High-resolution spectral domain optical coherence tomography system and structural characterization of *ex vivo* biological tissues using nanosensitive OCT

by

Rajib Dey

Supervisors: Prof. Martin J. Leahy

Dr Sergey Alexandrov

A thesis submitted in partial fulfillment of the requirements for the degree of Doctor of Philosophy,

Tissue Optics and Microcirculation Imaging Group,

School of Natural Sciences,

University of Galway, Ireland

Ollscoil na Gaillimhe
University of Galway

May 23, 2023

CONTENTS

Abstract.....6

Declaration.....8

Authorship Declaration.....9

Acknowledgements.....11

List of Publications 13

Acronyms and list of abbreviations.....15

List of Figures 18

List of Tables.....25

Chapter: 1

Biophotonics and optical coherence tomography in optical imaging

1.1 Introduction.....26
1.2 Aims and objective of the research.....34
1.3 Structure of the thesis.....35

Chapter: 2

Fundamental principles and applications of optical coherence tomography

2.1 Basic Theory.....44
2.2 Key Performance Metrics of OCT.....47
2.2.1 Central Wavelength and Spectral Range.....47
2.2.2 Axial Resolution.....49
2.2.3 Lateral Resolution.....49
2.2.4 Depth of Focus.....50
2.2.5 Total Measurement range / Imaging Depth.....51
2.2.6 Sensitivity and Roll-off.....51

2.3 Time-domain and Frequency-domain OCT 52

2.4 Imaging applications of OCT…….....56
2.4.1 OCT in Ophthalmology…….....56
2.4.2 OCT in Gastroenterology and Dermatology…….....57
2.4.3 OCT in Other Biomedical Applications…….……..59
2.4.4 OCT in Developmental Biology……..59
2.4.5 OCT in Material Imaging…….59

2.5 Conclusion…….....60

Chapter: 3

Development and simple characterization scheme of fibre-based near-isometric high-resolution optical coherence tomography system

3.1 Introduction…….……67

3.2 Materials and Methods …….....……..70
3.2.1 Experimental system setup ……...……70
3.2.2 Custom build LabVIEW program ……73
3.2.3 Air Wedge Theory and Construction…….75

3.3 OCT parameter measurements and Imaging Results……...……81
3.3.1 Measured system parameters…….……...81
3.3.2 Axial resolution and sensitivity measurements …….....81
3.3.3 Numerical simulation (using Zemax) and experimental validation of lateral resolution…….....83
3.3.4 Air wedge measurement methods and results……84
3.3.5 Air wedge spacing comparison between Telesto III and high-resolution system……..……88
3.3.6 Structural visibility comparison between existing Telesto III and developed high-resolution system……..91
3.3.6.1 Non-biological sample images……...……..91
3.3.6.2 Biological sample images……....92
3.3.6.3 Contrast to Noise Ratio (CNR) comparison between Telesto III and developed high-resolution OCT system images…….....94

3.4 Conclusion……...96

Chapter: 4

Skin cancer margin detection using nanosensitive optical coherence tomography and a comparative study with confocal microscopy

4.1 Introduction……104

4.2 Detection method and theory of nanosensitive optical coherence tomography…….....……...108
4.2.1 Theory of nsOCT……..……...…...108
4.2.2 nsOCT image formation……113

4.3 Impact of broad bandwidth light source on nsOCT……...…115

4.4 Materials and methods……....115

4.4.1 High resolution broadband spectral-domain OCT system……..…115
4.4.2 Tissue sample preparation……...…116
4.4.3 Confocal and light microscopy image analysis flowchart……..117

4.5 Results and discussion……....117

4.5.1 Numerical simulations to construct OCT and nsOCT images from synthesized submicron structures……...117
4.5.2 Experimental validation of nsOCT from submicron axial structures….119
4.5.3 nsOCT approach to detect submicron structural changes within marginal area from human skin cancer tissue……...…121
4.5.4 Structural sizes comparison between nsOCT technique and high-resolution confocal microscopy image from marginal area of human skin cancer tissue…….....……125
4.5.5 Healthy and lesional regions spatial period comparison from H&E slide using high-resolution light microscope……..127

4.6 Conclusion…….....……..129

Chapter 5

Non-invasive detection of nanoscale structural changes in cornea associated with cross-linking treatment

5.1 Introduction……138

5.2 Materials and Methods…….....141

5.2.1 Principle and demonstration of the over-sampling nsOCT…….....141

5.2.2 Experimental validation of the proposed nsOCT method using sum-micron structures……144

5.2.3 Numerical and experimental realization of nsOCT and over-sampling nsOCT methods on phantoms……145

5.2.4 *Ex vivo* bovine corneal cross-linking experiment……...148

5.2.5 Experimental system setup…….....149

5.3 Results……150

5.3.1 Structural visualization of virgin and treated cornea from confocal microscope images…….……150

5.3.2 Structural comparisons of virgin cornea, after riboflavin installation, and after corneal cross-linking process using over-sampling nsOCT technique.....……151

5.4 Discussion……...……159

5.5 Conclusion…….....……163

Chapter 6

Conclusion and future work……..……170

Abstract

Optical Coherence Tomography (OCT) is a rapidly growing imaging modality which is based on the principle of low coherence interferometry. It can perform high-resolution, cross-sectional imaging of the microstructure of biological tissues by detecting the coherent spectrum from the backscattered light. One significant advantage of OCT is that it can extract structural and functional imaging information in real time leading to a wide range of clinical and industrial imaging applications. Integration of OCT technology for imaging with high axial and spatial resolution to enhance the structural visibility into clinical practice is ongoing. During the FDOCT image construction, after inverse Fourier transform, high spatial frequencies, corresponding to small structural information is removed from the interference signal. All the high spatial frequency information exists in the OCT signal but does not exist in the constructed OCT image and it reduces the sensitivity to detect small structural changes. To detect this high spatial frequency information in each voxel of the three-dimensional OCT image, nanosensitive OCT (nsOCT) method has been invented. The nsOCT method provides the small size structural information with nanoscale sensitivity from all depth profiles of one single B-frame. The motivation of the thesis is to develop a high-resolution SDOCT system and enhance the structural imaging capability of *ex vivo* biological tissues using the developed nanosensitive OCT.

The first part of this thesis summarizes the fundamentals of OCT with a focus on the principles and key performance metrics. The various stages of development of OCT imaging since its invention is also summarized. Further, the thesis explores a development of the simple characterization scheme using fibre-based near-isometric resolution OCT system at a centre wavelength of 1300 nm with 400 nm bandwidth. Despite the challenges in transporting a broadband spectrum using fibre-optics, the system investigation was motivated by the ever-increasing demand for commercialization of high-resolution OCT systems and

simplification of construction. Furthermore, we evaluated and demonstrated a direct measurement method for axial resolution using an air wedge. Imaging of biomedical and other samples is demonstrated using a high numerical aperture objective lens and compared with images from a commercial OCT system. Further, the effect of the improved structural visibility by achieving image voxels closer to an isometric shape with a high NA sample lens is presented using our bespoke high-resolution OCT system.

The second part of this thesis discussed the application of nanosensitive OCT to improve the structural visibility with nanoscale sensitivity and broader dynamic range of detected spatial frequencies. The thesis demonstrates numerical and experimental detection of a few nanometres structural difference using the nsOCT method from single B-scan images of phantoms with sub-micron periodic structures acting like Bragg gratings. After that a single en face image is used to confirm the ability of nanosensitive OCT to map structural changes within the skin tissue with an intervening margin area at clinically relevant depths. In addition, the thesis compared the nsOCT en face image with a high-resolution confocal microscopy image from the same tissue. Different bandwidths of structural sizes confirm the structural differences between the healthy and lesional/cancerous region which further allow detection of the skin cancer margin. A corresponding study with other bandwidths of the lower spatial frequencies was done using histological images. As an another application of nsOCT, further the thesis demonstrated the structural changes with nanoscale sensitivity inside *ex vivo* bovine cornea associated with CXL treatment and clearly detected by the proposed over-sampling nsOCT method. This study shows that the spatial periods inside corneal stroma increased slightly after 30 minutes riboflavin instillation but decreased significantly after 30 min UVA irradiation. En face nsOCT images at different corneal depths have also confirmed the

consistent consequences, demonstrating that the nanoscale structural size decreases after the CXL treatment.

In summary, this thesis demonstrates that the broad bandwidth high-resolution spectral domain OCT can be used as a tool for structural imaging of biomaterial in conjunction with the nsOCT approach.

Declaration

The work in this thesis is based on the research carried out at the Tissue Optics and Microcirculation laboratory (TOMI), School of Physics, National University of Ireland Galway. I, Rajib Dey, hereby certify that this thesis has been written by me, that it is the record of work carried out by me and that it has not been submitted in any previous application for a degree or qualification.

Where work of other people has been consulted, quoted, or made use of in any other way, it has been fully acknowledged and referenced accordingly.

Rajib Dey

23rd May 2023

Authorship Declaration

This thesis contains the results of the research that I Rajib Dey, performed with in the Department of Physics and Applied Optics in the School of Natural Sciences at the University of Galway, between April 2018 and May 2023.

Chapters 3 and 4 of this thesis are reproductions of two first-authored publications, and while chapter 5 is a co-authored publication that has been rewritten and formatted by my own voice. The preparation of this thesis follows the guidelines set forth by the University of Galway's "Article based thesis" policy. I am the sole author of the remaining of this document.

Below are the details of the included publications and their respective locations in the thesis. The publications are listed in the order of appearance within the thesis:

1. **R. Dey (70%)**, Y. Zhou, Y. Neuhaus, S. Alexandrov, A. Nolan, T. C. Chang, and M. Leahy, "Simple Characterization Scheme for Optical Coherence Tomography Systems with Application to a Commercial and a Near-Isometric Resolution Fibre-Based System," *IEEE Photonics J.* **14**(1), 1-11 (2022).

Chapter 3: RD is the primary author of this article. RD along with YZ, SA and ML conceived and developed the methodology, RD designed and built the HR-SDOCT system, calibrated and characterized the HR-SDOCT system, performed imaging of different biological and non-biological phantoms, wrote the processing code and analysed data, RD along with YZ and TCC developed the LabVIEW platform, and RD led the writing of the manuscript which was reviewed and edited by all authors.

2. **R. Dey (70%)**, S. Alexandrov, P. Owens, J. Kelly, S. Phelan, and M. Leahy, "Skin cancer margin detection using nanosensitive optical coherence tomography and a comparative study with confocal microscopy," *Biomed. Opt. Express* **13**(11), 5654-5666 (2022).

Chapter 4: RD is the primary author of this article. RD along with SA and ML conceived and developed the methodology, RD designed and plan the work flow, performed 2D and 3D imaging from different human skin tissue and from non-biological phantom, RD with the help of SF and PW performed confocal and histology imaging, RD wrote the processing code and analysed data and performed numerical simulation, and led the writing of the manuscript which was reviewed and edited by all authors.

3. Y. Zhou, S. Alexandrov, A. Nolan, N. Das, **R. Dey (20%)** and M. Leahy "Non-invasive detection of nanoscale structural changes in cornea associated with corneal cross-linking treatment," *J. of Biophotonics* **13**(6), e201960234 (2020).

Chapter 5: RD is a co-author of this article. RD worked on phantom sample preparation with YZ for nsOCT method validation by experiment and performed numerical simulation. RD performed bovine cornea sample preparation and OCT imaging with the principal author of the article. RD helped YZ to process the acquired data, revise and edit the manuscript.

Rajib Dey
23rd May 2023

Acknowledgements

I would like to first thank my thesis supervisor, Prof. Martin Leahy. I am very appreciative of the time and effort that Prof. Leahy has invested in me from his very busy schedule. Prof. Leahy afforded unique opportunity to me as a member of his research group. Prof. Leahy has shown an unwavering concern for the success of his students, and has demonstrated a rare balance between always being accessible and allowing me almost a complete freedom and responsibility to pursue independent research. I am very grateful my studies were carried out in Prof Leahy's research group.

I also had the privilege of working with several excellent graduate / postdoctoral students in Prof. Leahy's research group: Sergey, Andrew, Yi, Nandan, Kai, Aedan, Cerine, VJ, Anand, Ryan, Soorya, Aron, Sean, Éanna. Thank you for your friendship and all the help that you guys have provided me over the past one year. My heartfelt gratitude to all the colleagues, technical staff and my graduate committee members for your support, encouragement and motivation during my time at School of Physics, University of Galway.

There are several collaborators outside Martin's laboratory who deserve recognition. I like to thank Prof. Jack Kelly, Prof. Thomas Ritter, Prof. Nirmalya Ghosh, Dr Sine Phelan, Dr Peter Wones, Dr Elizabeth Moloney for their kind support and valuable discussions.

I would like to thank my family and friends for their love and support throughout the years. The support of my parents, Mohan Dey and Mamata Dey, throughout my years of study has been truly amazing.

Some special friends – Conor, Ratul, Ibrahim, Ciarraí and Chiara for your friendship. You guys have been amazing friends and great people to work with.

Thank you for motivating and encouraging me to work with your work ethic and passion for science. I also thank all the present and past housemates for your love, warmth, support, and for all the shared moments together. Thank you Koustava, Balaji, Nandan. Galway would not have been the same for me if not for you all and this thesis may never have been brought to completion.

I would like to gratefully acknowledge fellowship and research facilities from Horizon 2020 STARSTEM research and innovation program and University of Galway.

Finally, I wish to express my appreciation and special thanks to the individuals who have assisted me in my doctoral research.

List of Publications

Refereed journal articles:

1. R. Dey, Y. Zhou, Y. Neuhaus, S. Alexandrov, A. Nolan, T. C. Chang, and M. Leahy, "Simple Characterization Scheme for Optical Coherence Tomography Systems with Application to a Commercial and a Near-Isometric Resolution Fibre-Based System," *IEEE Photonics J.* **14**(1), 1-11 (2022).
2. Y. Zhou, S. Alexandrov, A. Nolan, N. Das, R. Dey and M. Leahy "Non-invasive detection of nanoscale structural changes in cornea associated with corneal cross-linking treatment," *J. of Biophotonics* **13**(6), e201960234 (2020).
3. G. R. Sahoo, R. Dey, N. Das, N. Ghosh, and A. Pradhan, "Two dimensional multifractal detrended fluctuation analysis of low coherence images for diagnosis of cervical pre-cancer," *J. of Biomed. Phys. & Eng. Express* **6**(2), 025011 (2020).
4. R. Dey, S. Alexandrov, P. Owens, J. Kelly, S. Phelan, and M. Leahy, "Skin cancer margin detection using nanosensitive optical coherence tomography and a comparative study with confocal microscopy," *Biomed. Opt. Express* **13**(11), 5654-5666 (2022).

Conference Presentations:

1. R. Dey, Y. Zhou, N. Das, S. Alexandrov, A. Nolan, K. Neuhaus, M. Leahy, "Development of HR-SDOCT system using supercontinuum light source and its application in detecting nanoscale changes," *Proc. of SPIE Vol. 11228* (2020).
2. Y. Zhou, S. Alexandrov, A. Nolan, R. Dey, N. Das, K. Neuhaus, M. Leahy, "Application of over-sampling nano-sensitive optical coherence tomography for monitoring corneal internal structural changes in corneal cross-linking," *Proc. of SPIE Vol. 11228.* (2020).

3. N. Das, S. O'Gorman, S. Alexandrov, R. Dey, J. Chhablani, N. Ghosh, M. Leahy, "Nano sensitive study and fractal analysis of segmented retinal layers in Fourier domain OCT: promises for early disease detection" *Proc. of SPIE Vol. 10858.* (2019).

4. R. Dey, S. Alexandrov, P. Owens, J. Kelly, S. Phelan, and M. Leahy "Skin cancer margin detection using nanosensitive optical coherence tomography and a comparative

study with confocal microscopy" Oral presentation PW12352-7 at SPIE Photonics West 2023, 28 January-2 February, San Francisco USA 2023.

5. S. Alexandrov, A. Arangath, R. Dey, R. McAuley, and M. Leahy. "Visualization of the sub-wavelength structure of scattering objects with nano-sensitivity". Oral presentation PW23B-BO401-30 at SPIE Photonics West 2023, 28 January-2 February, San Francisco USA 2023.

Manuscripts in preparation:

1. R. Dey, G. Sordar, N. Das, S. Alexandrov J. Kelly, S. Phelan, and M. Leahy, "Characterization of micron and sub-micron scale skin cancer tissue using multifractal analysis model and validation with one class classification".
2. S. Alexandrov, R. McAuley, R. Dey, A. Arangath, Y. Zhou, A. Nolan, P. Owens, and M. Leahy, "Synthetic Fourier domain optical coherence tomography".

Acronyms and Abbreviations

2-D	Two-dimensional
3-D	Three-dimensional
ARPAM	Acoustic resolution PAM
CAM	Chorioallantoic membrane
CCD	Charge-coupled device
CCT	Central corneal thickness
CDV	Complex differential variance
cmOCT	Correlation mapping OCT
CMOS	Complementary metal-oxide-semiconductor
CNR	Contrast to noise ratio
CNV	Choroidal neovascularization
CSNR	Correlation signal to noise ratio
CT	Computerized tomography
CWS	Continuous wave spectroscopy
CWT	Continuous wavelet transform
CXL	Corneal cross linking
DC	Direct current
DCM	Dichroic mirror
DCS	Diffuse correlation spectroscopy
DRLS	Distance regularized level set
ECG	Electrocardiogram
EEG	Electroencephalogram
ED	Eigen decomposition
EM	Electromagnetic
EMG	Electromyogram
EV	Extracellular vesicles
FDA	Food and drug administration
FDOCT	Fourier domain OCT
FDML	Fourier domain mode locked Laser

fNIRS	Functional near infrared spectroscopy
FT	Fourier transform
FWHM	Full-width half maximum
GAG	Glycosaminoglycan
GI	Gastro intestinal
HSI	Hyperspectral imaging
IDFI	Incident dark field imaging
IR	Infrared
IFT	Inverse Fourier transform
LCI	Low coherence interferometry
LED	Light emitting diode
LDPI	Laser Doppler perfusion imaging
LIC	Lesser iris circle
LSCI	Laser speckle contrast imaging
MIP	Maximum intensity projection
MSF	Mean spatial frequency
MSC	Mesenchymal stem cells
MSC-EV	MSC-derived extracellular vesicles
MRI	Magnetic resonance imaging
NA	Numerical aperture
NIR	Near infra-red
nsOCT	Nanosensitive OCT
OCE	Optical coherence elastography
OCT	Optical coherence tomography
OCTA	Optical coherence tomography angiography
OD	Optical density
OMAG	Optical microangiography
OPD	Optical path displacement
OPL	Optical path length
ORPAM	Optical resolution PAM
PAI	Photoacoustic imaging
PAM	Photoacoustic microscopy

PAT	Photoacoustic tomography
PBS	Phosphate buffered saline
PET	Positron emission tomography
PSF	Point spread function
RIA	Radial iris arteries
RBC	Red blood cells
SDF	Side stream dark field imaging
SDOCT	Spectral domain OCT
SLD	Super luminescent diode
SNR	Signal to noise ratio
SSOCT	Swept source OCT
STED	Stimulated emission depletion tomography
SV	Speckle variance
SESF	Spectral encoding of spatial frequency
SEM	Transmission electron microscopy
TDOCT	Time domain OCT
TEM	Transmission electron microscopy
UVA	Ultraviolet-A

List of Figures

Fig. 1.1 Comparison of different imaging methods according to their resolutions and penetration depths. The length of the pendulum represents penetration depth, and the diameter of the sphere illustrates the spatial resolution of the imaging method……28

Fig. 2.1 Schematic of a time domain OCT system……..45

Fig. 2.2 (Left y-axis) Absorption coefficients of melanin, oxygenated haemoglobin, and water. (Right y-axis) Scattering coefficient of skin from……44

Fig. 2.3 The red line shows the theoretical sensitivity for FDOCT. The blue line is the TDOCT sensitivity for an unbalanced configuration. The squared dots are the actual measured system sensitivities for our FDOCT system……52

Fig. 2.4 High-resolution *in vivo* 3D OCT image of healthy hman skin…….....58

Fig. 3.1 Schematic of fibre based high-resolution spectral domain OCT system. SC Laser: Supercontinuum laser source, SuperK splitter, long pass, short pass and neutral density filters, OC: Optical Circulator, FC: 2×2 fibre coupler. L: Lenses, L5: Objective lens, RM: Reference mirror, X-Y Galvo, DG: Diffraction Grating……...…71

Fig. 3.2 (a) Represents the flowchart of the LabVIEW program. (b) interface of the X-Y Galvo setting parameters and scanning pattern…….74

Fig. 3.3 Plot (a) shows the numerical simulation based on equation (2) of a noisy double peak with a visible dip with arbitrary intensity values I along depth z. Plot (b) shows the simulated noiseless visibility v ($v = p–d$; p is peak height, d is dip height) for two peaks originating from a wedge reflection that move closer together along a lateral position x. The true size of depth z and x will be in the millimetre range and is not to scale for illustrative purpose. Best visibility would be achieved at $d = 0$ and $p = 1$ corresponding to a peak of unity intensity. The three different plots relate to different wedge slopes or wedge spacing. The “narrow” curve relates to a thin spacing or shallow slope, “medium” some spacing between narrow and

wide, and “wide” is the largest spacing or slope. The peaks would be fully merged at $x = 0$ (left) corresponding to the touching end of the wedge and fully separated for x position to the right. The ideal visibility starts to drop if the peak distance becomes smaller than the peak width. Without noise, the ideal visibility can be computed up to zero value……75

Fig. 3.4 (a) Shows the visibility function v for fitting with a visibility threshold due to parameter B related to equation (2). (b) shows the visibility function v with added noise. Plots (a) and (b) use arbitrary lateral dimensional scale in meters which in practice will be in the millimetre range. The average visibility of a structure must be at least above some noise threshold, which relates to the visibility threshold indicated. The grey shaded range is where the fitted function (black) would predict zero visibility without noise. The zero visibility must occur at lateral position $x_R > 0$. Based on the lateral position x_R, the axial resolution d can be calculated using equation (2). The measured visibility in section III-B confirms that the uncertainty impedes the detection of the peaks from the wedge reflections and the signal is lost before the lateral position $x = 0$ (Fig. 3.9)……77

Fig. 3.5 Output spectra of the SuperK EXU6 laser source. The selected spectral window used is from 1100 to 1500 nm (red box). (b) Sample arm spectrum obtained from mirror reflection……81

Fig. 3.6 (a) Interference pattern from sample mirror. (b) Measured axial PSF and roll-off over depth (z) and intensity in dB. The inset (red box) shows width of PSF at -6 dB from maximum at 100 µm depth. (c) Roll-off of sensitivity over a range of 1000 micrometre axial depth range……...82

Fig. 3.7 The lateral PSF was simulated, using Zemax, for three lateral positions over a scan range of ±1 mm from the principal `axis. The simulation results show that the lateral PSF remains constant over the full scan range…….83

Fig. 3.8 Lateral resolution validation using USAF test target. (a) Zoomed in view of group 6 and 7 elements from Thorlabs (USAF1951). The last resolved

line group is 6-4, highlighted in red colour box. (b) The line profile extracted from B-scan image across the vertical and horizontal direction of group 6-4…….....84

Fig. 3.9 The air-wedge geometry (top) related to the physical constructed wedge made of microscope slides (bottom). The geometry of the air-wedge is described by the visible length, *L*, the wedge spacer thickness, *D*, the lateral position, *x*, and the wedge gap, *d*, at this lateral position. The wedge gap, *d*, is assumed to be zero at the touching end. The average measured dimensions of the microscope slides are *L* = (71.0, 69.7, 67.4) mm, *D* = (0.070, 0.123, 0.237) mm (see Table II). The value *x* is measured by fitting in Fig. 9 and *d* is calculated with $d/x = D/L$……85

Fig. 3.10 Visibility measurements of Telesto III (a, b, c) and the high-resolution fibre optical OCT system (d, e, f). The fitting variance for the lateral position where visibility of the air gap is lost (for the factor *B* = 0.90 ...0.98) is shown as grey shade and the black dash line is *B* = 0.94. The grey regions are the lateral wedge positions where potentially the wedge may still be visible. The edge detection does not detect peaks for the full visibility range, and the uncertainty of visibility increases. Nevertheless, wedge separation may still be detectable within this region and the fitting provides a valid extension of the missing data points. The jagged visibility characteristic for the Telesto III system originates most likely from automatic contrast optimization. The visibility plots were assembled from multiple small segments using a scan range of 2.2 mm to cover the full wedge length. The arc shaped segments for the described high-resolution OCT system originate from the high NA lens…….....87

Fig. 3.11 Best detectable wedge spacings compared between Telesto III and the high-resolution system described. The mean difference between both systems is 2.8 microns, and the predicted improvement based on the light source bandwidth is 1.7 microns. Although the values fall within the

uncertainties, the consistent difference for three different wedges provides some confidence in an actual resolution difference. The box plot centre values represent the median, the upper and lower box boundaries represent the first and third quartile. The whiskers extend 1.5 times from the upper and lower box boundaries representing the interquartile range giving some estimate of the distribution of data points……..89

Fig. 3.12 Comparison of the HR-SDOCT (a) vs. the Telesto III (b) using Scotch tape. Image (a) shows smoother speckle structure due to the isometric voxel size……91

Fig. 3.13 Comparison of the HR-SDOCT (left column) vs Telesto III (right column). Images (a) and (b) show a fingertip and the zoomed regions (red box) show a less pronounced speckle washout for the HR-SDOCT system, which may be attributed to the improved isometric voxel shape using the high-NA sample lens. B-frame images of green cucumber (c) and (d). Red boxes from the same selected region show that again the speckle washout for the HR-SDOCT system is less pronounced. En face images of green cucumber (e) and (f). The red boxes from the same selected region show a sharper image, which is to be expected due to the higher NA lens used for the HR-SDOCT vs the Telesto III……..93

Fig. 4.1 Incident field and scattered field inside the object……...…108

Fig. 4.2 Illustration of far field approximation……110

Fig. 4.3 (a) illumination and scattering geometry in **K**-space for a particular one point on Ewald sphere (b) Spatial frequency representation in Ewald sphere at various wavelength……..112

Fig. 4.4 (a) Simulated OCT B-scan images from three different periodic structures and corresponding original spatial periods. (b) nsOCT B-scan images from (a) along with the detected submicron structural sizes……119

Fig. 4.5 Experimental demonstration of nsOCT technique using Bragg gratings, the detected axial spatial periods are 431.56 nm and 441.67 nm. (a) OCT B-

scan image, (b) nsOCT B-scan image of the two Bragg gratings. The colour bar represents structural size in nanometres……120

Fig. 4.6 (a), (d), and (g) conventional intensity-based OCT en face images of the tissue at the depths of ~200 μm, 400 μm, and 600 μm respectively. (b), (e), and (h) are corresponding nsOCT en face images with spatial period mapping, presenting the dominant structural size. The healthy, marginal, and lesional regions are separated by the red lines. The colour bar of the nsOCT en face images represents the spatial periods in nanometres. Plot (c), (f), and (i) show changes in the mean dominant spatial period of the structure between the two regions, defining an intervening marginal area in the nsOCT en face images……...123

Fig. 4.7 (a) Confocal microscopy image of the tissue sample. Line profiles of the selected red square box regions were taken for spatial period profile measurements using Fourier transform (b) box plot showing the spatial period distribution of the healthy and lesional regions. (c) and (d) spatial period profile obtained from selected lesional and healthy regions of the tissue……...……127

Fig. 4.8 (a) Histological sectioning image of the tissue sample. Line profiles of the selected black square boxes region were taken for spatial period profile measurements using Fourier transform (b) box plot showing the spatial period distribution of the healthy and lesional regions……128

Fig. 5.1 Flowchart for the over-sampling nsOCT signal processing. (a) Decompose axial spatial frequencies into multiple sub-bands and shift the dividing windows for over-sampling the spatial frequencies. (b) FFT of each sub-band and acquire the amplitude along different depths in each particular spatial frequency range. (c) Reconstruct and sum up all the spatial period profiles by taking the energy contribution of each sub-band and then obtain the dominant structural size for each voxel……143

Fig. 5.2 Experimental validation of the over-sampling nsOCT method by both B-scan and en face images. The two periodicity-different Bragg gratings and a tissue paper were covered under a two-layer tape. (a, b) Conventional intensity-based OCT B-scan and en face image at the depth marked by the dashed line. (c, d) The corresponding nsOCT B-scan and en face image with spatial periods mapping, visualizing the nanoscale structural differences between the samples. The colour bar presents the spatial periods with unit nanometre……..……...145

Fig. 5.3 Simulation results of nsOCT without and with over-sampling. (a) nsOCT without over-sampling can detect the difference of 6 nm but cannot distinguish very small difference, (b) nsOCT with over-sampling is able to distinguish the structural difference of 3 nm……146

Fig. 5.4 Experimental results of the Bragg gratings with the axial periodicity of 431.6 nm and 441.7 nm. (a) The nsOCT without over-sampling presents a 428.2 nm structural size. Error is 3.4 nm. (b) The nsOCT with over-sampling shows a 430.4 nm structural size. Error is 1.2 nm. (c) The nsOCT without over-sampling presents a 488.2 nm structural size. Error is 3.5 nm. (d) The nsOCT with over-sampling shows a 440.1 nm structural size. Error is 1.6 nm. The colour bar present the spatial periods with unit nanometre……...…148

Fig. 5.5 Confocal microscopy images of the virgin and treated cornea. (a) The virgin corneas consist of highly reflective and well-demarcated cell nuclei with an oval shape, indicated by white arrows. (b) The treated cornea is populated with some reflective interconnected stellate structures, containing elongated nuclei and keratocyte apoptotic bodies. The scale bar is 100 μm…….150

Fig. 5.6 B-scans of *ex vivo* bovine cornea during CXL treatment at three treating steps. (a, b) Both conventional OCT and nsOCT images acquired immediately after epithelial removal. (c, d) Images constructed after 30

min riboflavin instillation and (e, f) after 30 min UVA irradiation while finishing the treatment. The colour bar presents the spatial periods with unit nanometre……...152

Fig. 5.7 Histogram and boxplot of spatial period distributions inside cornea associated with CXL treatment. (a) Virgin cornea with the mean spatial period of 657.1 nm. (b) The cornea after 30 minutes riboflavin instillation with the mean value of 658.1 nm. (c) The crosslinked cornea with the mean value of 649.6 nm, with the histogram showing a shift towards lower spatial period compared with (a) and (b)……153

Fig. 5.8 Conventional OCT and nsOCT en face images at the three key treating steps during CXL treatment. (a, b, c) Conventional intensity-based OCT en face images of the cornea after epithelium removal, after 30 min riboflavin instillation and after 30 min UVA illumination, respectively. (d, e, f) The corresponding nsOCT en face images with spatial period mapping, presenting the nanoscale structural alterations. The en face images were constructed at the depth of ~500 μm. The colour bar presents the spatial periods with unit nanometre…….....156

Fig. 5.9 Mean spatial periods at various corneal depths for the virgin cornea, the cornea after 30 min riboflavin instillation and the cross-linked cornea, indicated by red, yellow and blue colour, respectively…….158

Fig. 5.10 The spatial periods plot of the treated cornea over different depths…….159

Fig. 5.11 A control experiment with the cornea half blocked from UVA irradiation. (a, b) Conventional intensity-based OCT and nsOCT images of the virgin cornea. (c) The conventional OCT image of the half cross-linked cornea using a UVA irradiation block on the right half. (d) The corresponding nsOCT image of the half cross-linked cornea, illustrating the nanoscale structural difference between the left half and right half in the same B-scan.

The colour bar presents the spatial periods with unit nanometre…….....162

List of Tables

Table 3.1 Public reported axil resolution of fibre-optic based HR-SDOCT systems with centre wavelength of 1300 nm……...69

Table 3.2 We used wedges with different spacer thickness to evaluate the impact of the wedge slope on the gap visibility……78

Table 3.3 CNR compared between Telesto and high-resolution system……...95

Table 4.1 The means spatial period changes of the lesional and healthy regions….124

Table 5.1 The intensity changes between the virgin cornea and cross-linked cornea during the CXL treatment……...154

Table 5.2 The spatial period changes of the virgin cornea and cross-linked cornea during the CXL treatment……...155

Chapter 1

Biophotonics and optical coherence tomography in optical imaging

1.1 Introduction

The most prevalent earlier medical imaging methods are X-ray radiography, ultrasound imaging (ultrasonography), X-ray computed tomography (CT), and magnetic resonance imaging (MRI). Roentgen introduced X-ray as the first medical imaging tool in 1895 [1] and during the 20th century the use of diagnostic imaging became central to medical diagnosis and management. All of these imaging modalities are based on electromagnetic radiation or sound wave to explore the macroscopic range of tissue structures from an image. Over half a century, these imaging modalities are being used as an ideal technology for medical imaging and diagnostic applications. These non-invasive imaging techniques can give high precision and sensitivity without damaging the object structures. These imaging techniques do not provide micron level superior imaging resolution, but they give much higher penetration depth than other optical imaging techniques such as optical coherence tomography for clinical imaging of tissue structures. To detect small structural and morphological changes in biological materials, higher resolution optical imaging systems are required.

Over the years, researchers have used light-based optical imaging systems to investigate the biological fundamentals of life. Nowadays, for all medical optical imaging, from UV to deep IR, broad spectral range light sources are used to investigate the biological structures. The advantage of optical imaging for medical applications in biological tissue is that optical photons provide nonionizing and safe radiation. Optical spectra which are based on absorption, fluorescence, Raman scattering provide biochemical information because they are related to molecular information. Optical absorption provides contrast for functional imaging. Optical scattering spectra provide information about the size

distribution of optical scatterers. Optical polarization provides information about structurally anisotropic components. Optical spectroscopy permits simultaneous detection of multiple contrast agents. Optical transparency in the eye provides a unique opportunity for high-resolution imaging of the retina, and so on. On account of all these advantages, optical imaging provides great potential in clinical diagnosis, early detection of disease, and monitoring of disease progression. However, for optical imaging, resolution is one of the major important parameters determining how much smaller structural or functional information of the object can be measured. Also, the penetration depth is one of the important parameters which can give depth information on the extent of a disease progress, which is especially important for clinical optical imaging applications. Figure 1.1 represents axial or depth resolution vs. penetration depth for the different medical imaging techniques. Nowadays, these techniques are used as standard clinical imaging for disease diagnosis [2]. From figure 1.1, it can be noticed that optical imaging modalities provide high axial resolution compared to other diagnostic imaging systems such as X-ray radiography, ultrasound imaging, X-ray computed tomography (CT), and magnetic resonance imaging (MRI) techniques. Also, figure 1.1 illustrates that, for all imaging modalities, image resolution is inversely proportional to the penetration depth [3]. The reason is the attenuation of light/sound waves returning from deeper locations inside the object, which increases the pixel size necessary to gather measurable signals from deeper areas. However, penetration depth of the input light depends on the absorption and scattering properties of the imaging object. Thus, absorption and scattering properties are typically dependent on the illumination wavelength i.e., the choice of the wavelength of the light source [4].

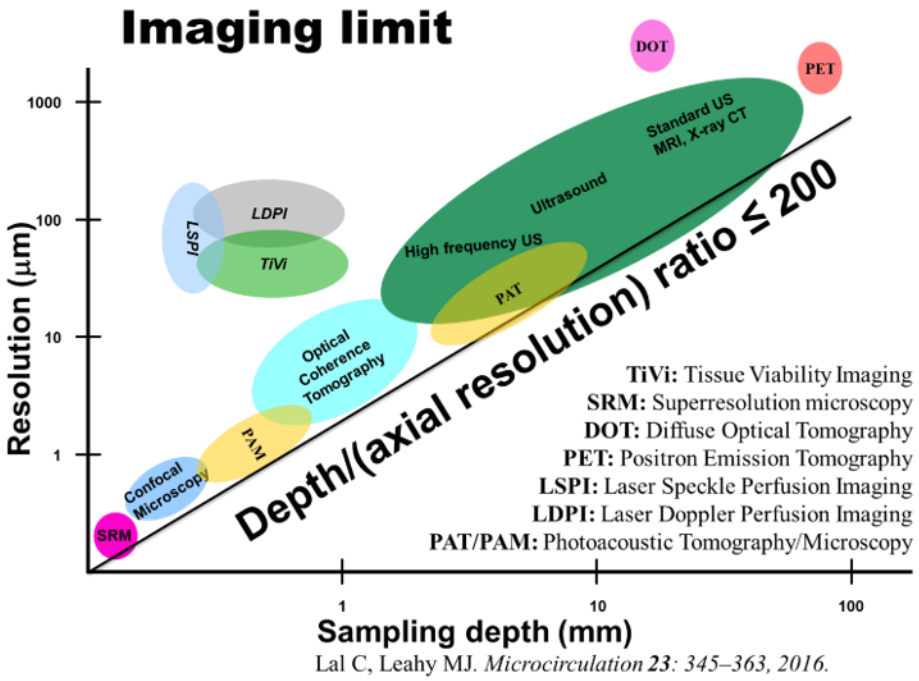

Fig. 1.1 Comparison of different imaging methods according to their resolutions and penetration depths [2].

Optical imaging is in widespread use in clinical diagnostics, biomedical and industrial research. All are based on surface imaging techniques, subsurface imaging techniques, and deep tissue imaging techniques. Confocal microscopy [5], super-resolution microscopy [6], phase microscopy [7], non-linear microscopy [8], second harmonic generation microscopy [9], capillaroscopy [10], two-photon microscope imaging [11], Raman imaging [12], and stimulated emission depletion tomography (STED) or super-resolution imaging [13] are surface imaging techniques. Most of these optical imaging procedures provide only two-dimensional images. Optical coherence tomography (OCT) [14], hyperspectral imaging [15], side stream dark field imaging (SDF) and incident dark field imaging (IDFI) [16] are made up with subsurface imaging techniques. Deep tissue imaging techniques discussed include diffuse correlation spectroscopy (DCS) [17], functional near infrared spectroscopy (fNIRS) [18], and photoacoustic tomography (PAT) [19].

Figure 1.1 indicates that confocal microscopy is one of the most high-resolution optical imaging techniques. It can acquire high-contrast 3D images up to a depth of 200 microns. Marvin Minsky first introduced the working principle of confocal imaging in 1955 [5]. After systematic improvements in the confocal microscope, it became an important optical imaging tool in the life sciences and in medical research. The resolution of the confocal microscope is higher, and penetration depth is more limited than other optical imaging techniques. Due to the shallow imaging depth, confocal microscope has limited use, especially for clinical *in vivo* imaging. Also, for *ex vivo* imaging requires specially prepared thin samples. Some highly scattering biological samples such as skin does not provide good quality confocal microscopy images because sample thickness is not sufficient. This imaging technique is used to study the principles of vessel regression [20], erythrocyte properties [21], and detecting skin lesions in oncology [22].

OCT is one of the imaging techniques that can fill the gap between the confocal microscope and other imaging techniques in terms of image resolution and imaging depth. OCT is a non-invasive imaging technique that utilizes the principles of interferometry to generate high-resolution, cross-sectional images of biological tissues. The mechanism of OCT involves the interaction of light with the tissue and the subsequent detection of the reflected or backscattered light. The basic setup of an OCT system consists of a low-coherence light source, a beam splitter, a reference arm, a sample arm, and a detector. The low-coherence light source typically emits near-infrared light, which has good tissue penetration. According to figure 1.1, OCT image resolution is 10-100 times higher, and the penetration depth is shallower compared to other clinical imaging techniques including ultrasound imaging, computed tomography, and magnetic resonance imaging. On the other hand, confocal microscopy provides better resolution than OCT. However, in the biological tissue penetration depth of the confocal microscope is limited to several hundred microns. OCT is a 3D imaging technique

that provides high axial and lateral resolution up to a few millimetres depth within the imaging object. It is a high-speed, noncontact, and non-invasive imaging technique. This optical imaging technique is acceptable for both *in vivo* and *ex vivo* imaging. Since the development of the OCT as an optical imaging technique in 1991, it is widely used for both structural and functional imaging applications [23]. For the disease diagnosis, especially in ophthalmology, OCT has become the gold standard clinical imaging tool for detecting morphological changes [24]. It has been used for many medical and surgical applications including heart and blood vessels [25], tumours [26], visualization of the dental structure [27] and diagnosis and treatment of skin diseases [28]. OCT is also used for other optical imaging applications including in material science [29], structural analysis of polymer composites [30], sensor technology [31], among many other applications.

Earlier development of the OCT was based on the time-domain (TDOCT), and this has been applied to non-invasive cross-sectional imaging in biological tissue [14]. It is based on the time-domain interferometric technique. In TD-OCT, a broadband light source emits short pulses of light, typically in the near-infrared range. The light is split into two paths: the reference arm and the sample arm. The light in the reference arm is directed towards a mirror, while the light in the sample arm is directed towards the biological tissue being imaged. To capture the interference pattern, a movable reference mirror in the reference arm is scanned back and forth, changing the reference path length. As the reference mirror is moved, the interference pattern is detected by a photodetector. The detected signal is recorded as a function of time, represent the depth information. Two years after the development of the TDOCT in 1993, OCT was used to perform *in vivo* imaging of the retina [32]. However, the imaging speed and sensitivity of the earlier TDOCT systems was two A-scans/second, which is not sufficient speed for biomedical imaging. To increase the imaging speed of the OCT system,

Fercher *et al.* introduced SDOCT system in 1995 to measure the corneal thickness [33]. First swept source OCT (SSOCT) was also introduced by tuneable light source in 1997 [34]. Before 1997 the advantage of sensitivity was not recognized or demonstrated to improve the image quality of the OCT. Andretzky *et al.* and Mitsui first gave theoretical hints about the advantage of sensitivity in 1998 [35, 36]. Five years later in 2003 Leitgeb *et al.*, de Boer *et al.*, Choma *et al.* demonstrated the significant advantages of the sensitivity in spectral-domain [37, 38] and swept-source [39] OCT systems over time-domain OCT systems. They provided both a theoretical derivation and an experimental confirmation of the sensitivity. With the rapid development of the OCT technology, the imaging speed has been improved significantly, which was a great success of OCT as an *in vivo* medical imaging technology. An SDOCT system with an imaging speed of 15 kHz (A-scans/second) was demonstrated in 2003 [40]. Using the ultra-high speed CMOS line scan camera and SDOCT system, Benjamin *et al.* demonstrated 312.5 kHz axial scan per second in 2008 [41]. Wolfgang Wieser *et al.* presented a swept source OCT system with enabling depth scan rates as high as 20.8 million lines per second for high quality 2D and 3D imaging of biological tissue [42]. Most recently, Jiqiang Kang *et al.* demonstrated 44.5 MHz A-scan rate SSOCT system with the implementation of a mode-locked fibre laser and time stretch techniques. This ultra-high speed makes a new record to realize high-performance volumetric OCT imaging in real time [43].

In clinical studies, OCT has been used since the mid-1990s. However, it was the years 1995-1996, that OCT reached a significant milestone in disease diagnosis, becoming useful in the diagnosis of retinal and macular diseases including glaucoma, macular oedema, aged-related macular degeneration, and choroidal neovascularization [44-47]. In 1996 the first commercial ophthalmic OCT machine was released for clinical studies [48]. After 10 years of experimental validation, advances in technology and improved clinical data, OCT finally

became a standard of care imaging tool in ophthalmology in 2005 [49]. In the year of 2006 OCT imaging technique got its first FDA approval for routine ophthalmic care, and the OCT market began to grow [50]. In addition to the ophthalmic OCT system, other OCT systems for commercial clinical purposes such as cardiovascular, dermatology, gastroenterology, and angiographic OCT systems came into the market in 2004, 2010, 2013 and 2014, respectively [51]. All of these commercial OCT systems further expanded the OCT market for clinical studies. It was estimated that a total number of ~30 Million OCT imaging systems were in use worldwide by 2017 [51] and the OCT system market reached $1Bn per year. In 2021 with rising usage of OCT in clinical and industrial application, the global OCT market size was evaluated $1.1 Bn, and it is likely to reach a valuation of $1.2 Bn in 2022 [52]. That being said, integration of cutting-edge OCT technology into clinical practice is still an evolving process.

First generation TDOCT systems resolution were not sufficient to image small biological tissue structures and the axial resolution is in the order of 10-20 μm [53]. Fourier domain OCT (FDOCT), mostly SDOCT improved 2-3 times the axial resolution by improving the advanced technology such as spectral bandwidth and stability of the light source, sensitivity, respectively [54, 55]. In the past couple of years, in combination with microscopy and OCT, advanced techniques such as optical coherence microscopy (OCM) [56] and, line-field confocal optical coherence tomography (LC-OCT) [57] were developed to improve the axial resolution less than 1 μm with high lateral resolution, in conjunction with high-numerical aperture objective lens. All these techniques are limited to several hundred microns imaging depths to acquire volume images. Depth information is crucial to acquire more structural details in the deeper region for any kind of disease detection, for example skin cancer. OCM and LC-OCT can detect small structural alterations allowing differentiation of cancer or precancer tissues from normal tissues. These high-resolution imaging techniques

can be used to study cancer detection, where all the morphological changes happen at the sub-cellular label. There is a need to investigate the early-stage development of cancer within the tissue structures where they undergo the nanoscale structural changes as they progress. These changes can be present long before they manifest as a disease. To detect such structural changes, there is a need to improve sensitivity to structural changes at the nuclear level. It is obvious that to visualize the structural changes in the nanoscale label, we must improve the resolution. However, if the resolution is a few nanometres then it would be difficult to acquire a small 3D volume image like $1\times1\times1$ mm^3 from each voxel and one 3D volume size will be large. Due to a large volume of data size, it would be difficult to process the data, and it is also time-consuming. So, an ultra-high-resolution system is not required to detect small structural changes where image penetration depth is limited. Instead of ultra-high-resolution systems, the more practical way may be the use of highly sensitive OCT systems to detect small structural alterations within the tissue. So, micron-scale axial and spatial resolutions with a highly sensitive OCT system can detect nanoscale structural alteration within the different tissue images. Moreover, improving the dynamic range of nanometre length scale sensitivity requires a broad spectral bandwidth light source. Within the detected broader spectral range, different nanometre length scale structures can be detectable from each voxel of a 3D volume [58-60]. The motivation of this thesis is to develop a fibre-based high-resolution SDOCT system with a broadband supercontinuum laser light source and to explore the enhancement of structural imaging capability from *ex vivo* biological tissue samples.

1.2 Aims and objectives of the research

- Development of a simple characterization scheme of fibre-based HR-SDOCT system using broadband supercontinuum light source. Which aims to imprve axial and lateral resolutions of the SDOCT system than existing SDOCT system. This develop SDOCT system creates a new palatform to visualize detail structural information from biological tissues with higher resolution.
- Design LabVIEW program that will control the main components (like galvo scanner and spectrometer) and create a single interface to control the whole system and reconstruct a depth profile from the raw data.
- Evaluation and demonstration of the direct measurement method for axial resolution using an air wedge and compare axial resolution with a commercial OCT system. The aim of this simple measurement method is to demonstrate the capability of high axial resolution measurement in a simple way.
- Improve the structural visibility by achieving image voxels closer to an isometric shape with a high NA sample lens and comparison with the existing commercial system.
- Demonstration of nanosensitive OCT (nsOCT) model for *ex vivo* human skin cancer intervening margin detection and comparative study with high-resolution confocal microscopy imaging. This nsOCT method would enable to distrihush healthy and lesional region from different nanoscale structural imformations of a single en face image.
- Demonstration of over-sampling nsOCT model on *ex vivo* bovine cornea to detect the nanoscale structural alteration which is associated with cross-linking treatment. The proposed over-sampling nsOCT has the potential to detect the nanoscale structural information from the different corneal depth

without any additional components. Which could be use as a novel clinical imaging system for ophthalmic applicatons.

1.3 Structure of the thesis

The chapters of this thesis are presented as summarized below:

Chapter 1: This chapter introduces the domain of existing medical optical imaging methods with their applications, resolution, and penetration depths. The chapter also provides details history and development of OCT technology over the years.

Chapter 2: This chapter discusses the fundamental principles of the OCT. To optimize the OCT system. Key performance metrics are explained. A detailed description of the different OCT methods including time domain and Fourier domain are described. This chapter also provides details on the existing structural imaging applications using OCT. The chapter provides the technical context for the chapters that follow and are explored in this thesis.

Chapter 3: This chapter presents a simple characterization scheme for OCT system using a supercontinuum laser light source. This chapter introduces a fibre-based near isometric resolution OCT system at a centre wavelength of 1300 nm with an axial resolution of 3.8 μm in air and lateral resolution of 5.5 μm. In this chapter we also evaluate and demonstrate the direct measurement method for axial resolution using an air wedge and compared axial resolution with a commercial OCT system. Imaging of biomedical and other samples is demonstrated using a high numerical aperture sample lens and compared with images from a commercial OCT system. This chapter also discusses the effect of the improved structural visibility by achieving image voxels closer to an isometric shape with a high NA sample lens.

Chapter 4: In this chapter, we present a recently developed technique, nanosensitive OCT (nsOCT), improved using broadband supercontinuum laser, and demonstrate nanoscale sensitivity to structural changes within *ex vivo* human skin tissue. This chapter starts with an explanation of the underlying principles of the nsOCT theory before moving on to the detailed processing steps required to form nsOCT images. Further, we demonstrated numerical and experimental detection of a few nanometres structural differences using the nsOCT method from phantoms with sub-micron periodic structures, acting like Bragg gratings. Then we show that nsOCT can distinguish nanoscale structural changes at the skin cancer margin from the healthy region, in en face images at clinically relevant depths. This chapter also describes the comparison of the nsOCT en face image with an existing high-resolution imaging modality, in this instance, confocal microscopy image to confirm the structural differences between the healthy and lesional/cancerous regions.

Chapter 5: This chapter presents the application of over-sampling nanosensitive optical coherence tomography (nsOCT) method for probing the corneal structural alterations. Further, as an advantage of over-sampling nsOCT we discuss numerical and experimental detection of a few nanometres structural differences using the over-sampling nsOCT method from phantoms with sub-micron periodic structures. We then show that over-sampling nsOCT can distinguish nanoscale structural alteration during *ex vivo* corneal corneal cross-linking (CXL) treatment.

Chapter 6: This chapter summarises the thesis based on experimental findings and recommended future directions for the research presented in the thesis.

References

1. L. V. Wang, and H. I. Wu, *Biomedical Optics: Principles and Imaging*. John Wiley & Sons (2012).
2. C. Lal, and M. J. Leahy, "An updated review of methods and advancements in microvascular blood flow imaging," *Microcirculation* **23**(5), 345-363 (2016).
3. A. Unterhuber, B. Považay, K. Bizheva, B. Hermann, H. Sattmann, A Stingl, T. Le, M. Seefeld, R. Menzel, M. Preusser, and H. Budka, "Advances in broad bandwidth light sources for ultrahigh resolution optical coherence tomography," *Phys. Med. Biol.* **49**(7), 1235-1246 (2004).
4. C. F. Bohren, and D. R. Huffman, *Absorption and scattering of light by small particles*. John Wiley & Sons (2008).
5. A. Nwaneshiudu, C. Kuschal, F. H. Sakamoto, R. Rox Anderson, K. Schwarzenberger, and R. C. Young, "Introduction to Confocal Microscopy," *J. Invest. Dermatol* **132**(12), 1–5 (2012).
6. M. Yamanaka, N. I. Smith, and K. Fujita, "Introduction to super-resolution microscopy," *Microscopy* **63**(3), 177-192 (2014).
7. V. P. Tychinskii, "Dynamic phase microscopy: is a 'dialogue' with the cell possible?" *Physics-Uspekhi* **50**(5), 513-528 (2007).
8. N. Mazumder, N. K. Balla, G. Y. Zhuo, Y. V. Kistenev, R. Kumar, F. J. Kao, S. Brasselet, V. V. Nikolaev, and N. A. Krivova, "Label-free non-linear multimodal optical microscopy-basics, development, and applications" *Frontiers in Physics* **7**, 1-26 (2019).
9. R. Gauderon, P. B. Lukins, and C. J. R. Sheppard, "Optimization of second-harmonic generation microscopy," *Micron* **32**(7), 691-700 (2001).
10. A. K. Murray, K. Feng, T. L. Moore, P. D. Allen, C. J. Taylor, and A. L. Herrick, "Preliminary clinical evaluation of semi-automated nailfold

capillaroscopy in the assessment of patients with Raynaud's phenomenon.," *Microcirculation* **18**(6), 440–447 (2011).

11. F. Helmchen, and W. Denk, "Deep tissue two-photon microscopy," *Nat. Med.* **2**(12), 932-940 (2005).
12. Y. Zhang, H. Hong, and W. Cai, "Imaging with Raman Spectroscopy," *Curr. Pharm. Biotechnol.* **11**(6), 654–661 (2010).
13. G. Vicidomini, P. Bianchini, and A. Diaspro, "STED super-resolved microscopy," *Nat. Med.* **15**(3), 173–182 (2018).
14. D. Huang, E. A. Swanson, C. P. Lin, J. S. Schuman, W. G. Stinson, W. Chang, M. R. Hee, T. Flotte, K. Gregory, C. A. Puliafito, and J. G. Fujimoto, "Optical Coherence Tomography," *Science* **254**(5035), 1178–1181 (1991).
15. J. Yoon, "Hyperspectral Imaging for Clinical Applications," *BioChip J.* **16**, 1-12 (2022).
16. H. A. Van Elteren, C. Ince, D. Tibboel, I. K. M Reiss, and R. C. J. de Jonge, "Cutaneous microcirculation in preterm neonates: comparison between sidestream dark field (SDF) and incident dark field (IDF) imaging." *J. Clin. Monit. Comput.* **29**(5), 543-548 (2015).
17. T. Durduran, and A. G. Yodh, "Diffuse correlation spectroscopy for non-invasive, micro-vascular cerebral blood flow measurement," *Neuroimage* **85**, 51-63 (2014).
18. K. B. Beć, J. Grabska, C. W. Huck, "Near-infrared spectroscopy in bio-application," *Molecules* **25**(12), 2948 (2020).
19. L. V. Wang and J. Yao, "A practical guide to photoacoustic tomography in the life sciences," *Nat. Med.* **13**(8), 627–638 (2016).
20. M. S. Wietecha, W. L. Cerny, and L. A. DiPietro, "Mechanisms of vessel regression: toward an understanding of the resolution of angiogenesis," New perspectives in regeneration, Current Topics in Microbiology and Immunology, *Springer, Berlin, Heidelberg* **367**, 3-32 (2012).

21. C. Saldanha, “Instrumental analysis applied to erythrocyte properties,” *J. Cell. Biotechnol.* **1**(1), 81–93 (2015).
22. M. A. Ilie, C. Caruntu, M. Lupu, D. Lixandru, M. Tampa, S. R. Georgescu, A. Bastian, C. Constantin, M. Neagu, S. A. Zurac, and D. Boda, “Current and future applications of confocal laser scanning microscopy imaging in skin oncology,” *Oncol. Lett.* **17**(5), 4102-4111 (2019).
23. J. G. Fujimoto, C. Pitris, S. A. Boppart, and M. E. Brezinski, “Optical coherence tomography: an emerging technology for biomedical imaging and optical biopsy,” *Neoplasia* **2**(1-2), 9-25 (2000).
24. P. Massin, A. Girach, A. Erginay, and A. Gaudric, “Optical coherence tomography: a key to the future management of patients with diabetic macular oedema,” *Acta Ophthalmol. Scand.* **84**(4), 466-474 (2006).
25. S. Yousefi, T. Liu, and R. K. Wang, “Segmentation and quantification of blood vessels for OCT-based micro-angiograms using hybrid shape/intensity compounding,” *Microvascular Research* **97**, 37-46 (2015).
26. A. Filloy, J. M. Caminal, L. Arias, S. Jordán, and J. Català, “Swept source optical coherence tomography imaging of a series of choroidal tumours,” *Can. J. of Ophthalmol.* **50**(3), 242-248 (2015).
27. H. Schneider, K. J. Park, M. Häfer, C. Rüger, G. Schmalz, F. Krause, J. Schmidt, D. Ziebolz, and R. Haak, “Dental applications of optical coherence tomography (OCT) in cariology” *Appl. Sci.* **7**(5), 472 (2017).
28. A. P. Yow, R. Srivastava, J. Cheng, A. Li, J. Liu, L. Schmetterer, H. L. Tey, and D. W. Wong, “Techniques and applications in skin OCT analysis,” *Deep Learning in Medical Image Analysis, Advance in Experimental Medicine and Biology, Springer* **1213**, 149-163 (2020).
29. A. M. Zysk, F. T. Nguyen, A. L. Oldenburg, D. L. Marks, and S. A. Boppart, “Optical coherence tomography: a review of clinical development from bench to bedside,” *J. Biomed. Opt.* **12**(5), 051403 (2007).

30. E. Gliścińska, D. Sankowski, I. Krucińska, J. Gocławski, M. Michalak, Z Rowińska, and J. Sekulska-Nalewajko, "Optical coherence tomography image analysis of polymer surface layers in sound-absorbing fibrous composite materials," *Polymer Testing* **63**, 194-203 (2017).
31. M. Kogel-Hollacher, M. Strebel, C. Staudenmaier, H. I. Schneider, and D. Regulin, "OCT sensor for layer height control in DED using SINUMERIK® controller," *In Laser 3D Manufacturing VII, Proc. SPIE* **11271**, 59-63 (2020).
32. E. A. Swanson, J. A. Izatt, M. R. Hee, D. Huang, C.P. Lin, J. S. Schuman, C. A. Puliafito, and J. G. Fujimoto, "*In vivo* retinal imaging by optical coherence tomography," *Opt. Lett.* **18**(21), 1864-1866 (1993).
33. A. F. Fercher, C. K. Hitzenberger, G. Kamp, and S. Y. El-Zaiat, "Measurement of intraocular distances by backscattering spectral interferometry," *Opt. Commun.* **117**(1-2), 43-48 (1995).
34. B. Golubovic, B. E. Bouma, G. J. Tearney, and J. G. Fujimoto, "Optical frequency-domain reflectometry using rapid wavelength tuning of a Cr 4+: forsterite laser," *Opt. Lett.* **22**(22), 1704-1706 (1997).
35. P. Andretzky, M. W. Lindner, J. M. Herrmann, A. Schultz, M. Konzog, F. Kiesewetter, and G. Hausler, "Optical Coherence Tomography by spectral radar: dynamic range estimation and *in vivo* measurements of skin," *Optical and Imaging Techniques for Biomonitoring IV, Proc. SPIE* **3567**, 78-87 (1999).
36. T. Mitsui, "Dynamic range of optical reflectometry with spectral interferometry," *Jpn. J. Appl. Phys.* **10**(38), 6133–6137 (1999).
37. R. Leitgeb, C. K. Hitzenberger, and A. F. Fercher, "Performance of fourier domain vs. time domain optical coherence tomography," *Opt. Express* **11**(8), 889–894 (2003).
38. J. F. de Boer, B. Cense, B. H. Park, M. C. Pierce, G. J. Tearney, and B. E. Bouma, "Improved signal-to-noise ratio in spectral-domain compared with

time-domain optical coherence tomography," *Opt. Lett.* **28**(21), 2067–2069 (2003).

39. M. A. Choma, M. V. Sarunic, C. H. Yang, and J. A. Izatt, "Sensitivity advantage of swept source and Fourier domain optical coherence tomography," *Opt. Express* **11**(18), 2183–2189 (2003).
40. M. Wojtkowski, T. Bajraszewski, P. Targowski, and A. Kowalczyk, "Real-time *in vivo* imaging by high-speed spectral optical coherence tomography," *Opt. Lett.* **28**(19), 1745-1747 (2003).
41. B. Potsaid, I. Gorczynska, V. J. Srinivasan, Y. Chen, J. Jiang, A. Cable, and J. G. Fujimoto, "Ultrahigh speed Spectral / Fourier domain OCT ophthalmic imaging at 70,000 to 312,500 axial scans per second," *Opt. Express* **16**(19), 15149-15169 (2008).
42. W. Wieser, B. R. Biedermann, T. Klein, C. M. Eigenwillig, and R. Huber, "Multi-Megahertz OCT: High quality 3D imaging at 20 million A-scans and 4.5 GVoxels per second," *Opt. Express* **18**(14), 14685-14704 (2010).
43. J. Kang, P. Feng, X. Wei, E. Y. Lam, K. K. Tsia, and K. K. Y. Wong, "102-nm, 44.5-MHz inertial-free swept source by mode-locked fibre laser and time stretch technique for optical coherence tomography," *Opt. Express* **26**(4), 4370-4381 (2018).
44. J. S. Schuman, M. R. Hee, A. V. Arya, T. Pedut-Kloizman, C. A. Puliafito, J. G. Fujimoto, and E. A. Swanson, "Optical coherence tomography: a new tool for glaucoma diagnosis," *Curr. Opin. Ophthalmol.* **6**(2), 89-95 (1995).
45. M. R. Hee, C. A. Puliafito, C. Wong, J. S. Duker, E. Reichel, B. Rutledge, J. S. Schuman, E. A. Swanson, and J. G. Fujimoto, "Quantitative assessment of macular edema with optical coherence tomography," *Arch. of Ophthalmol.* **113**(3), 1019-1029 (1995).
46. C. A. Puliafito, M. R. Hee, C. P. Lin, E. Reichel, J. S. Schuman, J. S. Duker, J. A. Izatt, E. A. Swanson, and J. G. Fujimoto, "Imaging of Macular

Diseases with Optical Coherence Tomography," *Ophthalmology* **102**(2), 217-229 (1995).

47. M. R. Hee, C. R. Baumal, C. A. Puliafito, J. S. Duker, E. Reichel, J. R. Wilkins, J. G. Coker, J. S. Schuman, E. A. Swanson, and J. G. Fujimoto, "Optical Coherence Tomography of Age-related Macular Degeneration and Choroidal Neovascularization," *Ophthalmology* **103**(8), 1260-1270 (1996).
48. M. E. Brezinski, G. J. Tearney, B. E. Bouma, J. A. Izatt, M. R. Hee, E. A. Swanson, J. F. Southern, and J. G. Fujimoto, "Optical coherence tomography for optical biopsy: properties and demonstration of vascular pathology," *Circulation* **93**(6), 1206-1213 (1996).
49. M. Wojtkowski, V. Srinivasan, J. G. Fujimoto, T. Ko, J. S. Schuman, A. Kowalczyk, and J. S. Duker, "Three-dimensional retinal imaging with high-speed ultrahigh-resolution optical coherence tomography," *Ophthalmology* **112**(10), 1734-1746 (2005).
50. A. A. Moshfeghi, P. J. Rosenfeld, C. A. Puliafito, S. Michels, E. N. Marcus, J. D. Lenchus, and A. S. Venkatraman, "Systemic bevacizumab (Avastin) therapy for neovascular age-related macular degeneration: twenty-four–week results of an uncontrolled open-label clinical study," *Ophthalmology* **113**(11), 2002-2011 (2006).
51. E. A. Swanson and J. G. Fujimoto, "The ecosystem that powered the translation of OCT from fundamental research to clinical and commercial impact [Invited]," *Biomed. Opt. Express* **8**(3), 1638-1664 (2017).
52. Optical Coherence Tomography Market by Product, Capacity, Application, Distribution Channel & Region - Forecast 2022 – 2032 (https://www.futuremarketinsights.com/reports/optical-coherence-tomography-equipment-market)

53. M. K. Leung, and B. A. Standish, Optical Coherence Tomography for Imaging Biological Tissue, *Handbook of 3D machine vision: Optical metrology and imaging,* 316-334 (2013).
54. M. Szkulmowski, M. Wojtkowski, T. Bajraszewski, I. Gorczyńska, P. Targowski, W. Wasilewski, A. Kowalczyk, and C. Radzewicz, "Quality improvement for high resolution *in vivo* images by spectral domain optical coherence tomography with supercontinuum source," *Opt. Commun.* **246**(4-6), 569-578 (2005).
55. P. Cimalla, J. Walther, M. Mehner, M. Cuevas, and E. Koch, "Simultaneous dual-band optical coherence tomography in the spectral domain for high resolution *in vivo* imaging," *Opt. Express* **17**(22), 19486–19500 (2009).
56. A. D. Aguirre, and J. G. Fujimoto, "Optical coherence microscopy. *In Optical coherence tomography,* Springer, Berlin, Heidelberg, 505-542 (2008).
57. A. Dubois, O. Levecq, H. Azimani, D. Siret, A. Barut, M. Suppa, V. Del Marmol, J. Malvehy, E. Cinotti, P. Rubegni, and J. L. Perrot, "Line-field confocal optical coherence tomography for high-resolution noninvasive imaging of skin tumours," *J. Biomed. Opt.* **23**(10), 106007 (2018).
58. S. A. Alexandrov, S. Uttam, R. K. Bista, K. Staton, and Y. Liu, "Spectral encoding of spatial frequency approach for characterization of nanoscale structures," *Appl. Phys. Lett.* **101**(3), 033702 (2012).
59. S. A. Alexandrov, Shikhar Uttam, Rajan K. Bista, Chengquan Zhao, and Yang Liu, "Real-time quantitative visualization of 3D structural information," *Opt. Express* **20**(8), 9203-9214 (2012).
60. S. A. Alexandrov, H. M. Subhash, A. Zam, and M. Leahy, "Nanosensitive optical coherence tomography," *Nanoscale* **6**(7), 3545–3549 (2014).

Chapter 2

Fundamental principles and applications of optical coherence tomography

2.1 Basic Theory

OCT is a non-contact optical imaging technique that is used to perform high-resolution, cross-sectional imaging of internal microstructures in biological systems and materials by measuring the echo time delay and magnitude of backscattered light. All OCT implementations are based on the concept of low-coherence interferometry (LCI) to generate the interference signals [1, 2]. Therefore, a low-coherence interferometry setup is the core of any OCT system. Despite the fact that there are many interference setups, the free space optics-based Michelson interferometric setup illustrated in figure 2.1 will be used to demonstrate the basic concepts of light interference and its function in OCT imaging. Michelson interferometric setup build-up with a low coherence light source, a beam splitter, a detector, a reference arm, and a sample arm. The light from a low coherence light source is split into two paths after the beam splitter and the two beam paths directing along the two different arms of the interferometer. When the light exits from the light source, it is shaped using various optical components such as lenses, apertures, and mirrors. In the sample arm, the light is backscattered from the different layers of the sample. In the reference arm, the light is back-reflected from a reference mirror and it returns into the interference system. The scattered and back-reflected light recombines at the beam splitter after travelling the same path length and it generates an interference pattern when their optical path length difference is within the coherence length of the light source, which is recorded by the detector [3].

When the reference mirror is moved along the propagation direction of light, the returning reference light for different locations of the mirror forms interference patterns with the sample arm backscattered light from the corresponding depths within the sample. That is, an interference will occur at the detector when the

optical path length difference between the two arms is same. For each sample point a single interference pattern detected by the detector is called a depth scan or an A-scan of the OCT signal. Scanning the sample arm beam across the sample surface at each position of the beam forms an OCT image. Hence, a series of A-scans at different locations form an OCT image and it is known as a B-scan or B-frame [4].

In the Michelson interferometric setup, the complex electric field originating from the light source is described as [5]

$$E_i = S(\kappa, \omega)e^{i(\kappa z - \omega t)} \tag{2.1}$$

where κ is the wave number and ω is the frequency component of the light source, t and z are functions of space and time.

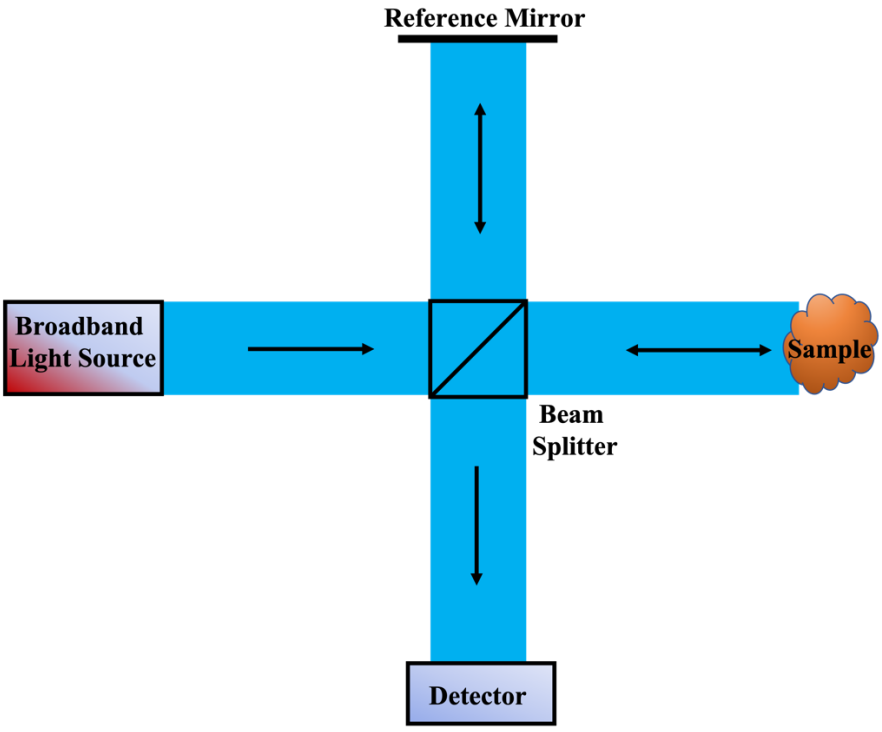

Fig. 2.1 Schematic of a time domain OCT system

As shown in figure 2.1 the electric field passing through the beam splitter after returning from the sample arm, the backscattered electric field can be written as [6],

$$E_S = \frac{E_i}{\sqrt{2}} \sum_{n=1}^{N} r_{sn} e^{-i2kz_n} \quad (2.2)$$

where E_S and E_i are the scattered and incident field. Within the sample, r_{sn} represents the reflectivity of layer *n* at distance z_n.

The electric field passing through the beam splitter after returning from the reference arm, the back reflected electric field can be written as [6],

$$E_R = \frac{E_i}{\sqrt{2}} r_R e^{-i2kz_R} \quad (2.3)$$

E_R and r_R represent the back reflected electric field from the reference arm and reflectivity of the reference mirror. Where z_R is the path length of the reference mirror from the beam splitter. The backscattered and back reflected electric field recombines after passing through the beam splitter and this recombine signal is detected by the photodetector which generates photocurrent. Depending on the path length differences between the two arms constructive and destructive interference occurs. The recombined signal can be written as [6]

$$I(\kappa, \omega) = \frac{\rho}{2} < |E_S + E_R|^2 > = < (E_S + E_R)(E_S + E_R)^* >$$

$$= \frac{\rho}{2} (< E_S E_S{}^* > + < E_R E_R{}^* > + 2®\{< E_R E_R{}^* >\}) \quad (2.4)$$

Expanding equation 2.4 using Euler's rule to generate a real result for the detector current as a function of wave number can be written as [6]

$$I(\kappa) = \frac{\rho}{4} [S(\kappa)(r_{s1} + r_{s2} + r_{s3} + \cdots)] \quad \text{'DC terms'}$$

$$+ \frac{\rho}{2} [S(\kappa) \sum_{n=1}^{N} \sqrt{r_R r_{sn}} (Cos(2k(z_R - z_{sn})))] \quad \text{'Cross correlation terms'}$$

$$+\frac{\rho}{4}\left[\, S(\kappa)\sum_{n\neq m=1}^{N}\sqrt{r_{sm}r_{sn}}\,\left(\, Cos(2k(z_{sm}-z_{sn}))\,\right)\,\right] \quad \text{'Auto correlation terms'} \tag{2.5}$$

Here, ρ is the responsivity of the detector. *S(κ)* is the power spectral density of the light source. r_{sm} and r_{sn} are sample reflectivities at layer *m* and *n* respectively, z_{sm} and z_{sn} are the pathlengths to the layers *m* and *n* within the sample measured from the beam splitter. Equation 2.5 has three different components of the detector. The first term is referred to as 'constant' or 'DC' component. Each sample reflector has a "cross-correlation" component, which is dependent on the light source wavenumber and the path length difference between the reference arm and the sample reflectors. In typical OCT system designs, 'autocorrelation' terms that indicate interference between the different sample reflectors appear as artifacts. The 'cross-correlation' term is the interference between the sample and the reference arm (desired OCT signal) [6].

2.2 Key Performance Metrics of OCT

Several key parameters are used to design, develop, and compare the performance of the OCT systems. The key parameters are the central wavelength and spectral range of the light source, axial resolution, lateral resolution, depth of focus, total imaging depth, roll-off, and sensitivity.

2.2.1 Central Wavelength and Spectral Range

We start with the central wavelength and the spectral range of the light source since it would measure or affect the rest of the key parameters. Generally, depending on the application, three wavelength ranges of OCT systems are frequently used: ~800 nm, ~1064 nm, and 1300 nm. For most ophthalmic applications, ~800 nm centre wavelength OCT system is used because for this particular optical window water absorption is low compared to 1064 nm and 1300

nm wavelength as shown in figure 2.2 [7,8]. Particularly for skin tissue imaging 1300 optical window is used and it can enhance penetration depth and imaging contrast due to low scattering at deeper penetration depth and absorption will be reasonably low. The characteristics of absorption are obtained by analyzing the known spectral absorption of skin components, such as hemoglobin, melanin, and water, along with the scattering properties of the dermis. Recently a few research groups used ~1700 nm centre wavelength OCT system with a broad spectral range for ultra-high-resolution imaging and deep tissue mouse brain imaging [9, 10]. Also, a few research groups used the visible wavelength optical window OCT system for human retina imaging to achieve less than one-micron resolution, where the water absorption is low compared to the 800 nm optical window as shown in figure 2.2 [11].

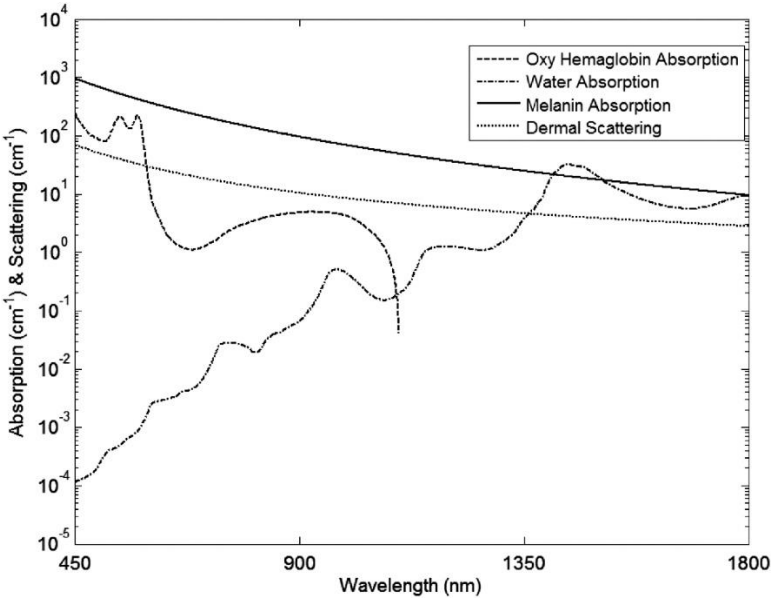

Fig. 2.2 Left y-axis represent absorption coefficients of melanin, oxygenated haemoglobin, and water. Right y-axis represents the scattering coefficient (cm^{-1}) of skin. x-axis represents the wavelength of light source [8].

2.2.2 Axial Resolution

Axial resolution is one of the key parameters of the OCT system, it shows the resolving power of the OCT along the depth direction. Generally, for a Gaussian shape optical spectrum [12] of the light source we can derive the theoretical axial resolution of the OCT system as

$$\Delta z = \frac{2\ln(2)}{\pi n}\frac{\lambda_c^2}{\Delta\lambda_{fwhm}} \tag{2.6}$$

where λ_c is the central wavelength of the light source and $\Delta\lambda_{fwhm}$ is the full width half maximum spectral bandwidth of the light source spectrum. From equation 2.6, it can be observed that the theoretical axial resolution of the OCT system depends on the central wavelength and spectral bandwidth of the light source. However, in the experimental OCT system, the spectral bandwidth of the detected signal is always affected by a few factors like the transmission window and optical property of the optical or optomechanical components and the detection range of the detector [13, 14]. For the broadband light source usually the spectrum shape is not Gaussian and it would affect the axial resolution as well. During the signal processing, the spectral shaping technique can be used to convert Gaussian-shape spectra from non-Gaussian-shaped spectra to suppress the sidelobes. In order to maintain the axial resolution in deeper imaging depth spectral resampling would require if the detected signal were not linearly sampled in wavenumber. Generally, 800 nm and 1300 nm optical window OCT systems the typical axial resolutions are 1-4 μm and 5-10 μm.

2.2.3 Lateral Resolution

Another important parameter of the OCT system is lateral or transverse resolution, it is independent of the bandwidth of the light source and axial resolution. Lateral resolution is determined by the sample arm objective lens beam spot size of the focused beam and the focusing media in front of the sample

[7]. The theoretical lateral resolution follows the Abbe's criteria, which is given by

$$\Delta x = 0.37 \frac{\lambda_c}{NA} \tag{2.7}$$

where λ_c is the central wavelength of the light source. *NA* is the numerical aperture of the sample arm objective lens. *NA* = n sin(α), where α is the angle between the optics axis and the wedge converging beam at the focal plane of the objective lens. *n* is the refractive index of the objective lens glass material.

2.2.4 Depth of Focus

The depth of focus of an OCT system refers to the range of distances over which the system can obtain sharp and well-resolved images. It is a measure of the axial or depth resolution of the OCT system. The theoretical value of the depth of focus or confocal parameter is determined by the following formula

$$\text{DOF} = 2bz_r = \frac{2n\lambda_c}{NA^2} \tag{2.8}$$

where *b* is the confocal parameter and z_r is the Rayleigh range which is twice of the confocal parameter [15, 16]. From the above equation it can be observed that the high *NA* objective lens provide sharp image but only allow shallow depth of focus but may struggle to maintain focus outside of this range. Meanwhile, a low *NA* objective would limit the lateral resolution but provides a broader depth of focus. Depth of focus is a trade-off between axial resolution and imaging range. Most of the OCT imaging system performed using low *NA* lens with higher axial resolution to allowing the system to capture sharp images over a larger depth range. With a longer depth of focus may sacrifice some axial resolution, while a system with a smaller septh of focus provides higher resolution but with a limited range.

2.2.5 Total Measurement range / Imaging depth

For the TDOCT, the measurement range is purely determined by the travel range of the reference mirror translation stage. So, obtained sample reflectivity profile along the depth is depends on the reference mirror movement. For FDOCT, the measurement range is inversely proportional to the spectral sampling interval. The spectral sampling interval is determined by $\Delta\lambda/N$, and the measurement range given by [16, 17]

$$\Delta z = \frac{\lambda_c^2}{4n\Delta\lambda_{full}} N \tag{2.9}$$

where N is the number of pixels or number of sampling points in an axial scan. $\Delta\lambda$ is the bandwidth of the light source. From the above equation it can be observed that for a particular central wavelength if the bandwidth of the light source is increased then the imaging depth will decrease.

2.2.6 Sensitivity and Roll-Off

Sensitivity measurement of an OCT system determines the minimum sample reflectivity, and it can provide a figure of merit for system characterization and evaluation [7, 18]. For the SDOCT system, the theoretical (assumed no optical loss and for Gaussian spectrum) shot noise limit sensitivity is defined as

$$Sensitivity = 10\log\left(\frac{\rho\eta T_{int}}{e} P_0\kappa_s\right) \tag{2.10}$$

where ρ represents the spectrometer efficiency, η denotes quantum efficiency of the detection unit. T_{int} and P_0 are camera integration time and average optical power entering the interferometer, κ_s represents the coupling coefficient of the coupler. Sensitivity roll-off is determined from the decrease in sensitivity with respect to imaging depth. Usually, for all the OCT systems sensitivity decreases by a certain value (like 3 dB, 5 dB, 10 dB) from the peak value within a few millimetres of imaging depth. The finite pixel size of the line detector and the

finite spot size created by the spectrometer optics are the two main factors in the characteristic decrease of sensitivity of the SDOCT.

2.3 Time-domain and Frequency-domain OCT

Since the first implementation of the OCTs, numerous approaches have been explored to develop OCT systems, all based on the fundamental principle of Michelson interferometry. The earlier development of the OCT systems is based on the time-domain [4, 7]. Since the implementation of the OCT systems three main technical approaches are used to develop OCT systems. Currently, all OCT systems used in industry and research fall into one of three categories: time-domain (TDOCT), Fourier-domain/ Spectral-domain (FD/SDOCT) or swept-source (SSOCT). However, for the clinical and commercial purposes spectral-domain OCT systems are mainly used, it has some advantages over the time-domain systems.

TDOCT system is based on the Michelson interferometric detection technique with a low coherence light source and scanning reference delay. The low coherence light split into the two paths by an optical beam splitter. The back reflected light from the reference mirror that is on a controlled translation motion, and it allows the reference light to travel a known path length and to undergo a measurable variable time delay. The backscattered light from the sample arm recombined with the reference light producing interference patterns after travelling the same optical path length. The measured interference pattern or intensity of the combined light detected by the detector is a function of time. Thus, the interference signal provides the sample depth information and the location of various structures within the sample. Unlike the TDOCT, for the FDOCT and SSOCT systems are used stationary reference reflector to measure the intensity of the interferogram as a function of wavelength. Then the measured intensity spectrum relates to the sample depth profile by performing an inverse Fourier transform. In general FDOCT is based on the Fourier relation between the

scattering amplitude and scattering potential [19, 20]. In the FDOCT the returning sample beam comes from the different layers of the backscatters located at various depths which is made up with multiple partial waves. The wavelength dependent spectrum detected by the detector and the detected spectrum is the sum of all the individual interference fringe. In this way FDOCT acquires all data points from all axial depths and one depth profile formed by inverse Fourier transform axial scan produces an A-line. The main difference between the TDOCT and FDOCT detection technique is that the reference arm in a FDOCT system has a static reflector instead of moving one as in TDOCT. In TD-OCT, the depth information is obtained by scanning the reference mirror along the axial direction while measuring the interference signal. However, TD-OCT suffers from limited sensitivity due to the slow scanning speed of the reference mirror, which results in longer acquisition times and increased susceptibility to noise. In contrast, FD-OCT utilizes a spectrally broad light source and measures the spectral interference pattern directly using a spectrometer. The spectrometer captures the interference signals from different depths simultaneously, allowing for fast and parallel acquisition of the depth information. The high-speed data acquisition enables FD-OCT to capture a larger number of interference signals, increasing the signal-to-noise ratio and sensitivity. Due to the static reflector in the reference arm, FDOCT systems are capable of higher data acquisition speeds and higher sensitivity compared to TDOCT system. R. Leitgeb *et al* demonstrated the performane of Fourier domain vs. time domain OCT and shown that FDOCT systems have a larger sensitivity advantage and allow for sensitivities well above 80dB, even in situations with low light levels and high speed detection [21].

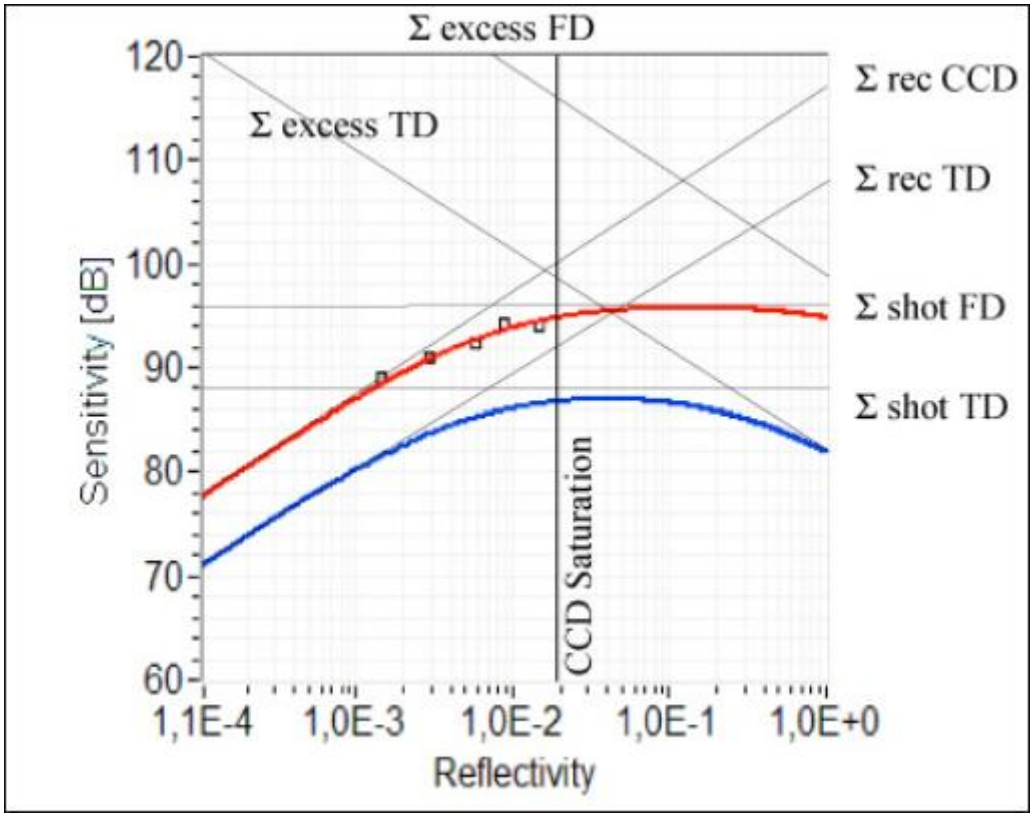

Fig. 2.3 The red line shows the theoretical sensitivity for FDOCT. The blue line is the TDOCT sensitivity for an unbalanced configuration. The squared dots are the actual measured system sensitivities for our FDOCT system [21].

Due to improvements of the light source and detection technology, FDOCT has split into two main approaches: spectral domain OCT (SDOCT) and swept source OCT (SSOCT) [22, 23]. In the SDOCT systems spectrometer is used as a detector on the other hand for the SSOCT system photodiode is used to detect the interference signals. For the SDOCT and SSOCT broadband light sources are used but the SSOCT splits the input light into narrow spectral lines across the available bandwidth of the light source. Swept-source OCT (SS-OCT) is an imaging technique used in OCT that utilizes a tunable laser source to obtain depth information about the sample being imaged. The swept-source laser rapidly sweeps its wavelength across the selected range during data acquisition. As the wavelength is swept, the interference signal is recorded by photodetector at different wavelengths.

In the SDOCT, a broadband light source such as supercontinuum light and a spectrometer are used to detect all the modulated spectral information at the same time from the recombined signals. The spectral interferogram $I_D\,(k)$ is then given by [24]

$$I_D(k) \propto S(k)\sum_{n=1}^{N}\sqrt{R_n R_R}\,(\cos 2k_0 z_n) \tag{2.11}$$

where *S(k)* the optical power density of the light source is described as a function of wavenumber $k = 2\pi/\lambda$. R_R represents the reflectivity of the reference mirror. R_n denotes the backscattered light from the $z_n$depth position of the *N* layers.

To access the sample reflectivity profile, inverse Fourier transform is applied on equation 2.11, which finally yields the A-scan [24]

$$I_D(z) \propto \sum_{n=1}^{N}\sqrt{R_n R_R}\,[\gamma\,(2z_n) + \gamma\,(-2z_n)] \tag{2.12}$$

where the coherence envelope $\gamma(z_n)$ is the inverse Fourier transform of the normalized power spectrum *S(k)*. In equation 2.11, $I_D(k)$ is a real valued function, its complex-valued Fourier transform has an ambiguity between positive and negative frequencies, which gives rise to the mirror terms in equation 2.12. In equation 2.12 only the term shown which encodes the sample properties and it is corresponding represents cross-correlation of the electric field amplitude of the two arms [23]. Generally, a constant DC term and an auto-correlation term together makes self-interference within the sample also it contributes to the final interferogram as well. Follows from equation 2.5, the mathematical form of the final detected sample depth profile (A-line) or detected interferogram after inverse Fourier transform can be written as

$I_D(z) = \frac{\rho}{8}[\gamma(z)(\,r_{s1} + r_{s2} + r_{s3} + \cdots)]$ 'DC terms'

$+\frac{\rho}{4}[\,\gamma(z)\sum_{n=1}^{N}\sqrt{r_R r_{sn}}\,(\gamma[2(z_R - z_{sn})] + \gamma[-2(z_R - z_{sn})]\,]$ 'Cross correlation terms'

$+\frac{\rho}{8}[\,\gamma(z)\sum_{n\neq m=1}^{N}\sqrt{r_{sm}r_{sn}}\,(\,\gamma[2(z_R-z_{sn})]+\,\gamma[-2(z_R-z_{sn})]\,]$ 'Auto correlation terms' (2.13)

r_{sm} and r_{sn} are represent sample reflectivity at layers *m* and *n* respectively, z_{sm} and z_{sn} are the path lengths to the layers *m* and *n* within the sample measured from the beam splitter.

2.4 Imaging Application using OCT

Since the development of OCT, medical imaging applications are still dominating using OCT [25]. In 1991 Fujimoto first reported OCT application in ophthalmology [1]. Advances in OCT technology have made it possible to use in a wide variety of medical and surgical applications, including gastroenterology, dermatology, cardiology, oncology, and others. Apart from the medical imaging applications, OCT has a few non-medical applications such as material science, structural analysis of polymer composites, sensor technology, and others [25]. OCT has some specific advantages compared with other optical techniques such as depth resolution is independent of the sample beam aperture and the coherence gate can substantially improve the probing depth in scattering media. Also, resolution and sensitivity of the OCT are high compared to non-optical imaging modalities. However, the biggest limitation of OCT compared to other imaging modalities in medical imaging is limited penetration depth in scattering media up to a few millimetres [27].

2.4.1 OCT in Ophthalmology

The first ophthalmic imaging application was based on the time-domain OCT [1]. Between the years 1995 and 2005 clinical trials were conducted using TDOCT by many research groups. They have confirmed the usefulness of the cross-sectional eye tissue images in medical diagnosis [28-31]. Due to the low imaging

speed of the TDOCT, resolution and sensitivity of the cross-section image was not sufficient to detect small pathological changes. To image the human eye, especially such structures as conjunctiva, cornea with a tear film, crystalline lens, optic nerve head, and retina FDOCT with visible or near-infrared light source is appropriate choice. Using FDOCT first retinal image were shown in 2002 with a moderate imaging speed of 1000 A-scans/Second [32]. Over the year OCT technique has improved due to advanced technology. Currently, ultrahigh-resolution SDOCT is the standard for ophthalmic applications with the imaging speed (A-scan/Second) range 128-250 kHz. Retinal images with 2.7 microns axial resolution at 840 nm ultrahigh resolution SDOCT have been demonstrated. OCT has already become a standard method for investigating the posterior region of the eye particularly for the retinal imaging.

2.4.2 OCT in Gastroenterology and Dermatology

Gastroenterological OCT was first described by Izatt *et al* in 1996. They showed that OCT images can describe internal histological-level tissue microstructure in bulk gastrointestinal (GI) tissue samples [33]. Rollins *et al* showed that endoscopic OCT imaging clearly observes the substructure of the mucosa and submucosa in GI organs and details structures such as glands, blood vessels, pits, villi, and crypts. Over the year endoscopic OCT tools have been developed to diagnose and investigate clinical problems of the gastrointestinal (GI) tract including the oesophagus, stomach, small intestine, and colon [34, 35]. Recently, with the development of FDOCT techniques using broadband light sources, endoscopic OCT images have been improved with high imaging speed and close to sub-cellular level resolution [36].

OCT was first described in dermatology applications in 1997 [37]. OCT is less established in the field of dermatology because the scattering of light strongly limits the penetration depth into the skin. To overcome these issues longer wavelengths (typically around 1300 nm centre wavelength) are chosen for skin

Imaging. In the longer wavelength region, it can enhance the penetration depth due to low scattering and reasonably low absorption [38]. Another important parameter of the OCT is resolution to recognize the details of the structures in the skin. To improve the resolution beyond regular OCT, the longer wavelength region broadband light sources has been used with FDOCT technique [39]. From the last decade in dermatology applications, OCT has been increasingly used for variety of skin diseases, monitor treatment response, and plan excisions of skin cancers and non-cancerous skin diseases [40]. Figure 2.3 represent the 3D OCT *in vivo* image of the human skin [41].

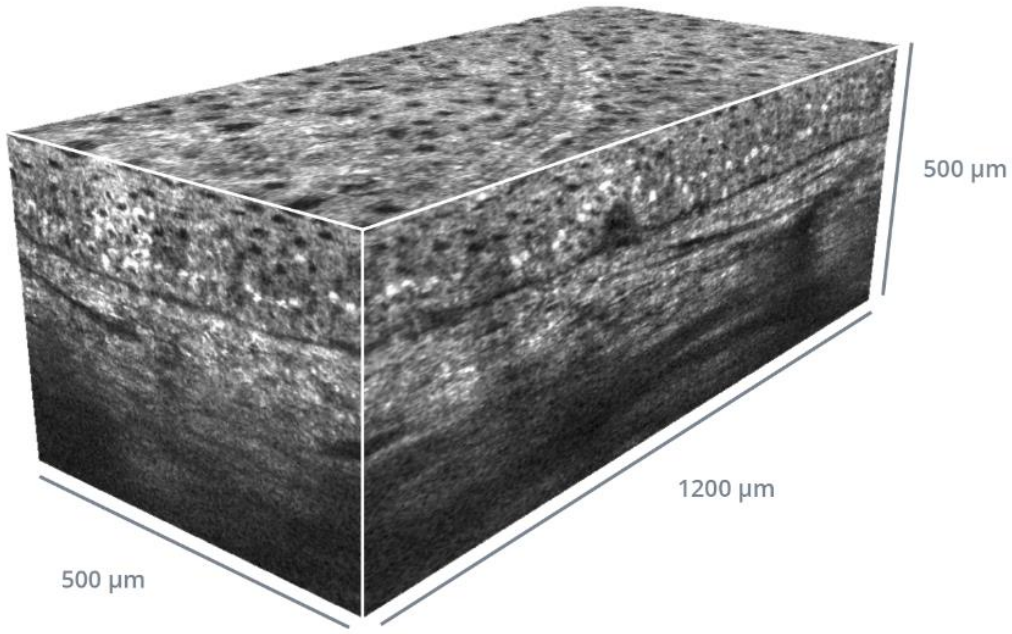

Fig. 2.4 High-resolution *in vivo* 3D OCT image of healthy hman skin [41].

2.4.3 OCT in Other Biomedical Applications

OCT has been used to images the heart and blood vessels and it is able to produce three-dimensional images with cellular/subcellular axial resolution within a few millimetres scale penetration depth. Xinwen Yao *et al* demonstrated the feasibility of OCT to examine myocardium specimens from fresh human and swine hearts [42-43]. To visualize the dental structures OCT has been used. A. Z. Freitas *et al* showed the clinical advantage of the OCT technique to make qualitative and quantitative analysis of dental health from the 3D images of a dental microstructure [44, 45].

2.4.4 OCT in Developmental Biology

OCT is ideally suited for monitoring the growth and development of biological tissues due to its high-resolution, real-time, and noninvasive imaging capabilities. To understand the formation of functional organs requires observation of dynamic changes in the cellular architecture. OCT provides the capability to image the functional and morphological changes in the living biology model [46]. Spectral domain OCT technique is being used as a new technique to image biological events at early stage of growth that take place in organisms [47].

2.4.5 OCT in Material Imaging

White light-based low coherence interferometry has been used for many years in metrological based industry a position sensor [48], and thickness measurement of thin films. Using broadband light, Denkers *et al* showed the application of OCT in non-destructive evaluation of highly scattering polymer-matrix composites to estimate residual porosity, fibre architecture, and structural integrity [49]. Bashkansky *et al* shown detection of the subsurface extent of the Hertzian crack on the surface of a silicon nitride ball from the OCT images [50]. Spectral domain OCT technique is widely used to sensor technology [51, 52] due to its high sensitivity and fast imaging speed.

2.5 Conclusion

In this chapter, we introduced basic working principles, theoretical framework, and key performance metrics of the optical coherence tomography. Three types of OCT were introduced including time-domain, spectral domain, and swept source OCTs. Also, this chapter described the advantages of Fourier domain OCT compared to earlier development of the TDOCT. Various key performance metrics such as central wavelength and spectral range of the light source, axial resolution, lateral resolution, depth of focus, total imaging depth, roll-off and sensitivity were discussed in this chapter. Further, a brief description of OCT applications in all different aspects were discussed, mainly based on biomedical research and clinical or industrial applications.

References

1. D. Huang, E. A. Swanson, C. P. Lin, J. S. Schuman, W. G. Stinson, W. Chang, M. R. Hee, T. Flotte, K. Gregory, C. A. Puliafito, and J. G. Fujimoto, "Optical Coherence Tomography," *Science* **254**(5035), 1178–1181 (1991).
2. J. G. Fujimoto, C. Pitris, S. A. Boppart, and M. E. Brezinski, "Optical Coherence Tomography: An Emerging Technology for Biomedical Imaging and Optical Biopsy," *Neoplasia* **2**(1-2), 9–25 (2000).
3. W. Drexler, J. G. Fujimoto, *Optical Coherence Tomography: Technology and Application* (Singer Berlin Heidelberg, 2008).
4. D. P. Popescu, L. P. Choo-Smith, C. Flueraru , Y. Mao, S. Chang , J. Disano, S. Sherif, M. G. Sowa, "Optical coherence tomography: fundamental principles, instrumental designs and biomedical applications," *Biophys. Rev.* **3**(3), 155-169 (2011).

5. D. J. Griffiths, "*Introduction to electrodynamics*." (American Association of Physics Teachers, 2005).
6. J. A. Izatt and M. A. Choma, "Theory of Optical Coherence Tomography," in *Optical Coherence Tomography* Springer Berlin Heidelberg, 47–72 (2008).
7. M. Wojtkowski, "High-speed optical coherence tomography: basics and applications," *Appl. Opt.* **49**(16), 30–61 (2010).
8. M. J. Mendenhall, A. S. Nunez, and R. K. Martin, "Human skin detection in the visible and near infrared," *Appl. Opt.* **54**(35), 10559-10570 (2015).
9. N. Nishizawa, H. Kawagoe, M. Yamanaka, M. Matsushima, K. Mori, and T. Kawabe, "Wavelength Dependence of Ultrahigh-Resolution Optical Coherence Tomography Using Supercontinuum for Biomedical Imaging," *IEEE J. of Sel. Top. Quantum Electron.* **25**(1), 1-15 (2019).
10. S. P. Chong, C. W. Merkle, D. F. Cooke, T. Zhang, H. Radhakrishnan, L. Krubitzer, and V. J. Srinivasan, "Noninvasive, *in vivo* imaging of subcortical mouse brain regions with 1.7 μm optical coherence tomography," *Opt. Lett.* **40**(21), 4911-4914 (2015).
11. J. Yi, S. Chen, X. Shu, A. A. Fawzi, and H. F. Zhang, "Human retinal imaging using visible-light optical coherence tomography guided by scanning laser ophthalmoscopy," *Biomed. Opt. Express* **6**(10), 3701-3713 (2015).
12. R. Tripathi, N. Nassif, J. S. Nelson, B. H. Park, and J. F. de Boer, "Spectral shaping for non-Gaussian source spectra in optical coherence tomography," *Opt. Lett.* **27**(6), 406-408 (2002).
13. A. C. Akcay, J. P. Rolland, and J. M. Eichenholz, "Spectral shaping to improve the point spread function in optical coherence tomography," *Opt. Lett.* **28**(20), 1921-1923 (2003).

14. R. A. Leitgeb, W. Drexler, A. Unterhuber, B. Hermann, T. Bajraszewski, T. Le, A. Stingl, and A. F. Fercher, “Ultrahigh resolution Fourier domain optical coherence tomography,” *Opt. Express* **12**(10), 2156-2165 (2004).
15. M. Born and E. Wolf, *Principles of Optics* (Sixth Edition) Pergamon, 1980.
16. W. Drexler, M. Liu, A. Kumar, T. Kamali, A. Unterhuber, and R. A. Leitgeb, “Optical coherence tomography today: speed, contrast, and multimodality,” *J. Biomed. Opt.* **19**(7), 071412 (2014).
17. T. Klein and R. Huber, “High-speed OCT light sources and systems,” *Biomed. Opt. Express* **8**(2), 828-859 (2017).
18. J. F. de Boer, R. Leitgeb, and M. Wojtkowski, “Twenty-five years of optical coherence tomography: the paradigm shift in sensitivity and speed provided by Fourier domain OCT,” *Biomed. Opt. Express* **8**(7), 3248–3280 (2017).
19. M. Born and E. Wolf, Principles of Optics: *Electromagnetic Theory of Propagation, Interference and Diffraction of Light* (Elsevier, 2013).
20. A. F. Fercher, C. K. Hitzenberger, G. Kamp, and S. Y. El-Zaiat, “Measurement of intraocular distances by backscattering spectral interferometry,” *Opt. Commun.* **117**(1-2), 43–48 (1995).
21. R. Leitgeb, C. K. Hitzenberger, and A. F. Fercher, "Performance of fourier domain vs. time domain optical coherence tomography," Opt. Express 11, 889-894 (2003)
22. R. Leitgeb, C. Hitzenberger, and A. Fercher, “Performance of fourier domain vs. time domain optical coherence tomography,” *Opt. Express* **11**(8), 889–894 (2003).
23. S. Aumann, S. Donner, J. Fischer, and F. Müller, “Optical Coherence Tomography (OCT): Principle and Technical Realization,” *High Resolution Imaging in Microscopy and Ophthalmology*, 59–85 (Springer, 2019).

24. J. F. Bille, *High Resolution Imaging in Microscopy and Ophthalmology* (Springer, 2019).
25. B. E. Bouma and G. J. Tearney, *Handbook of Optical Coherence Tomography* (New York: Marcel Dekker, 2002).
26. A. F. Fercher, W. Drexler, C. K. Hitzenberger, and T. Lasser, "Optical coherence tomography-principles and applications," *Rep. Prog. Phys.* **66**(2), 239 (2003).
27. I. Y. Wong, H. Koizumi, and W. W. Lai, "Enhanced depth imaging optical coherence tomography," *Ophthalmic Surg. Lasers Imaging* **42**(4), 75-84 (2011).
28. M. R. Hee, C. A. Puliafito, C. Wong, J. S. Duker, E. Reichel, J. S. Schuman, E. A. Swanson, and J. G. Fujimoto, "Optical coherence tomography of macular holes," *J. Ophthalmol.* **102**(5), 748–756 (1995).
29. J. A. Izatt, M. R. Hee, E. A. Swanson, C. P. Lin, D. Huang, J. S. Schuman, C. A. Puliafito, and J. G. Fujimoto, "Micrometer scale resolution imaging of the anterior eye *in vivo* with optical coherence tomography," *Arch. Ophthalmol.* **112**(12), 1584–1589 (1994).
30. J. S. Schuman, C. A. Puliafito, and J. G. Fujimoto, *Optical Coherence Tomography of Ocular Diseases*, 2nd ed. (Slack Inc., 2004).
31. R. A. Costa, M. Skaf, L. A. Melo, Jr., D. Calucci, J. A. Cardillo, J. C. Castro, D. Huang, and M. Wojtkowski, "Retinal assessment using optical coherence tomography," *Prog. Retin. Eye Res.* **25**(3), 325–353 (2006).
32. M. Wojtkowski, R. Leitgeb, A. Kowalczyk, T. Bajraszewski, and A. F. Fercher, "*In vivo* human retinal imaging by Fourier domain optical coherence tomography," *J. Biomed. Opt.* **7**(2), 457–463 (2002).
33. J. A. Izatt, M. D. Kulkarni, H. W. Wang, K. Kobayashi, and M. V. Sivak, "Optical coherence tomography and microscopy in gastrointestinal tissues," *IEEE J. of Sel. Top. Quantum Electron.* **2**(4), 1017-1028 (1996).

34. T. H. Tsai, C. L. Leggett, A. J. Trindade, A. Sethi, A.-F. Swager, V. Joshi, J. J. Bergman, H. Mashimo, N. S. Nishioka, and E. Namati, "Optical coherence tomography in gastroenterology: a review and future outlook," *J. Biomed. Opt.* **22**(12), 121716 (2017).
35. T. H. Tsai, J. G. Fujimoto, and H. Mashimo, "Endoscopic Optical Coherence Tomography for Clinical Gastroenterology," *Diagnostics* **4**(2), 57–93 (2014).
36. F. Prati, M. W. Jenkins, A. Di Giorgio, and A. M. Rollins, "Intracoronary optical coherence tomography, basic theory and image acquisition techniques," *Int. J. Cardiovasc. Imaging* **27**(2), 251–258 (2011).
37. J. Welzel, E. Lankenau, R. Birngruber, R. Engelhardt, "Optical coherence tomography of the human skin," *J. Am. Acad. Dermatol.* **37**(6), 958-963, (1997).
38. N. M. Israelsen, M. Maria, M. Mogensen, S. Bojesen, M. Jensen, M. Haedersdal, A. Podoleanu, and O. Bang, "The value of ultrahigh resolution OCT in dermatology-delineating the dermo-epidermal junction, capillaries in the dermal papillae and vellus hairs," *Biomed. Opt. Express* **9**(5), 2240-2265, (2018).
39. Y. Pan, and D. L. Farkas, "Non-invasive imaging of living human skin with dual-wavelength optical coherence tomography in two and three dimensions," *J. Biomed. Opt.* **3**(4), 446-455 (1998).
40. M. Nasiriavanakia, J. W. Fakhourya, S. Daveluya, "OCT image atlas of healthy skin on sun-exposed areas," *Skin Res Technol.* **24**(4), 570-586 (2018).
41. J. Ogien, O. Levecq, H. Azimani, and A. Dubois, "Dual-mode line-field confocal optical coherence tomography for ultrahigh-resolution vertical and horizontal section imaging of human skin in vivo" Biomed. Opt. Express **11***(*3), 1327-1335 (2020).

42. X. Yao, Y. Gan, C. C. Marboe, and C. P. Hendon, “Myocardial imaging using ultrahigh-resolution spectral domain optical coherence tomography,” *J. Biomed. Opt.* **21**(6), 061006 (2016).
43. J. G. Fujimoto, S. A. Boppart, G. J. Tearney, B. E. Bouma, C. Pitris, and M. E. Brezinski, “High resolution *in vivo* intra-arterial imaging with optical coherence tomography,” *Heart* **82**(2), 128–133, (1999).
44. L. L. Otis, B. W. Colston, M. J. Everett, and H. Nathel, “Dental optical coherence tomography: A comparison of two in vitro systems,” *Dentomaxillofac Radiol.* **29**(2), 85–89 (2000).
45. A. Z. Freitas, D. M. Zezell, N. D. Vieira, A. C. Ribeiro, and A. S. L. Gomes, “Imaging carious human dental tissue with optical coherence tomography,” *J. Appl. Phys.* **99**(2), 024906 (2006).
46. A. M. Davis, S. A. Boppart, F. Rothenberg, and J. A. Izatt, “*OCT Applications in Developmental Biology*,” Springer, 919–959 (2008).
47. L. I. Jian-ping, L. I. Dong. “Applications of OCT Technique in Developmental Biology,” *Appl. Opt.* **26**(2), 60-64, (2005).
48. T. Li, A. Wang, K. Murphy, and R. Claus, “White-light scanning fibre Michelson interferometer for absolute position-distance measurement,” *Opt. Lett.* **20**(7), 785-787 (1995).
49. J. P. Dunkers, R. S. Parnas, C. G. Zimba, R. C. Peterson, K. M. Flynn, J. G. Fujimoto, and B. E. Bouma, “Optical coherence tomography of glass reinforced polymer composites,” *Compos. Part A Appl. Sci. and Manufacturing* **30**(2), 139-145 (1999).
50. M. Bashkansky, D, Lewis Iii, V. Pujari, J. Reintjes, and H. Y. Yu, “Subsurface detection and characterization of Hertzian cracks in Si3N4 balls using optical coherence tomography,” *Ndt & E International* **34**(8), 547-555 (2001).
51. K. M. Kennedy, S. Es’haghian, L. Chin, R. A. McLaughlin, D. D. Sampson, and B. F. Kennedy, “Optical palpation: Optical coherence

tomography based tactile imaging using a compliant sensor," *Opt. Lett.* **39**(10), 3014–3017 (2014).

52. D. Culemann, A. Knuettel, and E. Voges, "Integrated optical sensor in glass for optical coherence tomography," *IEEE J. of Sel. Top. Quantum Electron.* **6**(5), 730–734 (2000).

Chapter 3

Development and simple characterization scheme of fibre-based near-isometric high-resolution optical coherence tomography system

3.1 Introduction

Optical coherence tomography (OCT) is a high speed, noncontact, non-invasive imaging technology that provides high axial resolution to depths of 1 to 2 millimetres within biological samples [1, 2]. OCT is a powerful imaging technique which facilitates depth resolved information from interferometrically separated backscattered photons from different layers of samples. OCT is widely used for both structural and functional imaging applications for disease diagnosis such as that of the eye [3, 4], heart and blood vessels [5–8], tumours [9, 10], visualization of dental structure [11–13], diagnosis and treatment of skin disorders [14–16]. OCT is used for imaging in material science [17], structural analysis of polymer composites [18, 19], sensor technology [20, 21], among many other applications. Spectral-domain OCT (SDOCT) is a widely used modality due to its high sensitivity and fast imaging speed [22–26].

The axial resolution of OCT system is determined by the characteristics of the light source. Specifically, it is inversely proportional to the bandwidth of the light source and proportional to the square of the central wavelength of the light source [27]. With the development of high-resolution spectral-domain OCT (HR-SDOCT), supercontinuum generation light sources have attracted much attention in the last two decades. Supercontinuum generation light sources have several advantages over super luminescent diodes such as high output power, extremely broad spectral bandwidth, and a comparatively high degree of spatial coherence. M. Szkulmowski *et al.* first demonstrated a free space spectral domain OCT system with a supercontinuum light source for high resolution *in vivo* imaging, and achieved 4 μm axial OCT image resolution and 20 μm lateral resolution in the 0.75 μm to 0.95 μm spectral window [28]. Suitable spectral bandwidth for

deep imaging in tissue is around of 1300 nm P. Cimalla *et al.* demonstrated a dual-band, free space SDOCT system based on a supercontinuum laser. They reported 4.5 μm and 7 μm axial resolution in air within the spectral windows of 0.7 μm to 0.9 μm and 1.1 μm to 1.4 μm, respectively [29]. These proposed supercontinuum SDOCT systems were mainly based on free-space optics. Several OCT research groups have developed free-space TDOCT and SDOCT [6, 30] systems using supercontinuum light sources but only a few research groups have demonstrated supercontinuum source and fibre-based SDOCT systems (Table 3.1) centred at 1300 nm wavelength corresponding to an axial and lateral resolution of 8 μm and 15 μm in air [31, 32]. M. Maria *et al.* compared the noise performance of three different supercontinuum light sources using a fibre-based OCT configuration [33]. Although, it is to be expected that the axial resolution may improve with increased spectral bandwidth, we discuss the air-wedge method for direct evaluation of the axial resolution. Also, more accurate characterization may become more relevant for fibre-based OCT systems in the future, to provide improved tuning and calibration. More- over, our system design evaluates the use of a high NA sample lens to improve isometry of the image voxel, which becomes relevant with improved axial resolution. Although many system designs try to maximize imaging depth using lower NA sample lenses, high NA sample lenses are of interest for improved sensitivity to small structures in shallower sample regions, such as for skin cancer detection. K. C. Zhou *et al.* and C. K. Chang *et al.* have discussed the importance of isometric resolution in OCT [34–36].

As the system designed for this study is intended for skin imaging, a centre wavelength at 1300 nm was chosen because it offers the best compromise between penetration depth, water absorption, and axial resolution. In biological applications, scattering and water absorption are highly dependent on the wavelength of the light source. In the longer wavelength region, it can enhance penetration depth and imaging contrast due to low scattering at deeper penetration

depths where multiple scattered photons dominate over ballistic photons [37, 38], and absorption will be reasonably low.

A fibre-based SDOCT system has advantages over free space regarding commercialized designs. Fibre-optics are easier to assemble, have better stability (less sensitive to vibration, airflow, and temperature fluctuation), and handling is simplified, which may be important for the construction of future medical imaging devices.

In this chapter, we present a high axial resolution of 3.7 μm based on the bandwidth of the light-source and a measured resolution in air of 3.8 μm. We experimentally validate a lateral resolution of 5.5 μm using a USAF target with a fibre-based HR-SDOCT system with a supercontinuum light source and a spectral window between 1100 nm to 1500 nm. We also provide a more rigorous analysis using an air-wedge for the characterization and validation of the axial resolution. The maximum sensitivity was measured to be 109 dB at an A-line rate of 73 kHz averaging 1024 A-lines. We demonstrate imaging on biological tissue, including qualitative discussion.

Table 3.1
Public reported axial resolution of fibre-optic based HR-SDOCT systems with centre wavelength of 1300nm

Authors	Axial resolution (μm)	Lateral resolution (μm)
Yi-Jing You, et al., Laser Phys. Lett., 2015 [31].	8.1 (air)	Not stated.
C. Chen, et al., Biomed. Opt. Express., 2018 [32].	8 (air)	15
M. Maria et al., Proc. Of SPIE, 2017 [33].	4 (air)	Not stated.
Presented System	3.8 (air)	5.5

Along with the OCT system characterization, we evaluate a low-cost air-wedge-based measurement standard. Many publications suggest a wide variety of OCT

phantoms that are often difficult to replicate or impossible to obtain commercially. For instance, the APL-OP01 OCT phantom (Arden photonics Ltd.) is a valuable and easily applicable standard that characterizes essential parameters for OCT systems. Whereas the commercial phantom provides good repeatability of geometric structures and allows characterizing the PSF on inscribed reflectors and different depth positions, it would not allow direct measurement of the axial resolution limits as it would be difficult to provide embedded reflecting structures with known size and sufficient accuracy. Laser inscription of structures into fused silica is a favoured method in laboratories that have suitable laser equipment and expertise to create phantoms with known structures [39]. Also, the air wedge using standard microscope slides will not be able to provide high accuracy. However, a user or a well-equipped laboratory may find it easy to modify the construction with more accurate methods and materials, offering the flexibility to design a phantom for specific characterization goals. For instance, different wedge slopes may be of interest in studying the impact of interference artefacts on closely spaced structures and layers. Moreover, the wedge can be embedded in different liquids to study different effects due to refractive index changes and dispersion still having the capability to modify the wedge spacing.

3.2 Materials and Methods

3.2.1 Experimental System Setup

For this study, no detailed evaluation of the relative intensity noise (RIN) was performed, as it would not contribute significantly to the evaluation of the axial resolution. The supercontinuum light source (SuperK EXU6, NKT Photonics) is advertised for OCT applications, suggesting that the RIN values are better than 100 dB. Our system design (see schematic Fig. 1) uses a low noise, non-polarized, supercontinuum light source (SuperK EXU6, NKT Photonics) with a central

wavelength of 1300 nm (SC Laser). The bandwidth of the light source spectrum was reduced to about 400 nm using a short pass filter (Edmund optics, SN: 84656, OD2, wavelength range: 810-2025 nm, transmission wavelength: 810-1540 nm, rejection wavelength: 1700-2025 nm) and long pass filter (Semrock, SN: BLP01-1064R-25, transmission band: 1093.8-1600 nm). The output power is attenuated using an optical splitter (SuperK connect, NKT Photonics, wavelength range 400-2000 nm). A broadband fibre delivery system (SuperK FD5 non-PM, NKT Photonics, wavelength range 950-1530 nm) is used to inject the light source into the Michelson interferometer (MI). To avoid back propagation of light to the light source, an optical circulator is used (Precision Micro-Optics, 1310 nm SM Circulator, SN: 2017123002).

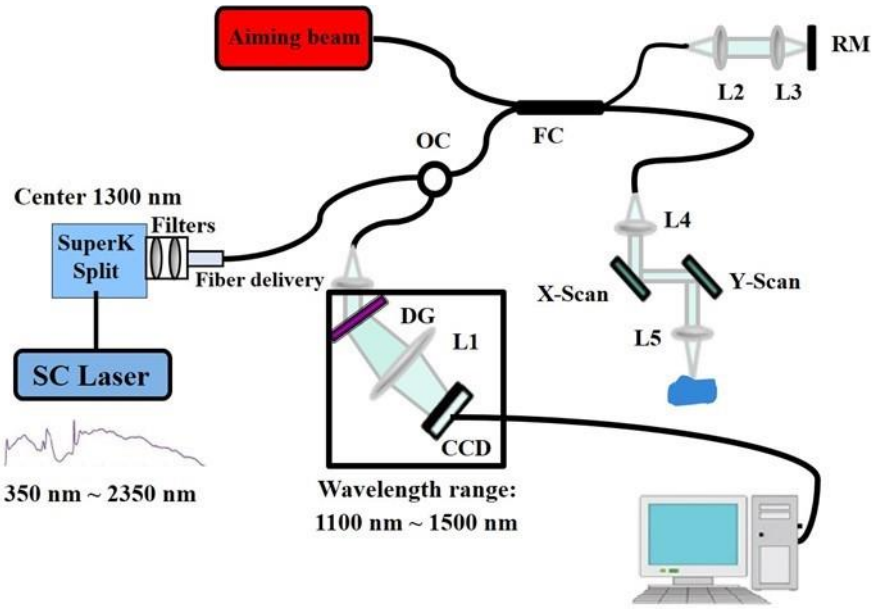

Fig. 3.1 Schematic of fibre based high-resolution spectral domain OCT system. SC Laser: Supercontinuum laser source, SuperK splitter, Long pass, short pass and neutral density filters, OC: Optical Circulator, FC: 2×2 fibre coupler. L: Lenses, L5: Objective lens, RM: Reference mirror, X-Y Galvo, DG: Diffraction Grating.

The MI is constructed using a 90/10 beam splitter (Thorlabs, SN: T030932, 2×2 90:10 wideband coupler) providing 90 per- cent sample arm power and 10 percent reference arm power (FC). For the sample arm fibre, a collimator (L4) with a focal length f = 11 mm is used (Thorlabs, Inc., Part No. F280APC-C) projecting the beam onto an X-Y galvanometer (Thorlabs, Part No. GVS112). The sample objective lens (L5) is an Mitutoyo Plan Apo with 10× magnification, NA = 0.26, and f = 20 mm (Edmund Optics, Parts No. 378-823-5). For the reference arm, another collimator (L2) of the same type is used. The reference mirror (RM) is gold coated (Thorlabs, SN: ME1-M01) and for focusing, an achromatic doublet (Thorlabs, Achromatic Doublet, f = 19 mm) is used. For dispersion compensation, a 2 mm thick optical window between L2 and L3 is used (not shown in schematic). Tuning the dispersion compensation was performed by successively changing the path delay in the reference arm using different optical thicknesses while measuring the point-spread function. The output port of the circulator (OC) is connected to the spectrometer (Wasatch Photonics, Cobra 1300). The high-speed camera (CCD) is connected to the CameraLink frame grabber (Teledyne Dalsa, X64 Xcelera-CL PX4 Dual) and triggered by a digital input/output board. For lateral scanning, a two-axis galvo scanning system (Thorlabs, GVS112) is connected to a PCIe 6321 multifunctional I/O device (National Instrument, PCIe 6321). We developed custom software in LabVIEW for hardware control and data acquisition. Although for visualization, some pre-processing was performed in LabVIEW, signal and image processing of the raw data was performed in MATLAB. Signal and image processing steps included **K**-space linearization, spectral windowing (Hann), inverse Fast-Fourier Transform, and intensity log-scaling for display. The Hann window was selected due to its minimal spectral leakage and the optimal reproduction of the PSF [40].

3.2.2 Custom build LabVIEW program

LabVIEW (Laboratory Virtual Instrument Engineering Workbench) is a graphical programming language that uses icons instead of lines of text to create applications. Unlike text-based programming languages, where the order of program execution is determined by instructions, LabVIEW Dataflow programming is used, in which data flows through nodes on the network. The execution sequence of the VIs and functions is determined by the block diagram. In LabVIEW, we build a user interface by using a set of tools and objects. The user interface is also known as the front panel. Figure 3.2(a) represents the flow chart of our custom builds LabVIEW program. A few interfaces have been built to control the OCT system, mainly 2D Galvo scanner synchronized with spectrometer to acquire the data. Multiple loops and queues have been used to run the programs. First, we initialized the hardware connection with some internal settings and after that, we passed some comments to the camera to make it ready for acquiring the data. The high-speed camera (CCD) is connected to the CameraLink frame grabber (Teledyne Dalsa, X64 Xcelera-CL PX4 Dual) and triggered by a digital input/output data acquisition (DAQ) board. After calculating the one loop for one B-frame the DAQ sends them for graphical display. From the graphical display after visualizing the position of the sample we saved the spectral raw data and ended one loop. For 3D data acquisition, we captured several hundred B-frames by scanning each location of the object using X-Y Galvo scanner. To control the scanning range, we used different input voltages for the Galvo scanners. To acquire the 3D data, we followed raster scanning patterns. In figure 3.2(b) the bottom diagram represents the scanning pattern using X-Y Galvo. In figure 3.2(b) the right-side diagram represents the X-Y Galvo movement with the trigger mode of the camera. Trigger mode is used to begin on the rising or falling edge of a digital signal. The one rising sample corresponds to the X-Galvo movement. The frame rate depends on how many

sample points (corresponding to A-lines/A-scan) are captured in one B-frame. In figure 3.2(b), left side blue and green panels represent the X-Y Galvo setting parameters.

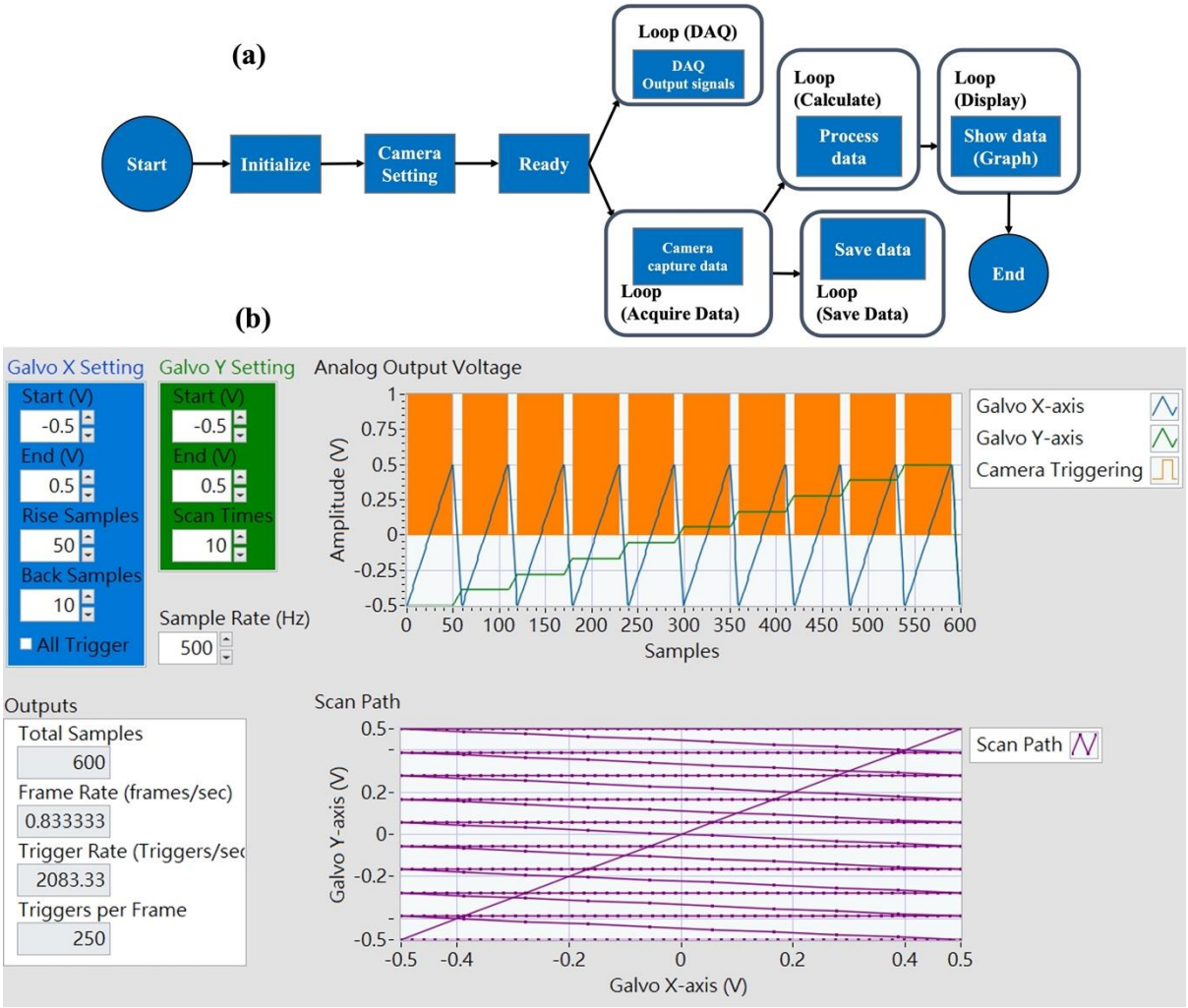

Fig. 3.2 (a) Represent the flowchart of the LabVIEW program. (b) interface of the X-Y Galvo setting parameters and scanning pattern.

3.2.3 Air Wedge Theory and Construction

The in-air axial resolution of OCT systems is conventionally provided based on the bandwidth of the used light source, and the point spread function (PSF) can be measured based on a mirror reflection in the sample arm of the Michelson interferometer. Some research groups are using beads embedded in a semi-transparent medium to demonstrate sensitivity and resolution, but preparation and lifetime limits access and usability. For lens based optical systems such as microscopes and telescopes the resolution limit is defined based on certain criteria, such as the better-known Rayleigh criterion, but also the Sparrow, Ricker Dawes's criterion, and most importantly the Abbé diffraction limit [41–46]. All criteria describe the resolution limit based on the separation of two PSF's that are mathematically described by the Airy function. The Airy function can be approximated with a Gaussian, which allows the measurement of the axial PSF of OCT systems with a Gaussian light source and using two reflecting surfaces or layers in the sample arm of the system's interferometer.

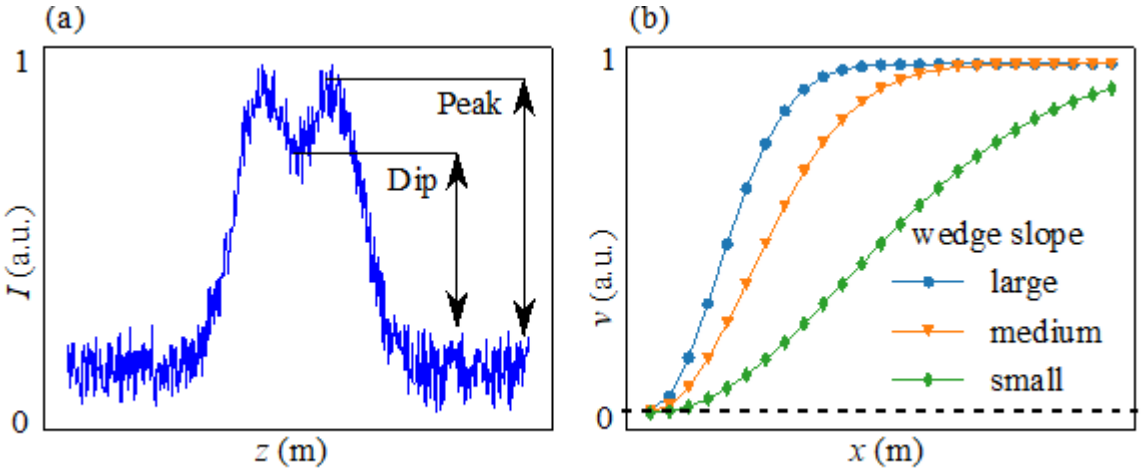

Fig. 3.3 Plot (a) shows the numerical simulation based on equation (2). An arbitrary intensity profile *I* along the depth axis *z*, exhibiting a noisy double peak with a noticeable dip, can be observed. Plot (b) shows the simulated noiseless visibility *v* (*v* = *p*–*d*; *p* ...peak height, *d* ...dip height) for two peaks originating

from a wedge reflection that move closer together along a lateral position *x*. The true size of depth *z* and *x* will be in the millimetre range and is not to scale for illustrative purpose. Best visibility would be achieved at $d = 0$ and $p = 1$ corresponding to a peak of unity intensity. The three different plots relate to different wedge slopes or wedge spacing. The “narrow” curve relates to a thin spacing or shallow slope, “medium” some spacing between narrow and wide, and “wide” is the largest spacing or slope. The peaks would be fully merged at $x = 0$ (left) corresponding to the touching end of the wedge and fully separated for *x* position to the right. The ideal visibility starts to drop if the peak distance becomes smaller than the peak width. Without noise, the ideal visibility can be computed up to zero value.

Although the theory of measuring the optical resolution and image quality is well understood, the process to perform accurate measurements requires suitable equipment depending on precision and accuracy required. This is especially true for OCT if one tries to plan for a suitable reflection standard that can generate two axial PSF’s with sufficient accuracy. Nevertheless, we show that the noise is a major factor which limits measurement accuracy and a low-cost optical air-wedge may be sufficient for general characterization of the axial resolution of an OCT system.

We designed therefore a low-cost method to measure the axial resolution of OCT systems using a simple air wedge made of two microscope slides, Scotch tape and aluminium tape (Section 3.3.4, Fig. 3.9). The air wedge is then moved along its length *L* and imaged multiple times at a position x depending on the scan range of the used OCT system. Although a translational stage can provide better positioning accuracy, price and size may not be suitable for all systems and would not help to get a continuous wedge image. We therefore designed suitable

software that can process, align and position the imaged segments relative to each other based on the visible wedge spacing.

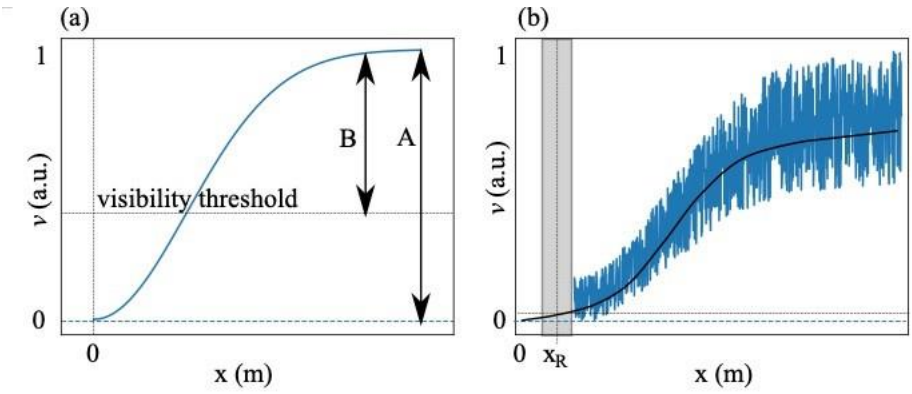

Fig. 3.4 (a) Shows the visibility function *v* for fitting with a visibility threshold due to parameter *B* related to equation (2). (b) shows the visibility function *v* with added noise. Plots (a) and (b) use arbitrary lateral dimensional scale in meters which in practice will be in the millimetre range. The average visibility of a structure must be at least above some noise threshold, which relates to the visibility threshold indicated. The grey shaded range is where the fitted function (black) would predict zero visibility without noise. The zero visibility must occur at lateral position $x_R > 0$. Based on the lateral position x_R, the axial resolution *d* can be calculated using equation (2). The measured visibility in section III-B confirms that the uncertainty impedes the detection of the peaks from the wedge reflections and the signal is lost before the lateral position $x = 0$ (Fig. 9).

Table 3.2

We used wedges with different spacer thickness to evaluate the impact of the wedge slope on the gap visibility.

	Visible wedge length *L* (mm)	Spacer *D* (mm)
Wedge 1	71.0 ± 0.2	0.070 ± 0.006
Wedge 2	69.7 ± 0.2	0.123 ± 0.007
Wedge 3	67.4 ± 0.2	0.237 ± 0.005

The dimensions of the wedge were measured using a micrometer screw gauge and calipers. Although air wedge interference can be used to characterize the wedge geometry to nanometre accuracy, the expected uncertainties of the wedge imaging would not benefit from it. Also, the expected fringe separation for the required wedge geometries based on Table 3.2 would be less than 280 microns and difficult to record accurately. The visible wedge length was measured with calipers to an uncertainty of 200 microns. Also, it could be argued that better accuracy could be achieved with a micrometer stage and microscope. The maximum error expected would be 0.7 μm based on the relation $x/d = L/D$ with x for any lateral position, d the wedge spacing at position x, L the visible wedge length, and D the spacer thickness. This 0.7 μm accuracy is far beyond the achievable imaging accuracy due to the additional uncertainties introduced by the image noise.

The noise of the image acquisition makes the largest contribution to the uncertainty, which is described in more detail, exploring the measurement theory. Although additional image averaging can reduce the noise further, it was of interest for this study to include the noise characteristics for comparison. On the other hand, signal or image averaging may otherwise obfuscate artefacts, i.e., automatic adaptive contrast adjustments. The theory is based on the detection of

the peak separation. As shown in figure 3.3, the visibility, *v*, can be defined by using the height of the peak, *p*, vs dip amplitude, *d*. The visibility, *v*, can then be described by the difference between the peak and dip height and plotted for a sequence of peak distances along a wedge position, *x*, including a peak standard deviation, σ (Fig. 3.3) corresponding to a peak width. The visibility, *v*, then follows the equation:

$$v = 1 - e^{-\frac{x^2}{\sigma^2}} \tag{3.1}$$

Equation 1 only considers a noise-less signal, meaning a visibility up to a lateral zero position ($x = 0$) can be found corresponding to the thin end of wedge. However, measurements in Section 3.3.4 show that the visibility is lost before the lateral position of the touching ends of the wedge are reached ($x > 0$). It should be noted that we acknowledge that the image intensities and noise intensities are log scaled and that the linear difference is log scaled. However, as we consider the visibility as the difference between peak intensity of the wedge edges vs the intensity of the dip, the visibility has the relation as described by equation 3.2 and additional log scaling would not essentially improve details of the visibility measurements.

It is apparent from figure 3.3(a) that noise can obfuscate the dip, and the separation of two peaks cannot be determined if noise levels are too large. We can accommodate noise by adding the parameters for amplitude, *A*, and an uncertainty factor, *B*, to (3.1):

$$v = BA - Ae^{-\frac{x^2}{\sigma^2}} \tag{3.2}$$

Equation 3.2 accommodates now the amplitude parameter, *A*, for normalizing visibility values or to fit against measurement data. The uncertainty factor, *B*, allows the shifting of the visibility curve in figure 3.4(b) such that negative visibilities can be computed that represent data that are not measurable due to noise. Please note that the effect of the uncertainty factor, *B*, is not noise and only accounts for the signal cut-off due to noise as shown in figure 3.4.

Uncertainty factor, *B*, forces the visibility amplitude, *A*, to be shifted such that some components have negative values that are not available as a signal. Figure 3.4(b) shows the visibility computed using equation 3.2 and added variations, whereas values for visibility less than zero have been removed. Compared to the measured visibilities as shown in Section 3.3.4, the modelled visibility (Figure 3.4(b)) agrees well with the observed visibility characteristics.

The uncertainties of the visibility and *B* are difficult to measure accurately as they depend on many different factors that are not easy to control. For instance, the more obvious variations in the OCT reference system (Telesto III) are related to adaptive contrast optimization that becomes visible in the jagged uncertainty of the visibility (see figures in Section 3.3.4). For the HR-SDOCT system described in this manuscript, the high NA lens causes the uncertainty of visibility to change strongly over the scan range, which is clearly visible by the arc shaped characteristics in (see Section 3.3.4). However, some upper and lower boundaries can be estimated based on the observed uncertainty and fitting with equation 3.2. Since equation 3.2 describes the ideal visibility without uncertainties from noise sources for $B = 1$, the curve trajectory would reach $x = 0$ and we can determine the theoretical wedge spacing $d = 0$ mm ($d = xL/D$). The lower boundary for the uncertainty factor must have a value $B < 1$. Based on the theory described and figure 3.4, the uncertainties in visibility show a clear cut-off along the lateral wedge position which can be used to estimate a value for *B*. Therefore, the fitting was performed for $B = 0.9$, 0.94, and 0.98. This allows the visibility to be followed close to the lowest uncertainties observed ($B = 0.90$), including fitting to the mean levels ($B = 0.98$). It should be noted that the if *B* is allowed to vary for fitting, the fitting algorithm does not converge or produces spurious visibility values larger than zero for the touching end.

3.3 OCT parameter measurements and Imaging results

3.3.1 Measured system parameters

To characterize the performance of the OCT system few key performance metrics have been optimised such as axial resolution, lateral resolution, signal to noise ratio (SNR), and sensitivity. All the parameters characterization procedure are described in the next sections.

3.3.2 Axial resolution and sensitivity measurements

After power attenuation and spectral filtering, the sample arm power was measured to be 8 mW. Figure 3.5(a) shows the spectrum of the laser source and the red box shows the selected spectral window. The optical components and optical fibre reshape the light source spectrum, and figure 3.5(b) shows the spectrum obtained from the sample mirror reflection. The spectrum ranges from 1100 to 1500 nm, is centred at around 1300 nm, and the full width at half maximum (FWHM) is about 200 nm.

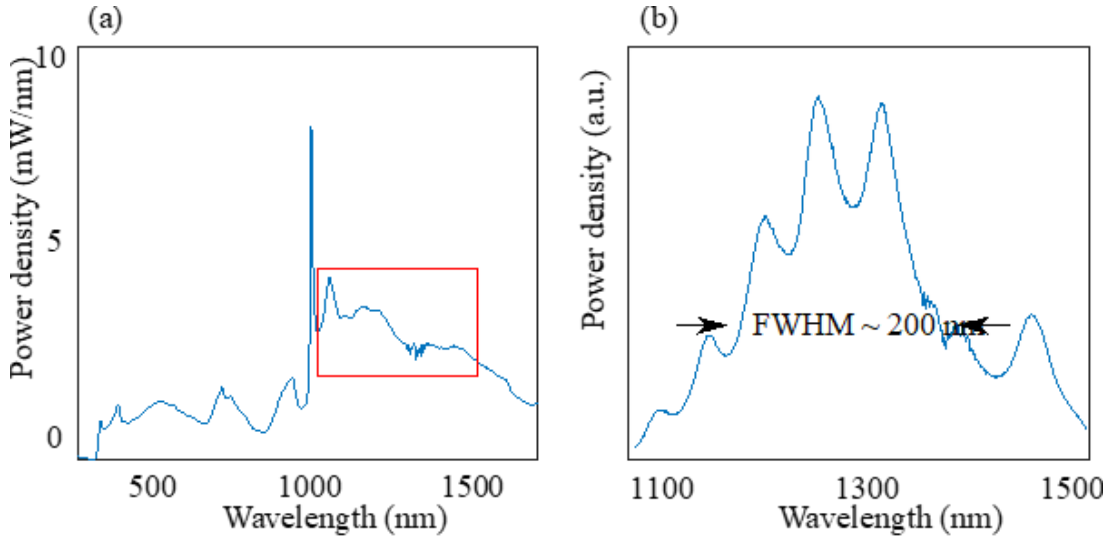

Fig. 3.5 Output spectra of the SuperK EXU6 laser source. The selected spectral window used is from 1100 to 1500 nm (red box). (b) Sample arm spectrum obtained from mirror reflection.

Figure 3.6(a) shows an interference spectrum obtained from the HR-SDOCT system. The axial resolution is defined as the FWHM of the coherence envelope of the interferogram, obtained by inverse Fourier transform. The PSF was measured from a sample mirror reflection at a depth of 100 μm in air and the best fit with a Gaussian provided a value of 3.8 μm as shown in figure 3.6(b). This measured axial PSF on a sample mirror agrees well with the calculated theoretical axial resolution value of 3.7 μm. Figure 3.6(c) shows sensitivity roll-off from 109 to about 94 dB over a depth range of about 1 mm. The roll-off was measured by moving the reference reflactor of the reference arm. The signal-to-noise ratio (SNR) of the system was measured as the difference between maximum peak amplitude and median of the noise floor of the depth profile of the dB scaled values. An SNR of 69 dB was measured using an OD2 optical attenuation (40 dB) in the sample arm with 1024 A-line averaging at the line rate of 73 kHz.

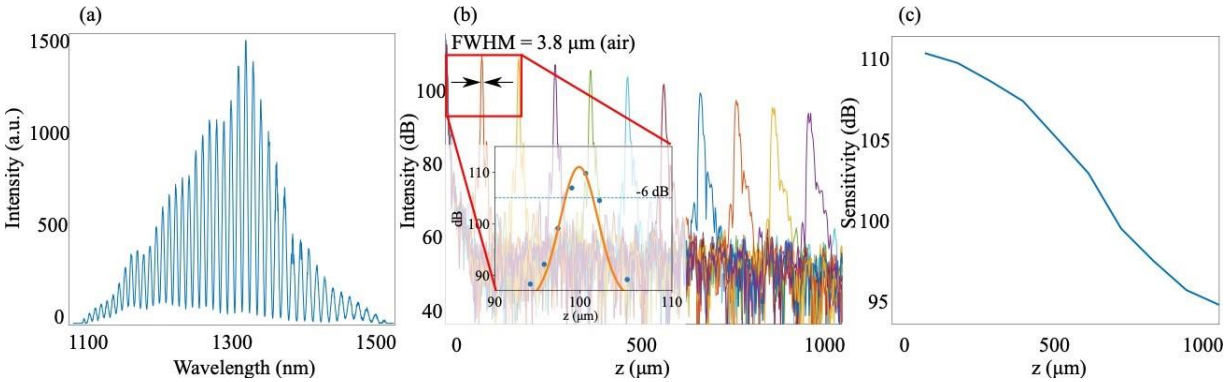

Fig. 3.6 (a) Interference pattern from sample mirror. (b) Measured axial PSF and roll-off over depth (z) and intensity in dB. The inset (red box) shows width of PSF at -6 dB from maximum at 100 μm depth. (c) Roll-off of sensitivity over a range of 1000 micrometre axial depth range.

3.3.3 Numerical simulation (using Zemax) and experimental validation of lateral resolution

The properties of the high-NA lens were simulated with Zemax regarding the lateral PSF in air. Using the paraxial beam approximation and diffraction limited focal spot size at the focal plane, the pupil diameter was varied to find the optimal NA. It was found that an NA of 0.085 for an entrance pupil diameter of 3.4 mm provides a lateral PSF of 6.0 μm. The theoretical lateral resolution of 5.6 μm using $0.37 \cdot \lambda_0/\mathrm{NA}$ agrees well with the simulated value. Figure 3.7(a), (b), and (c) shows that the lateral resolution of about 6 μm remains constant over a scan range of about 2 mm.

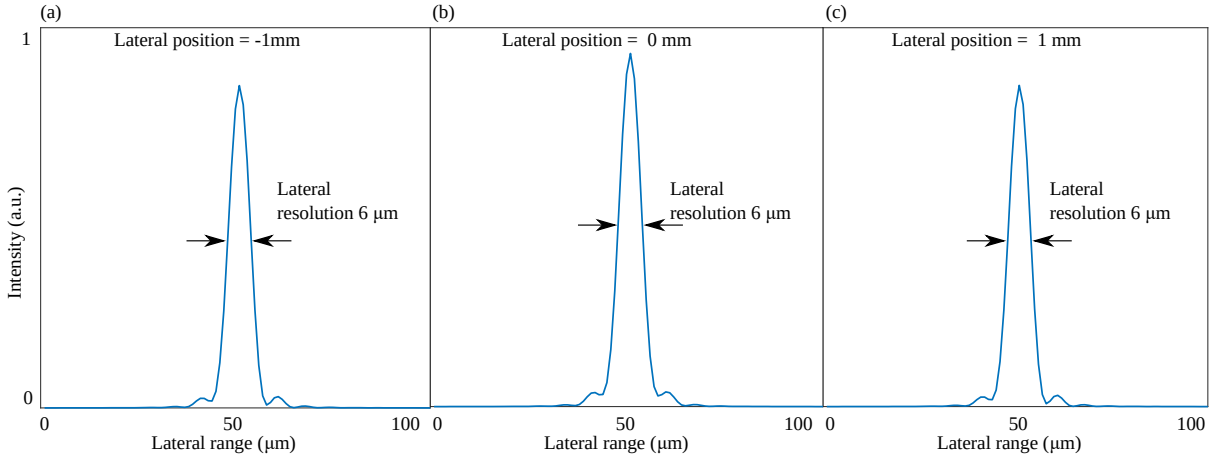

Fig. 3.7 The lateral PSF was simulated, using Zemax, for three lateral positions over a scan range of ±1 mm from the principal axis. The simulation results show that the lateral PSF remains constant over the full scan range.

To verify the lateral resolution, an element group of an USAF test target was scanned with a focused beam and imaged. The en face image in figure 3.8(a) shows the 4th element of group 6, with line spacings of 11 microns. The width of a single element of 5.5 microns agrees well with the simulated lateral PSF in figure 3.8.

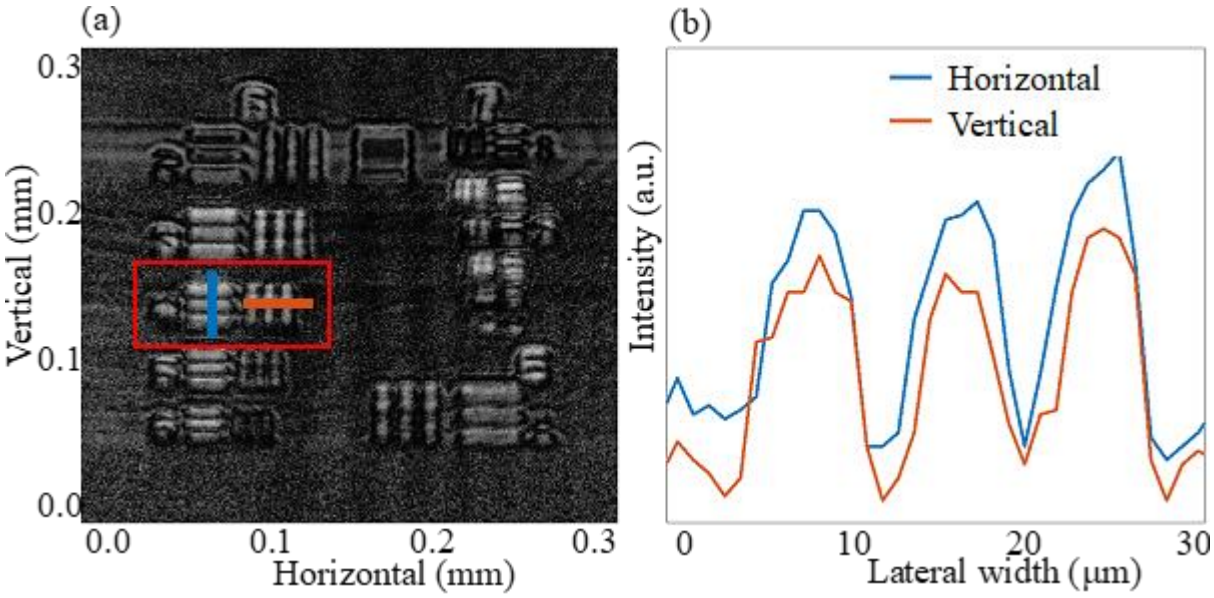

Fig. 3.8 Lateral resolution validation using USAF test target. (a) Zoomed in view of group 6 and 7 elements from Thorlabs (USAF1951). The last resolved line group is 6-4, highlighted in red colour box. (b) The line profile extracted from B-scan image across the vertical and horizontal direction of group 6-4.

3.3.4 Air wedge measurement methods and results

Three different air-wedges were constructed (Fig. 3.9) from commercial microscope slides (VWR International, Cat. No. 631-0109) with dimensions of (75×26×1) mm and spacer material of commercially available aluminium tape (Radionics, 3 M T117).

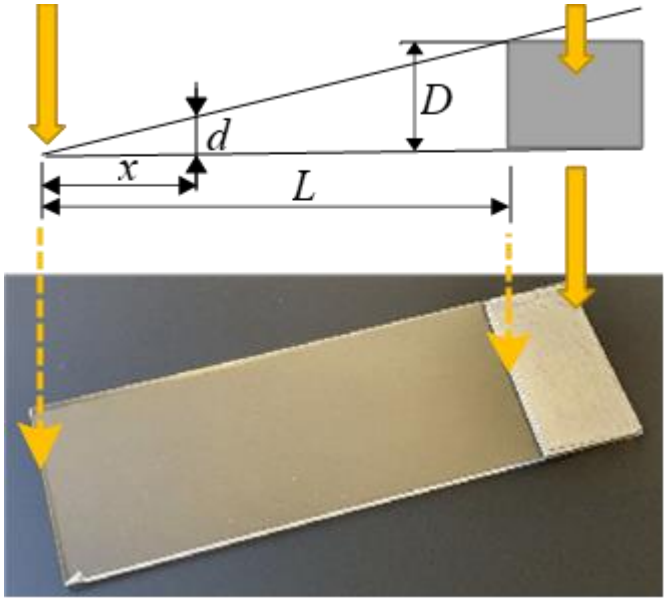

Fig. 3.9 The air-wedge geometry (top) related to the physical constructed wedge made of microscope slides (bottom). The geometry of the air-wedge is described by the visible length, *L*, the wedge spacer thickness, *D*, the lateral position, *x*, and the wedge gap, *d*, at this lateral position. The wedge gap, *d*, is assumed to be zero at the touching end. The average measured dimensions of the microscope slides are *L* = (71.0,69.7,67.4) mm, *D* = (0.070,0.123,0.237) mm (see Table II). The value *x* is measured by fitting in Fig. 9 and *d* is calculated with *d/x* = *D/L*.

Three spacer thicknesses were used (Table 3.2) to estimate the effect of noise, but also to obtain an estimate of measurement variance. The measurement uncertainties for the visible wedge lengths were chosen from the overall largest measured standard variation, assuming that smaller uncertainty values are coincidental. For the spacer thickness, the uncertainties are based on the standard deviation from at least six different measurements with the micrometer screw gauge.

The tape layers were applied on top of the carrier microscope slide and the total thickness was measured with a micrometer screw gauge (reading accuracy of 0.01

mm). Six or more readings were performed over multiple locations over the tape layers and reading values between the ticks were added as estimates for the calculation of the standard deviation. It was found that the total thickness was constant, or any variations were beyond measurable. It should be noted that the total thickness of the tape layers is somewhat less compared to the suppliers' specifications due to the glue layer viscosity. The visible wedge length was then measured using a caliper.

To measure the visibility of the edges of the air-wedge, multiple image segments needed to be acquired over the visible wedge length. The described high-resolution OCT system is limited to a maximum scan range of 2.2 mm. Consequently, to cover a full wedge length, multiple image segments were acquired. The image segments were stored in separate image files and then processed and plotted (Fig. 3.10). For image processing, we used edge detection from scikit-image [47] and the LMFIT [48] package for curve fitting. The edge detection was used to allocate the wedge edges in the images corresponding to the peaks per A-line. Based on the edge location data, the segments were laterally aligned, and the peak and dip heights were measured in the original image. The difference of the peak and median dip height was collected to create the plots in figure 3.10.

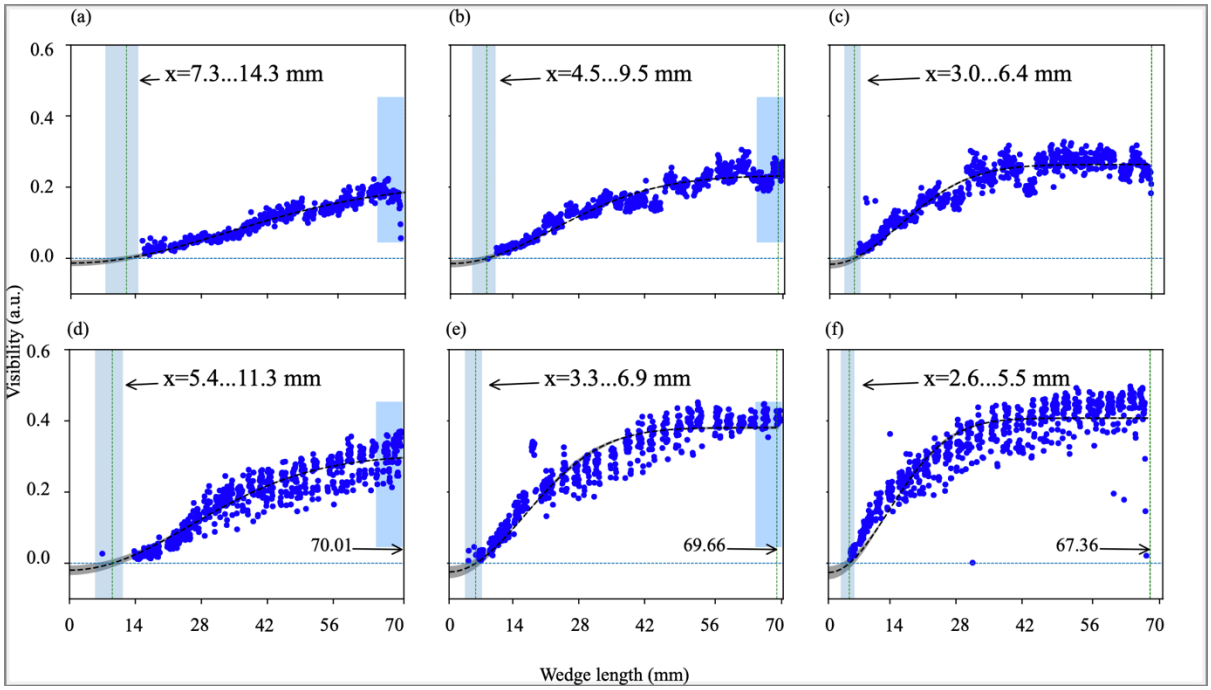

Fig. 3.10 Visibility measurements of Telesto III (a, b, c) and the high-resolution fibre optical OCT system (d, e, f). The fitting variance for the lateral position where visibility of the air gap is lost (for the factor B = 0.90 ...0.98) is shown as grey shade and the black dash line is B = 0.94. The grey regions are the lateral wedge positions where potentially the wedge may still be visible. The edge detection does not detect peaks for the full visibility range, and the uncertainty of visibility increases. Nevertheless, wedge separation may still be detectable within this region and the fitting provides a valid extension of the missing data points. The jagged visibility characteristic for the Telesto III system originates most likely from automatic contrast optimization. The visibility plots were assembled from multiple small segments using a scan range of 2.2 mm to cover the full wedge length. The arc shaped segments for the described high-resolution OCT system originate from the high NA lens.

The wedge imaging was performed to characterize the high-resolution system and compared to the images from a Telesto III (Thorlabs, Inc.) with a centre wavelength of 1300 nm, bandwidth larger than 170 nm, and 5.5 µm axial

resolution in air. Figure 3.10(a–c) shows the results for the Telesto III, figure 10(d–f) shows results for the described HR-SDOCT system. Each column in figure 3.10 corresponds to a different wedge spacer thickness, as tabulated in Table 3.2.

The results in figure 3.10 show how the visibility (blue) can be approximated using a model fit to find the actual smallest wedge space detectable. The model fit accounts for noise or the uncertainty of visibility using an uncertainty factor that is visible as the grey shaded range around the fitted curve. The uncertainty of visibility translates to an uncertainty laterally where the smallest wedge spacing can be predicted, shown as a vertical region in grey. The *x* values in the plot give the numeric range of the predicted lateral positions. Using the values for the wedge spacer given in Table 3.2, the wedge spacing can be calculated using the simple relation $d/x = D/L$ as describe above. The value ranges for *d* are plotted in figure 3.11 showing the best estimates for the detection of wedge gaps.

3.3.5 Air wedge spacing comparison between Telesto III and high-resolution system

It should be noted that ideally, the values for different wedge sizes should produce the same detectable wedge gap. However, it is to be expected that the noise for larger wedge slopes increases more rapidly if the wedge edges converge, which could be attributed to interference effects. Like the air-wedge interference visible with a sodium lamp, interference will occur in the OCT images as well [49]. We did not provide any images of such wedge interference as it was not very pronounced or visible as expected for light sources with a broader spectrum.

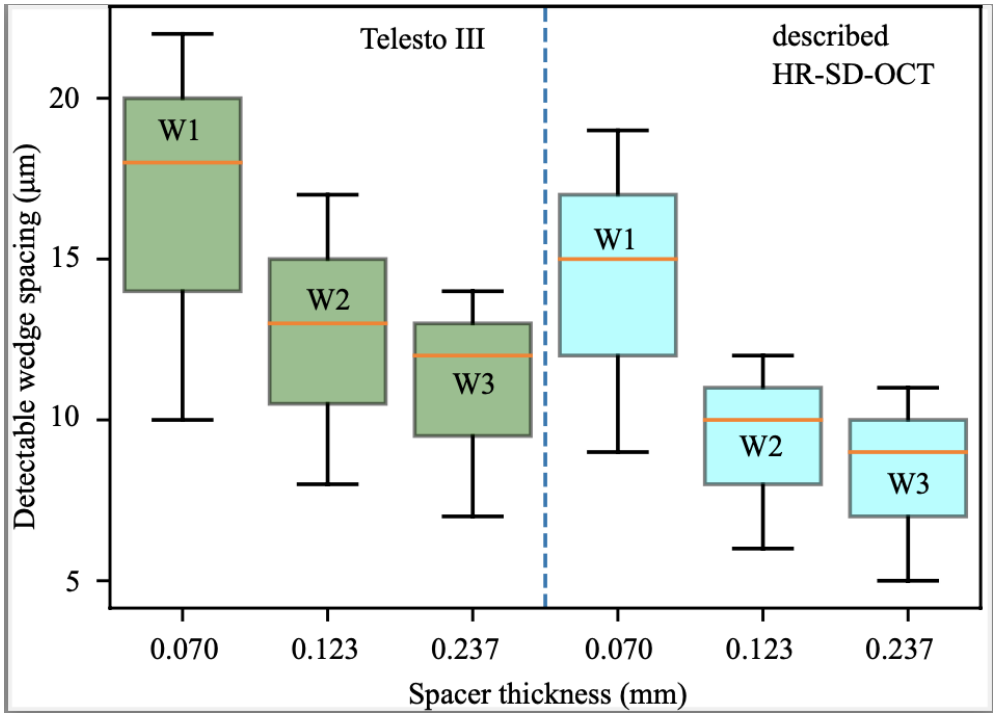

Fig. 3.11 Best detectable wedge spacings compared between Telesto III and the high-resolution system described. The mean difference between both systems is 2.8 microns, and the predicted improvement based on the light source bandwidth is 1.7 microns. Although the values fall within the uncertainties, the consistent difference for three different wedges provides some confidence in an actual resolution difference. The box plot centre values represent the median, the upper and lower box boundaries represent the first and third quartile. The whiskers extend 1.5 times from the upper and lower box boundaries representing the interquartile range giving some estimate of the distribution of data points.

The investigation using simple microscope slides was motivated to understand the limitations of using a low-cost in-house construction method. The results show that the high reflectivity due to the air-glass interfaces causes camera saturation, and additional attenuation increases noise and reduces the visibility of smaller wedge spacings. A follow-up study could use commercial anti-reflective

coated materials to investigate material properties most suitable for higher accuracy wedges. The touching end of the microscope slides is considered the ground truth of a zero spacing that can never be imaged in practice. Only fitting a visibility model over measured wedge data allows estimating the lateral position x_R where the noiseless wedge visibility is lost. The calculation of the wedge spacing d at x_R is obtained from the relation $d/x_R = D/L$. Notably, any uncertainties and systematic errors of measuring D and L will cause increased uncertainty in the value d or even cause an offset deviating from the expected theoretical point-spread function. The uncertainties in x_R originate from the wedge visibility and fitting accuracy. The measured best resolution using the wedge in figure 3.11 is indeed much larger with around 8 microns compared to the expected axial resolution of 3.8 microns measured on a single A-line profile (Fig. 3.6). Other problems with the air wedge are the increasing axial interference of reflections between the layers at very narrow wedge spacing. If the wedge spacing is close to the wavelength of the light source, fringe artefacts increasingly obfuscate the wedge visibility and inhibit the accurate measurement of the axial resolution. Although we could not reliably replicate axial air wedge interference, which appears attenuated due to the broad bandwidth of the light source, it shows that the air wedge is valuable in investigating structural visibility. The air wedge using non-ideal reflecting materials would provide a controlled structure to evaluate different conditions that reduce resolution and visibility in actual samples.

Although, the air-wedge measurement method is limited due to the intensity noise in the image, it is sufficient to obtain a value for the improvement of resolution by direct measurement. However, it also shows that it can provide a rich set of additional information about the visibility an OCT system can provide. Relating to figure 3.9 for instance, the uncertainty of the visibility due to noise is a major indicator of sensitivity performance. The visibility uncertainties for the Telesto III system are narrower overall compared to the described HR-SDOCT system but has a more consistent spread per segment, indicating that some contrast

stretching is performed to obtain optimal image results. In comparison, the described HR-SDOCT system has a large spread due to the high NA lens, but a very narrow spread per segment, indicating that best sensitivity is obtained at the scan centre.

3.3.6 Structural visibility comparison with existing Telesto III and developed high-resolution system

3.3.6.1 Non-biological sample images

To demonstrate the imaging performance of the designed HR- SDOCT system and compare it to the Telesto III system from Thorlabs, we imaged non-biological and biological samples. Figure 3.12 shows B-scan images of multilayer Scotch tape using a similar high-NA sample lens in both systems. Although, in both cases, the depth visibility is limited, the speckle noise for the de- scribed HR-SDOCT system is somewhat better. The isometry of the image voxel improves the structural visibility for our HR-SDOCT system compared to the Telesto system.

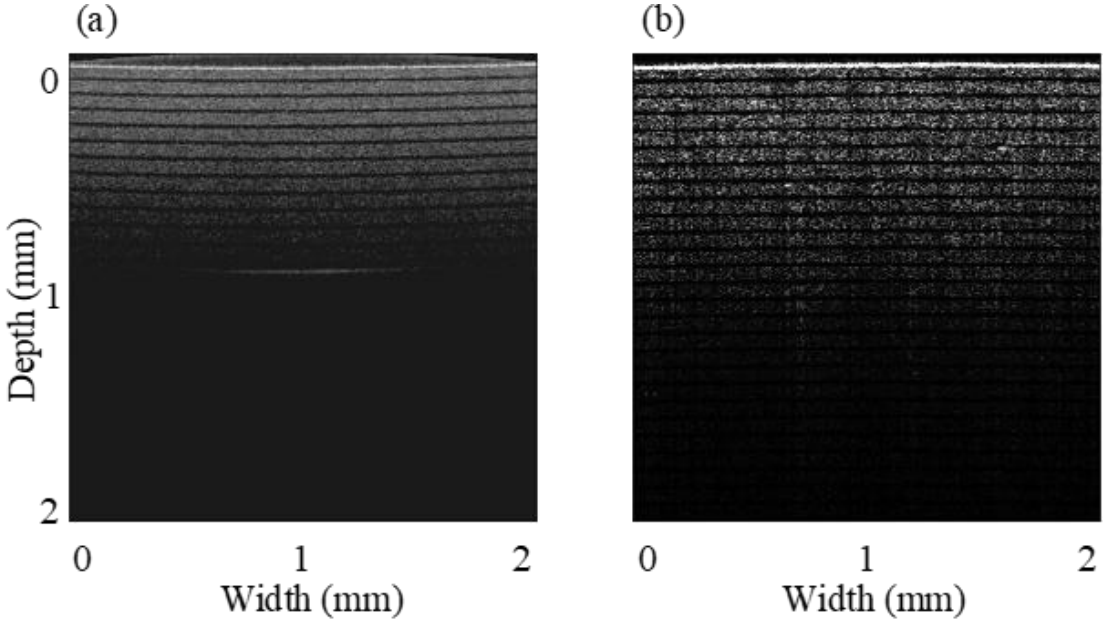

Fig. 3.12 Comparison of the HR-SDOCT (a) vs. the Telesto III (b) using Scotch tape. Image (a) shows smoother speckle structure due to the isometric voxel size.

3.3.6.2 Biological sample images

Figure 3.13(a) and (b) shows B-scan images obtained from volunteer's fingertip. In figure 3.13(a) and (b) the zoomed regions (red boxes) show that for the HR-SDOCT the speckle washout is reduced, whereas for the Telesto system the contrast is improved.

Figure 3.13(c) to (f) show images from a green cucumber compared between the described HR-SDOCT and the Telesto III system. Figure 3.13(c) and (d) confirm that the speckle structures improve due to the isometric voxel shape and consequently reveal more structural details. This would confirm the advantages of isometric imaging to produce a better contrast and improved structural visibility. Figure 3.13(e) and (f) show en face images from the HR-SDOCT and Telesto III respectively.

It should be noted that the HR-SDOCT sacrifices depth visibility due to the high NA sample lens. The lens has the most substantial contribution to reduced depth visibility. Another factor could be the usable spectral resolution of the spectrometer due to a limited spectral illumination. The maximum imaging depth z_{max} for a spectral-domain OCT is described by $z_{max} = \lambda^2_c / 4n\delta\lambda$ where λc is the centre wavelength, n is the refractive index, and $\delta\lambda$ is the wavelength resolution of the spectrometer [50]. Although our system tries to accommodate a maximal bandwidth, not all camera pixels receive equal intensity. Therefore, the maximum spectrometer resolution achievable is reduced, which in retrospect limits the depth visibility.

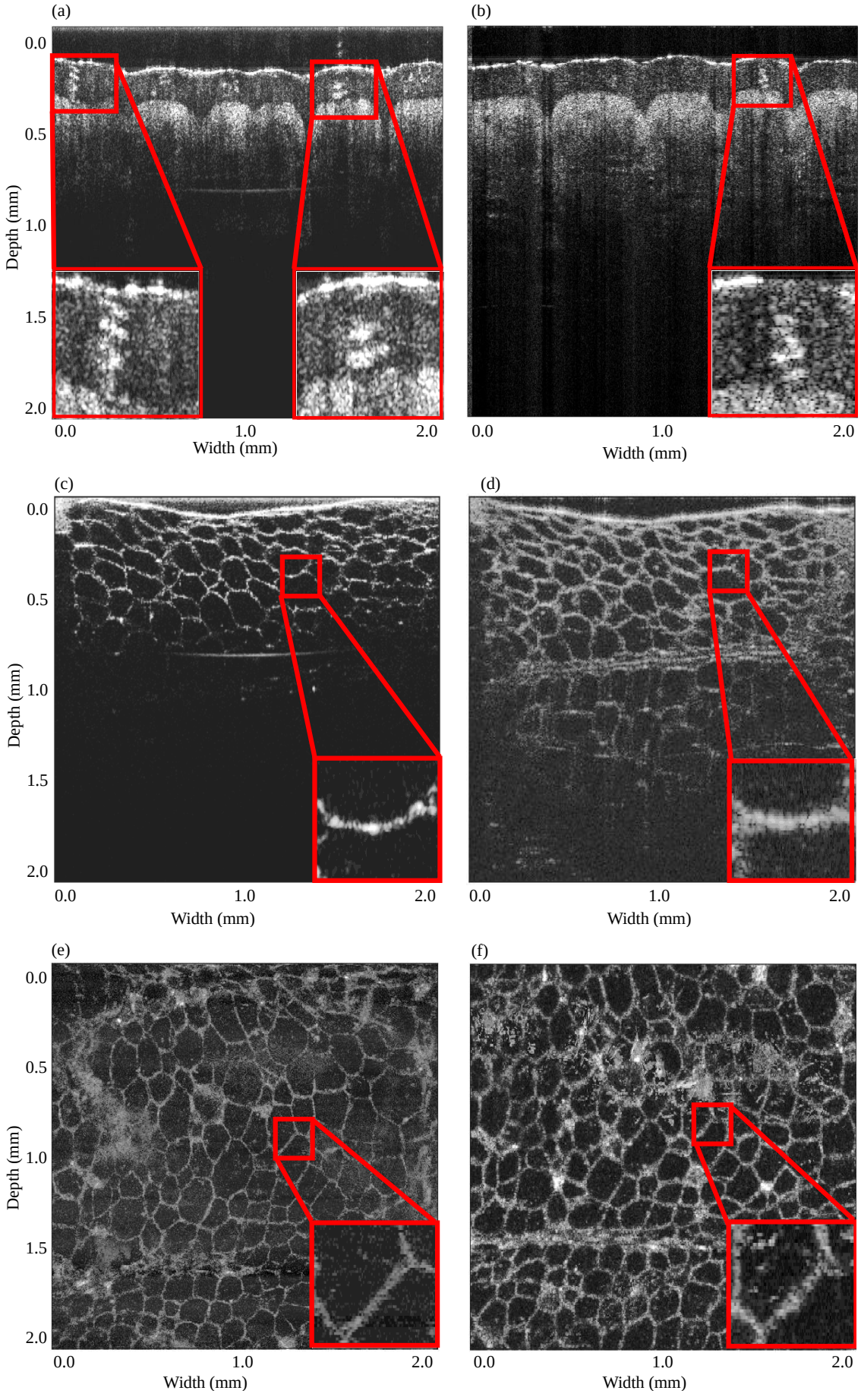
(a)
(b)
(c)
(d)
(e)
(f)
Depth (mm)
0.0
0.5
1.0
1.5
2.0
Width (mm)
0.0
1.0
2.0

Fig. 3.13 Comparison of the HR-SDOCT (left column) vs Telesto III (right column). Images (a) and (b) show a fingertip and the zoomed regions (red box) show a less pronounced speckle washout for the HR-SDOCT system, which may be attributed to the improved isometric voxel shape using the high-NA sample lens. B-frame images of green cucumber (c) and (d). Red boxes from the same selected region show that again the speckle washout for the HR-SDOCT system is less pronounced. En face images of green cucumber (e) and (f). The red boxes from the same selected region show a sharper image, which is to be expected due to the higher NA lens used for the HR-SDOCT vs the Telesto III.

3.3.6.3 Contrast to Noise Ratio (CNR) comparison between Telesto III and developed high-resolution OCT system images

According to literature, the local contrast, in conjunction with the spatial frequency of structures, is relevant in determining the ability of an imaging system to capture or reconstruct features of interest [51]. The contrast-to-noise ratio (CNR) is then the ratio of the local contrast to the image noise. Various other literature sources describe the selection of specific regions to obtain a noise level, and it is usually acknowledged that the CNR is not an absolute metric but a relative metric to compare the local contrast of imaging systems. Conventionally, the root-mean-square or the standard deviation of the noise is obtained from a common image region. However, for the images available for this study and the purpose of comparing between the commercial system (Telesto III) and the investigated fibre-based OCT system, we obtain the noise from the median level in the region of interest. Equation 3.3 describes the mathematical relation to compute the CNR based on the region of interest in the image (I_{ROI}):

$$\mathrm{CNR} = (\max(I_{ROI}) - \min(I_{ROI})) / \mathrm{median}(I_{ROI}) \quad (3.3)$$

The median value is dominated by the noise level, while larger intensity values from structures have little effect. Consequently, we can use the calculated CNR to compare how much local contrast for selected structures in the region of interest is available, as long as the structures are similar in both images and do not fill the whole region of interest (see Fig. 3.13).

Table 3.3 confirms that the investigated high-resolution system has larger CNR values compared to the Telesto system.

Minor differences in the images are expected as it was not possible to equip both systems with the same lens type. Nevertheless, Table 3.3 shows a notable increase of CNR values consistently for three different structures for the investigated HR-SDOCT system.

Table 3.3

CNR compared between Telesto and high-resolution system.

	Telesto	High-resolution system
Finger tip	0.44	2.44
Cucumber B-frame	1.28	9.00
Cucumber en face	0.69	3.27

3.4 Conclusion

This chapter described design of a fibre-based HR-SDOCT system and evaluated a simple air-wedge method to compare axial resolution directly. This chapter also discussed low-cost construction of the air-wedges, which should be easily accessible for many laboratories. Nevertheless, the air-wedge also provides some information about the uncertainty of reproducing a PSF, which may be of interest for high-end image quality quantification.

This chapter presented the feasibility of using a broad bandwidth fibre-based OCT system in conjunction with a high-NA sample lens to improve the isometric shape of the image voxels. Especially in conjunction with the broad bandwidth light source, it shows strong indicators for improved structural visibility in B-frame and en face images. After quantitative CNR comparison, it was confirmed that the high-resolution system improved the structural visibility.

We optimized several OCT key parameters such as axial resolution, lateral resolution and sensitivity. The axial resolution of the HR-SDOCT was calculated to be 3.7 microns based on the spectral bandwidth at FWHM and was measured with a Gaussian fit on the data recorded from the sample mirror to be 3.8 microns. The measured sensitivity roll-off from 109 dB to about 94 dB over a depth range of about 1 mm. The lateral resolution for a scan range of 2 mm is 6 microns from simulation, and the image of the USAF target showed full separation of elements with a spacing of 11 microns. We compared the axial resolution with a Telesto III system that is specified with 5.5 microns in air.

This chapter also presented the axial resolution comparison between HR-SDOCT and a commercial Telesto III system by air-wedge measurements. The HR-SDOCT has about 1.4 times better axial resolution. The air-wedge analysis provided a mean axial resolution of 13 microns for the Telesto and 11 microns for the HR-SDOCT, which translates to about 1.2 times better axial resolution. The larger measured values using the air-wedge are plausible, as the light must

pass through the glass body from the top. This would also allow future research of how the refractive index affects the axial resolution.

The improved image quality in conjunction with isometric image voxel geometry was of major interest for conventional OCT imaging [52-57]. Newly developed nanosensitive OCT (nsOCT) can benefit from the extended spectral bandwidth which permits access to a wider distribution of spatial frequencies and can improve the dynamic range of the length scale sensitivity. Using the nsOCT technique we have characterized *ex vivo* normal and cancerous skin tissue with the intervening marginal area, which is presented in the next chapter.

References

1. D. Huang et al., "Optical coherence tomography," *Science* **254**(5035), 1178–1181 (1991).
2. J. Schmitt, "Optical coherence tomography (OCT): A review," *IEEE J. Sel. Topics Quantum Electron.* **5**(4), 1205–1215 (1999).
3. A. C. Akcay, K. S. Lee, L. R. Furenlid, M. A. Costa, and J. P. Rolland, "Compact low-cost detection electronics for optical coherence imaging," *Opt. Eng.* **45**(7), 070504 (2006).
4. M. Mujat et al., "Retinal nerve fibre layer thickness map determined from optical coherence tomography images," *Opt. Express* **13**(23), 9480–9491 (2005).
5. B. E. Bouma and G. J. Tearney, "Clinical imaging with optical coherence tomography," *Academic Radiol.* **9**(8) 942–953, (2002).
6. X. Yao, Y. Gan, C. C. Marboe, and C. P. Hendon, "Myocardial imaging using ultrahigh-resolution spectral domain optical coherence tomography," *J. Biomed. Opt.* **21**(6), 061006 (2016).

7. J. G. Fujimoto, S. A. Boppart, G. J. Tearney, B. E. Bouma, C. Pitris, and M. E. Brezinski, “High resolution *in vivo* intra-arterial imaging with optical coherence tomography,” *Heart* **82**(2), 128–133 (1999).
8. G. J. Tearney et al., “Quantification of macrophage content in atherosclerotic plaques by optical coherence tomography,” *Circulation* **107**(1), 113–119 (2003).
9. S. A. Boppart, W. Luo, D. L. Marks, and K. W. Singletary, “Optical coherence tomography: Feasibility for basic research and image-guided surgery of breast cancer,” *Breast Cancer Res. Treat.* **84**(2), 85–97 (2004).
10. A. F. Zuluaga, M. Follen, I. Boiko, A. Malpica, and R. Richards-Kortum, “Optical coherence tomography: A pilot study of a new imaging technique for noninvasive examination of cervical tissue,” *Amer. J. Obstet. Gynecol.* **193**(1), 83–88 (2005).
11. B. W. Colston, M. J. Everett, L. B. D. Silva, L. L. Otis, P. Stroeve, and H. Nathel, “Imaging of hard- and soft-tissue structure in the oral cavity by optical coherence tomography,” *Appl. Opt.* **37**(16), 3582–3585 (1998).
12. L. L. Otis, B. W. Colston, M. J. Everett, and H. Nathel, “Dental optical coherence tomography: A comparison of two in vitro systems,” *Dento Maxillo Facial Radiol.* **29**(2), 85–89 (2000).
13. A. Z. Freitas, D. M. Zezell, N. D. Vieira, A. C. Ribeiro, and A. S. L. Gomes, “Imaging carious human dental tissue with optical coherence tomography,” *J. Appl. Phys.* **99**(2), 024906 (2006).
14. J. Olsen, J. Holmes, and G. B. E. Jemec, “Advances in optical coherence tomography in dermatology—A review,” *J. Biomed. Opt.* **23**(4), 040901 (2018).
15. N. M. Israelsen et al., “The value of ultrahigh resolution OCT in dermatology–delineating the dermo-epidermal junction, capillaries in the dermal papillae and vellus hairs,” *Biomed. Opt. Express* **9**(5), 2240–2265 (2018).

16. R. Steiner, K. Kunzi-Rapp, and K. Scharffetter-Kochanek, “Optical coherence tomography: Clinical applications in dermatology,” *Med. Laser Appl.* **18**(3), 249–259 (2003).
17. A. M. Zysk, F. T. Nguyen, A. L. Oldenburg, S. A. Boppart, and D. L. Marks, “Optical coherence tomography: A review of clinical development from bench to bedside,” *J. Biomed. Opt.* **12**(5), 051403 (2007).
18. M. F. Shirazi, M. Jeon, and J. Kim, “Structural analysis of polymer composites using spectral domain optical coherence tomography,” *Sensors* **17**(5), 1155–1166 (2017).
19. P. Meemon et al., “Optical coherence tomography enabling non-destructive metrology of layered polymeric GRIN material,” *Sci. Rep.* **3(**1), 1709–1719 (2013).
20. K.M. Kennedy, S. Es’haghian, L. Chin, R. A.McLaughlin, D. D. Sampson, and B. F. Kennedy, “Optical palpation: Optical coherence tomographybased tactile imaging using a compliant sensor,” *Opt. Lett.* **39**(10), 3014–3017 (2014).
21. D. Culemann, A. Knuettel, and E. Voges, “Integrated optical sensor in glass for optical coherence tomography (OCT),” *IEEE J. Sel. Topics Quantum Electron.* **6**(5), 730–734 (2000).
22. J. F. de Boer, B. Cense, B. H. Park, M. C. Pierce, G. J. Tearney, and B. E. Bouma, “Improved signal-to-noise ratio in spectral-domain compared with time-domain optical coherence tomography,” *Opt. Lett.* **28**(21), 2067–2069 (2003).
23. M. Wojtkowski, T. Bajraszewski, P. Targowski, and A. Kowalczyk, “Realtime *in vivo* imaging by high-speed spectral optical coherence tomography,” *Opt. Lett.* **28**(19), 1745–1747 (2003).
24. R. Leitgeb, C. K. Hitzenberger, and A. F. Fercher, “Performance of Fourier domain vs. time domain optical coherence tomography,” *Opt. Express* **11**(8), 889–894 (2003).

25. M. Choma, M. Sarunic, C. Yang, and J. Izatt, “Sensitivity advantage of swept source and Fourier domain optical coherence tomography,” *Opt. Express* **11**(18), 2183–2189 (2003).
26. M. Wojtkowski, V. J. Srinivasan, T. H. Ko, J. G. Fujimoto, A. Kowalczyk, and J. S. Duker, “Ultrahigh-resolution, high-speed, Fourier domain optical coherence tomography and methods for dispersion compensation,” *Opt. Express* **12**(11), 2404–2422 (2004).
27. G. Humbert et al., “Supercontinuum generation system for optical coherence tomography based on tapered photonic crystal fibre,” *Opt. Express* **14**(4), 1596–1603 (2006).
28. M. Szkulmowski et al., “Quality improvement for high resolution *in vivo* images by spectral domain optical coherence tomography with supercontinuum source,” *Opt. Commun.* **246**(4), 569–578 (2005).
29. P. Cimalla, J.Walther, M. Mehner, M. Cuevas, and E. Koch, “Simultaneous dual-band optical coherence tomography in the spectral domain for high resolution *in vivo* imaging,” *Opt. Express* **17**(22), 19486–19500 (2009).
30. J. Barrick, A. Doblas, M. R. Gardner, P. R. Sears, L. E. Ostrowski, and A. L. Oldenburg, “High-speed and high-sensitivity parallel spectral domain optical coherence tomography using a supercontinuum light source,” *Opt. Lett.* **41**(24), 5620–5623 (2016).
31. Y. J. You, C. Wang, Y. L. Lin, A. Zaytsev, P. Xue, and C. L. Pan, “Ultrahigh-resolution optical coherence tomography at 1.3 μm central wavelength by using a supercontinuum source pumped by noise-like pulses,” *Laser Phys. Lett.* **13**(2), 025101 (2015).
32. C. Chen, W. Shi, R. Reyes, and V. X. D. Yang, “Buffer-averaging supercontinuum source based spectral domain optical coherence tomography for high-speed imaging,” *Biomed. Opt. Express* **9**(12), 6529–6544 (2018).

33. M. Maria et al., “A comparative study of noise in supercontinuum light sources for ultra-high resolution optical coherence tomography,” *Proc. SPIE*, **10056**, 115-120 (2017).
34. K. C. Zhou, R. Qian, S. Degan, S. Farsiu, and J. A. Izatt, “Optical coherence refraction tomography,” *Nat. Photon.* **13**(11), 794–802 (2019).
35. K. C. Zhou, R. Qian, S. Farsiu, and J. A. Izatt, “Spectroscopic optical coherence refraction tomography,” *Opt. Lett.* **45**(7), 2091–2094 (2020).
36. C.-K. Chang et al., “Segmentation of nucleus and cytoplasm of a single cell in three-dimensional tomogram using optical coherence tomography,” *J. Biomed. Opt.* **22**(3), 036003 (2017).
37. K. Q. Kieu, N. N. Peyghambarian, J. Klein, J. K. Barton, and A. Evans, “Ultrahigh resolution all-reflective optical coherence tomography system with a compact fibre-based supercontinuum source,” *J. Biomed. Opt.*, **16**(10), 106004 (2011).
38. S. Ishida and N. Nishizawa, “Quantitative comparison of contrast and imaging depth of ultrahigh-resolution optical coherence tomography images in 800 nm wavelength region,” *Biomed. Opt. Expres*s **3**(2), 282–294 (2012).
39. Y. Lu et al., “Non-planar calibration phantoms for optical coherence tomography,” *Proc. SPIE* **0544**, 148–154 (2018).
40. S. Braun, “Windows,” in Encyclopedia of Vibration, S. Braun, Ed. Oxford, U.K. Elsevier, 1587–1595 (2001).
41. J. G. Robertson, “Quantifying resolving power in astronomical spectra,” *Pub. Astronomical Soc. Aust.* **30**(048), (2013).
42. T. Latychevskaia, “Lateral and axial resolution criteria in incoherent and coherent optics and holography, near- and far-field regimes,” *Appl. Opt.* **58**(13), 3597–3603 (2019).
43. S. V. Aert, D. V. Dyck, and A. J. den Dekker, “Resolution of coherent and incoherent imaging systems reconsidered - Classical criteria and a statistical alternative,” *Opt. Express* **14**(9), 3830–3839 (2006).

44. R. S. Kallweit and L. C. Wood, “The limits of resolution of zero phase wavelets,” *Geophysics* **47**(7), 1035–1046 (1982).
45. R. Barakat, “Application of apodization to increase two-point resolution by the Sparrow criterion I. Coherent illumination,” *J. Opt. Soc. Amer.* **52**(3), 276–283 (1962).
46. M. Moskovits, “Criterion for determining resolving power in the optical near field,” *J. Nanophotonics* **11**(4), 046018 (2017).
47. S. Van der Walt et al., “Scikit-image: Image processing in Python,” *PeerJ* **2**, e453 (2014).
48. M. Newville et al., lmfit/lmfit-py: 1.0.3. Zenodo, doi: 10.5281/zenodo.5570790, (2021).
49. X. Liu, S. Chen, D. Cui, X. Yu, and L. Liu, “Spectral estimation optical coherence tomography for axial super-resolution,” *Opt. Express* **23**(20), 26521–26532 (2015).
50. B. Akca et al., “Toward spectral-domain optical coherence tomography on a chip,” *IEEE J. Sel. Topics Quantum Electron.* **18**(3), 1223–1233 (2012).
51. E. Peli, “Contrast in complex images,” *J. Opt. Soc. Amer. A* **7**(10), 2032–2040 (1990).
52. S. A. Alexandrov, H. M. Subhash, A. Zam, and M. Leahy, “Nano-sensitive optical coherence tomography,” *Nanoscale* **6**(7), 3545–3549 (2014).
53. S. Alexandrov et al., “Spatial frequency domain correlation mapping optical coherence tomography for nanoscale structural characterization,” *Appl. Phys. Lett.* **115**(12), 121105 (2019).
54. Y. Zhou, S. Alexandrov, A. Nolan, N. Das, R. Dey, and M. Leahy, “Noninvasive detection of nanoscale structural changes in cornea associated with cross-linking treatment,” *J. Biophotonics* **13**(6), e201960234 (2020).
55. C. Lal, S. Alexandrov, S. Rani, Y. Zhou, T. Ritter, and M. Leahy, “Nanosensitive optical coherence tomography to assess wound healing within the cornea,” *Biomed. Opt. Express* **11**(7), 3407–3422 (2020).

56. N. Das, S. Alexandrov, Y. Zhou, K. E. Gilligan, R. M. Dwyer, and M. Leahy, “Nanoscale structure detection and monitoring of tumour growth with optical coherence tomography,” *Nanoscale Adv.* **2**(7), 2853–2858 (2020).
57. S. Alexandrov et al., “Accessing depth-resolved high spatial frequency content from the optical coherence tomography signal,” *Sci. Rep.* **11**(1), 17123 (2021).

Chapter 4

Skin cancer margin detection using nanosensitive optical coherence tomography and a comparative study with confocal microscopy

4.1 Introduction

One of the unresolved clinical issues in skin cancer surgery is the lack of any objectively reliable label-free and accurate assessment modality for resection margin status pre-operatively or intraoperatively. Most commonly, intraoperative visual inspection and palpation are used. This intraoperative technique results in wider surgical margins in almost 40% of the patients [1-3]. Also, this technique is time-consuming. To overcome these clinical challenges, a highly sensitive, non-invasive, cost-effective, and real-time diagnostic tool is required [4]. The use of optical diagnostic technologies such as confocal [5, 6], Raman [7], and two-photon [8] microscopy in clinical trials has increased in the past few years. However, most of these techniques are limited to imaging depth up to 100-300 micrometres due to issues with multiple scattering, high numerical aperture, and photon absorption. OCT, in contrast, can image up to a depth of 1 to 2 millimetres in biological samples with high voxel resolution. OCT is a non-invasive optical imaging modality based on low coherence interferometry that enables high-resolution cross-sectional imaging in materials and biologic systems by measuring backscattered light [9]. One major advantage of OCT is that it can be used to obtain both structural and functional information from real-time imaging. Huang et al. introduced the principle of OCT in the 1990s [10]. Initially, its clinical use was restricted to the field of ophthalmology [11, 12]. Soon after, OCT clinical application extended to several disease diagnoses such as heart and blood vessels [13, 14], tumours [15, 16] visualization of the dental structure [17, 18], diagnosis and treatment of skin disorders [19-22].

In the last three decades, OCT techniques and tools have improved the resolution to detect micrometre-scale tissue structures. The axial resolution of the conventional OCT system typically depends on the bandwidth and central wavelength of the light source. The lateral resolution depends on the numerical aperture of the sample arm objective lens [23]. Over the years, to improve the axial resolution, supercontinuum laser sources have been used [24]. In general, conventional OCT commonly has non-isometric resolutions, particularly with poorer lateral resolutions on the order of 10 µm or greater. Objective lenses with high numerical aperture are used in conventional OCT systems to achieve near-isometric resolution and detect fine structural features within a limited imaging depth of a volume object [25-27]. Sensitivity and scanning speed are two other major parameters of the OCT system. The scanning speed and sensitivity significantly improved by Fourier domain OCT (FDOCT) including spectral-domain OCT (SDOCT) and swept-source OCT (SSOCT) in comparison with time-domain OCT (TDOCT) [28].

Recently Bernstein *et al.* demonstrated a supercontinuum-based ultrahigh-resolution spectral-domain OCT system with a central wavelength of 1300 nm and axial resolution of 2.6 µm in the air [29]. However, the resolution limits persist, and sub-micron structural features remain inaccessible to OCT. Structures smaller than approximately half of the illumination wavelength were not resolvable. However, structures smaller than the diffraction limit still affect the scattering events. This emerges as granular artifacts in the OCT image known as speckle. The fundamental idea of speckle is that random interference within a resolution voxel occurs, so that a dark pixel in an image does not always represent a weaker scattering structure. Recently, a few OCT methods to detect sub-micrometre structural changes within biological tissue have been described. Inverse spectroscopic OCT (ISOCT) was introduced by measuring the

wavelength-dependent scattering and backscattering coefficient to quantify the mass-density function. They show that the length scale of sensitivity of ISOCT ranges from 30 to 450 nm without resolving specific geometrical features [30, 31]. Another technique is based on the phase-sensitive OCT (PSOCT) to characterize the motion of cellular components within the organ of Corti at a sub-micron scale [32]. Nanosensitive OCT (nsOCT) is a novel imaging technique based on the spectral encoding of spatial frequencies (SESF) principle [33-38]. An advantage of the SESF technique was used for real-time and super-resolution 2D microscopy imaging [34-37]. The axial spatial frequency profiles are reconstructed at each pixel in 2D image. The nsOCT is a realization of the SESF approach for 3D imaging, where the axial spatial frequency profiles are reconstructed from each voxel in 3D OCT image. The nsOCT visualizes sub-wavelength structure without resolving it and provides nanoscale sensitivity to structural changes from single frame [39-46]. Each local frequency component of the scattering object is encoded in a corresponding optical illumination wavelength range. Recently, nsOCT has been applied to detect both structural [42-44] and functional [45] changes in *ex vivo* and *in vivo* biological tissues including visualization of the nanoscale structural changes within mesenchymal stem cells (MSC) [46]. The nsOCT gives the information content of the FDOCT signal which is based on the general scattering theory. In our previous publication [39-44, 46], we showed that the FDOCT signal in the axial component of the 3D Fourier transform of spatial frequencies is limited by illumination bandwidth. We also explained the reason why high spatial frequency information is absent in conventional OCT image. In addition, we demonstrated how this high spatial frequency information can be mapped to each volume of interest within the FDOCT image. Therefore, besides detection of the alteration of the structure smaller than spatial resolution, nsOCT approach permits visualization of the dominant spatial period of the sub-wavelength structure at each small volume of interest within the FDOCT image. Despite some similarities in processing

between spectroscopic OCT (SOCT) [47-49] and nsOCT, the nsOCT technique is fundamentally distinct from SOCT, which is often based on sample absorption properties or on models such as Mie scattering theory to compute the size of spherical scatterers. The interpretation of the nsOCT and SOCT results also differ. To our knowledge, there is no publication where the spectroscopic OCT was used to reconstruct the local Fourier spectra of spatial frequencies within the sample.

In the last decade, OCT in the field of Dermatology was less established than in Ophthalmology since the scattering of light strongly limits the penetration into the skin [50]. Nowadays, OCT has been increasingly used to diagnose, monitor treatment response, and plan excisions of skin cancers and non-cancerous skin diseases [51]. Recently, line-field confocal optical coherence tomography (LCOCT) combined the benefits of high penetration depth of OCT and high-resolution, equivalent to reflectance confocal microscopy to acquire the volume image from the diseased skin [52]. However, this technique cannot give nanometre length scale sensitivity from the tissue structure's volume image. The most prevalent nonmelanoma skin cancer among Caucasians is basal cell carcinoma (BCC) [53]. The second most common form of skin cancer is squamous cell carcinoma (SCC). Both BCC and SCC arise in the basal layer of the epidermis. It is well known that many cancers have their first manifestations at the nanoscale level, and these nanoscale structural changes start at the cellular level before appearing at the tissue level. Non-invasive nsOCT has great potential to detect sub-cellular nanoscale structural features at clinically relevant depths.

In this chapter, we discuss the usefulness of the nsOCT technique, using an SDOCT system with a broadband supercontinuum light source, in three different ways. Firstly, we numerically validate the nsOCT approach on synthetic submicron axial structures made to a few nanometres tolerance. Secondly, we

experimentally validate the nsOCT approach from two periodic Bragg grating samples with known dimensional sizes. We apply the nsOCT method in assessing and discriminating between *ex vivo* healthy skin and cancer margin of the resected surgical specimens. Finally, we compare nsOCT image information with high-resolution confocal microscopy images.

4.2 Detection method and theory of nanosensitive optical coherence tomography (nsOCT)

4.2.1 Theory of nsOCT

In a light scattering problem for determination of the electric field at any point inside the object, we assumed that the light is incident in a homogeneous medium. We can write the incident electric field equation for the infinite plane wave incident on object [54]

$$E_i(r,t) = E_0 \exp\big(i(k.r - \omega t)\big) \tag{4.1}$$

k being the wave number and ω is the frequency of the incident field. Incident and scattered field shown in the figure 4.1.

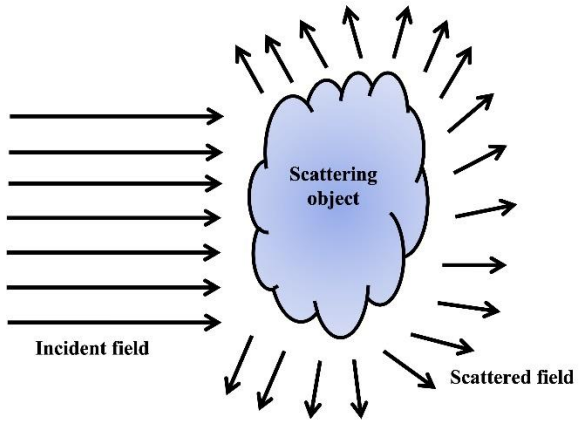

Fig. 4.1 Incident field and scattered field inside the object.

For the electric field the differential equation in the presence of a scattering medium having space varying dielectric 'constant' ε (r) (or corresponding refractive index *n* (r)) can be written as [55]

$$\nabla^2 U(\mathbf{r},\omega) + k^2 n^2(\mathbf{r},\omega) E(\boldsymbol{r},\omega) = 0 \tag{4.2}$$

The above equation generally considers the vectorial electric field. In the scalar approximation, the field $E(\mathbf{r},\omega)$can be replaced by any of its components $U(\mathbf{r},\omega)$. The above equation can then be rewritten as

$$\nabla^2 U(\mathbf{r},\omega) + k^2 U(\mathbf{r},\omega) = -4\pi F(\mathbf{r},\omega) U(\mathbf{r},\omega) \tag{4.3}$$

Here, the right-hand side represents the scattering potential given by

$$F(\mathbf{r},\omega) = \frac{1}{4\pi} k^2 [\, n^2(\mathbf{r},\omega) - 1] \tag{4.4}$$

Field inside scattered medium, $U(\boldsymbol{r},\omega)$ can be expressed as the sum of the incident, $U^i(\boldsymbol{r},\omega)$and the scattered field, $U^s(\boldsymbol{r},\omega)$ as

$$U(\mathbf{r},\omega) \sim U^i(\mathbf{r},\omega) + U^s(\mathbf{r},\omega) \tag{4.5}$$

Considering incident plane wave that satisfies Helmholtz equation, equation 4.3 reduces to

$$(\nabla^2 + k^2) U^s(\mathbf{r},\omega) = -4\pi F(\mathbf{r},\omega) U(\mathbf{r},\omega) \tag{4.6}$$

The total field inside the scattering medium can be obtained by converting $U^s(\boldsymbol{r},\omega)$ to an integral equation by using the Green's function of Helmholtz equation and considering the incident field to be monochromatic plane wave $(U^i(\mathbf{r},\omega) = e^{ik\boldsymbol{s_0}\mathbf{r}})$. The total field can then be written as [55]

$$U(\mathbf{r},\omega) = \mathrm{e}^{ik\boldsymbol{s_o}\mathbf{r}} + \int_V F(\mathbf{r}',\omega) U(\mathbf{r}',\omega) \frac{e^{ik|\mathbf{r}-\mathbf{r}'|}}{|\mathbf{r}-\mathbf{r}'|} d^3\mathrm{r}' \tag{4.7}$$

Here, s_o represents the unit vector of the incident wave.

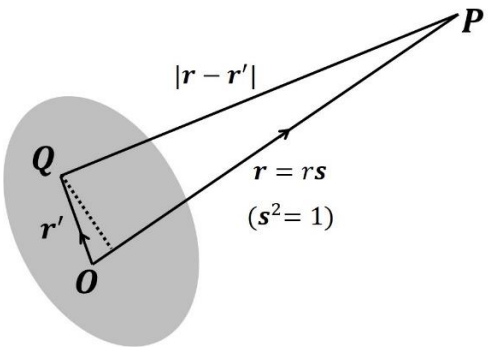

Fig. 4.2 Illustration of far field approximation.

For weakly fluctuating scattering medium, the total field under the integral in equation 4.7 can be replaced by the incident field U^i. Using this approximation, one arrives to a first order approximation of the solution as

$$U(\mathrm{r}) = \boldsymbol{U_1}(\mathrm{r}) = \mathrm{e}^{ik\boldsymbol{s_o}\mathbf{r}} + \int_V F(\mathrm{r}')\,\mathrm{e}^{ik\boldsymbol{s_o}\mathbf{r}}\frac{e^{ik|\mathbf{r}-\mathbf{r}'|}}{|\mathbf{r}-\mathbf{r}'|}d^3\mathrm{r}' \tag{4.8}$$

This above approximate solution is referred to as the 1st order Born approximation or Born approximation. In the far field, the above equation reduces to

$$U_1(r) \sim \mathrm{e}^{ik\boldsymbol{s_o}\boldsymbol{r}} + f_1(s, s_o)\frac{e^{ikr}}{r} \tag{4.9}$$

$$f_1(s, s_o) = \int_V F(r')\,\mathrm{e}^{ik(\boldsymbol{s}-\boldsymbol{s_o})r'}d^3r' \tag{4.10}$$

From the above equation, it is apparent that the expression of the scattering amplitude $f_1(s, s_o)$ is simply the Fourier transformation of the scattering potential given by

$$F(\mathbf{K}) = \int F(r')e^{-i\mathbf{K}.\mathbf{r}'}d^3\mathrm{r}' \tag{4.11}$$

$$f_1(s, s_o) = F[\mathrm{K}(\mathbf{s} - \mathbf{s_o})] \tag{4.12}$$

The above equation implies that under 1st order Born approximation, the scattering amplitude in the far zone in the direction of unit vector $\boldsymbol{s}$, depends only

on the Fourier component of scattering potential. The corresponding scattering vector is defined as [55]

$$\mathbf{K} = k(\mathbf{s} - \mathbf{s_o}) \tag{4.13}$$

K represents the spatial frequency vector. From the Born Approximation it can be observed that in the scattered field have the information about all possible spatial frequencies of the object structure. The consequence of the simple formula (Eq. 4.13) has the solution of the inverse scattering problem, i.e., the problem of obtaining information about the object by measuring the scattered field from it. Wolf first demonstrated the inverse scattering problem in the application of holography to determine the three-dimensional structure of weakly scattering semi-transparent objects [56]. Equation 4.13 can be expanded for the 3D object and the structure is described by spatial frequency vector components, which can be written as in Cartesian coordinates [46]

$$\mathbf{K} = \frac{2\pi n}{\lambda}(\mathbf{s} - \mathbf{s_0}) = 2\pi n[(\upsilon_x \mathbf{i} + \upsilon_y \mathbf{j} + \upsilon_z \mathbf{k}) - (\upsilon_{0x} \mathbf{i} + \upsilon_{0y} \mathbf{j} - \upsilon_{0z} \mathbf{k})] \tag{4.14}$$

where $\boldsymbol{s}$ and $\boldsymbol{s_0}$ are the unit vectors of the scattered and illuminated waves. υ_x, υ_y, and υ_z are the spatial frequencies along the *x*, *y*, and *z* direction of the object structure. Equation 4.11 described the amplitude of the scattering wave, and it shows this wave has an information about all spatial frequencies. This information can be represented visually as several Ewald spheres. For a single wavelength, at constant illumination and collection angle provide information about one frequency component at one point on the Ewald's sphere. In figure 4.3(a) is presented illumination and collection geometry. If the object is illuminated by a plane wave with a broad spectral bandwidth, then the spatial frequencies distribution in **K**-space for all collection angles can be illustrated as multiple Ewald's spheres with different diameters. Figure 4.3 (a) is represented

spatial frequency distribution in 2D plane for the 1100-1500 nm spectral bandwidth.

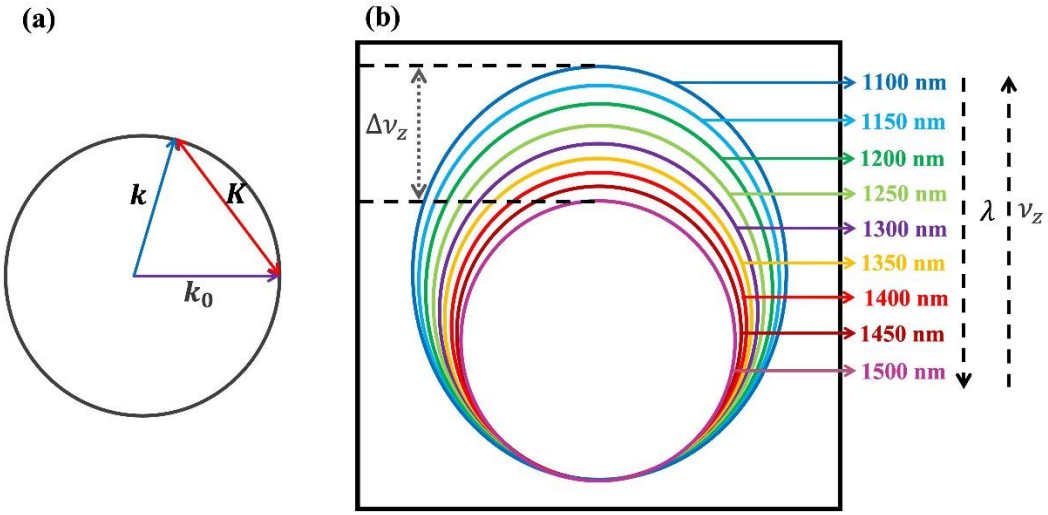

Fig. 4.3 (a) illumination and scattering geometry in **K**-space for a particular one point on Ewald sphere (b) Spatial frequency representation in Ewald sphere at various wavelength.

OCT is a one-dimensional solution of the inverse scattering problem. In OCT, the direction of illumination and measurement of back scattering light are the same as scattering technique. In OCT every time we detect only object depth profile of the scattering potential along one line which is called A-line. Scanning the illumination light on the object surface we construct the volume where have all the spatial frequency information of the object. In OCT signal we capture broadband spatial frequencies information which are labelled by a **K**-vector in equation 4.14 and measure the Fourier components of the spatial frequencies. But the reconstructed OCT image resolution is in micron scale like 5-10 microns. So, during the OCT image construction after inverse Fourier transform we are losing

some high spatial frequency information which corresponds to small structural information of the object. All the high spatial frequency information exists in the OCT signal but does not exist in the constructed OCT image. Fourier shift theorem told that if spectrum will be shifted then the reconstructed profile after absolute value of Fourier transform remaining the same. That's why all information about high spatial frequency disappear. To keep all the spatial frequency information in each voxel of the three-dimensional OCT image, we applied nsOCT technique [46] to detect small structural information and the nsOCT image formation described in the next section.

4.2.2 nsOCT Image formation

Nanosensitive OCT detects the spatial and temporal structural changes within the three-dimensional scattering objects. The nsOCT method is based on the theory of spectral encoding of spatial frequency (SESF) approach, which allows detection of structural changes of the objects with nanoscale sensitivity [33-37]. To construct the nsOCT images, first we processed the interference spectra after basic preliminary signal processing, including background noise removal, apodization, **K**-space linearization, and dispersion compensation. Follows from equation 4.15 the collected axial spatial frequency component in the *z* direction can be expressed [46] as

$$v_z = n(cos\theta + cos\alpha)/\lambda \qquad (4.15)$$

where θ and α are the illumination and scattering angles. n and λ are the refractive index of the medium and illumination wavelength. For the reflection configuration at small illumination and scattering angles θ and α are ≈ 0, which is typical for OCT [46]. Then the processed interference spectra are rescaled from wavelength to frequency. After that, the collected complex amplitudes of the

spectra are converted to complex amplitudes of spatial frequency based on the following relation, which is a simplified form of equation 4.15.

$$v_z = 2n/\lambda \tag{4.16}$$

where n is the refractive index, and λ is the wavelength of the light source. The spatial frequency range is subsequently calculated as

$$\Delta v_z = 2n\Delta\lambda / \lambda_1 \lambda_n \tag{4.17}$$

where $\Delta\lambda = \lambda_n - \lambda_1$ is the light source bandwidth, λ_n and λ_1 are the longest and shortest wavelengths of the light source spectrum.

The rescaled spectra of the complex amplitude of spatial frequencies are decomposed into the sub-bands, for example, using the Tukey window. The IFFT (inverse Fourier transform) of each sub-band signal has been performed to get the amplitude along all the imaging depths for one spatial frequency range. Finally, by combining all the sub-band spatial profiles, it is possible to reconstruct the axial spatial frequency profile at each image pixel/voxel. After that the dominant spatial frequency/period can be calculated from each voxel. The relation between the spatial periods of the structures and the spatial frequencies is as follows

$$H_z = 1/v_z \tag{4.18}$$

From the dominant spatial period of each voxel, an nsOCT image can be formed using an optimized threshold. In the present study, $\Delta\lambda$ is 400 nm where the corresponding λ_1 to λ_n range is 1100 to 1500 nm. According to equation 4.18 physical spatial periods varied from 392.8 nm to 535.7 nm (after correction using n = 1.36 for human skin). From the nsOCT images we measured different

nanometre scale structural [42-44, 46] and functional [45] information using different parameters like dominant spatial period, median spatial period, and correlation between two spatial frequencies. In this chapter we mapped the dominant or physical spatial periods from the nsOCT profile. As an application of the nsOCT technique, we applied this technique on low and highly scattering *ex vivo* biological samples such as bovine cornea and human skin tissue.

4.3 Impact of broad bandwidth light source on nsOCT

According to equation 4.17 we can see spatial frequency range depends on the light source bandwidth. If we increase the bandwidth of the light source, spatial frequency range also increase. As a result, we can detect all the small structures within the detected broader spatial frequency range. So, in the nsOCT image we can increase the dynamic range of the length scale sensitivity. In this study we used 400 nm bandwidth with 1300 nm centred supercontinuum light source. The detected spatial frequency range is from 0.0018 nm^{-1} to 0.0013 nm^{-1}.

4.4 Materials and Methods

4.4.1 High-resolution broadband spectral-domain OCT system

For spectral interference data collection, a custom built fibre-based SDOCT system is used with supercontinuum laser light and a broadband spectrometer. The SDOCT system has an axial and lateral resolution of 3.8 μm in air and 5.5 μm, respectively [57]. This SDOCT system operates within a wavelength range of 1100 nm to 1500 nm with a central wavelength of 1300 nm. The system has a sensitivity of 109 dB at 73 kHz line rate. Detectable spatial period or spatial frequency range depends on the light source bandwidth and spectrometer bandwidth range. The data acquisition process was performed through our home-

built software platform written in LabVIEW. All post-processing steps were done separately in MATLAB after data acquisition to reconstruct conventional B-scan images and nanosensitive OCT (nsOCT) images.

4.4.2 Tissue Sample Preparation

This research study was approved by the Galway Clinical Research Ethics Committee and the approved reference number is *C.A. 2575*. All the fresh tissue samples from human skin are prepared in accordance with the guidelines of the Department of Anatomic Pathology, Galway University Hospital. Tissue samples are examined by a pathologist, who documents any gross abnormalities and applies ink to the margins of the specimen, prior to sectioning the specimen into 2 mm slices to be processed for microtomy and H&E staining to facilitate pathological diagnosis. Concomitantly a representative section of tissue, including tumour and adjacent normal tissue is taken for this research study. All the tissue samples were kept into 4% paraformaldehyde (PFA) solution to keep the samples fresh and to minimize the structural changes. Only during the OCT imaging, all the tissue samples were removed from the PFA solution for a minimum period to avoid dehydration. After finishing the OCT imaging from the same tissue sample, one slice was taken for histology imaging and the rest of the tissue block was embedded in paraffin for high-resolution confocal microscopy imaging with the help of pathologists. During histology and confocal microscopy imaging, tissue samples were kept in the same orientation as the OCT image.

4.4.3 Confocal and light microscopy image analysis flowchart

To analyse the spatial frequency profiles from the confocal and H&E slide images, we analysed two hundreds vertical line profiles across the confocal image in a given region and Fourier transform of these profiles were calculated to obtain the spectrum of spatial period distribution of the structures as shown in flowchart below. The regions within the confocal image were carefully chosen to avoid any artefacts caused by fixation/folding. From the Fourier spectrum of the profiles, median spatial frequencies/periods of the spectrum were calculated using equation 4.19

$$msf = \frac{\sum_{n=1}^{N} f(n)x(n)}{\sum_{n=1}^{N} x(n)} \tag{4.19}$$

where *x(n)* represents the intensity of the spatial frequency/period profile at the frequency/period *f(n)*. This method characterises the median local structure size within the sample.

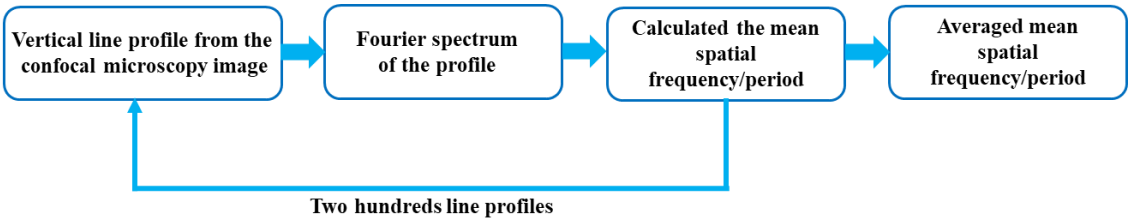

4.5 Results and Discussion

4.5.1 Submicron axial periodic structures and numerical simulation to construct nsOCT image

The nsOCT technique was used to image two samples with sub-micron periodic structure along depth (reflection Bragg gratings) from OptiGrate Corp. USA, as proof of concept. These two samples have different axial periodic structures, and the periodicity is 431.56 nm and 441.76 nm. Each periodic layer was fabricated

using a sinusoidal refractive index variation of 1.483 ± 0.001. The periodicity of the sample remains stable for ambient temperatures up to 400°C. Each sample has a thickness of ~3 mm. To mimic this experimental condition, we synthesized and performed numerical simulation using three different axial periodic structures with periodicities of 431.56 nm, 441.76 nm, and 445.04 nm. In these axial periodic structure simulations, we followed the same sinusoidal refractive index variation as Bragg grating samples. In our previous paper, we showed the simulation of randomized submicron axial structures with different periodicities at different depths to mimic the tissue-like structure [44]. We demonstrated that a few nanometres structural differences can be detected between the randomized axial structures along the depth direction. In our present simulation strategy, we applied this to an OCT system with a broadband supercontinuum laser and followed standard SDOCT image construction theory to implement the proposed nsOCT simulation [55, 56]. To mimic the same fabricated layer sample, in the simulation, we divided each periodic layer into many sublayers with a thickness of 0.01 nm to make it smooth enough for sinusoidal refractive index variation. For example, one sample has 431.56 nm periodicity and the number of sublayers in each periodic layer is 43,156. The SDOCT interference signal was formed from the different layers of the synthesized structure and the reference wave of the gold-coated mirror reflection. In the simulation, we added some background noise from the detector spectra to mimic the same experimental condition. To match the experimental conditions, we used a signal-to-noise ratio of ~ 69 dB in the simulation. Finally, the B-scan image was formed after the inverse Fourier transform of the interference signal. In OCT simulation the same sinusoidal refractive index variation was considered for all three samples with layer thicknesses of 431.56 nm, 441.76 nm, and 445.04 nm. From these simulations, we have demonstrated that our state of art nsOCT method can detect depth-resolved submicron structures with an accuracy of a few nanometres.

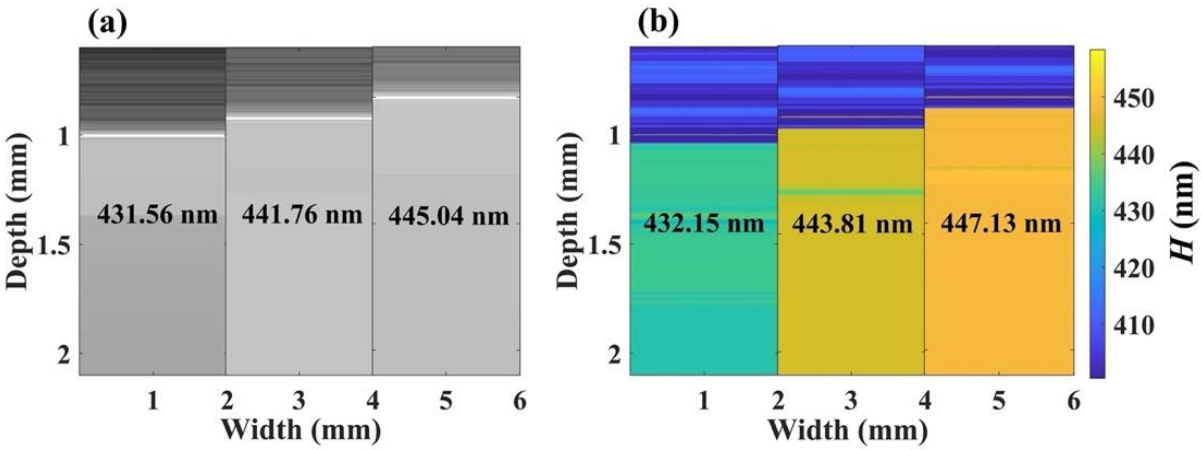

Fig. 4.4 (a) Simulated OCT B-scan images from three different periodic structures and corresponding original spatial periods. (b) nsOCT B-scan images from (a) along with the detected submicron structural sizes.

To validate the nsOCT technique, we constructed intensity-based OCT B-scan images from three different synthetic axial structures. In Figure 4.4(a), we show the OCT B-scans from the synthetic structures along with their axial structural size. Figure 4.4(b) shows numerically constructed dominant spatial periods mapping nsOCT image from the Figure 4.4(a) OCT B-scan image. Detected submicron axial structural sizes are mentioned on each nsOCT image. From this numerical nsOCT technique, it is clearly seen that the submicron axial structure is detectable within the ~2 nm accuracy.

4.5.2 Experimental validation of nsOCT from submicron axial structures

To demonstrate the potential of nsOCT technique to detect axial submicron structures experimentally, we imaged two Bragg gratings from OptiGrate Corp, USA with periodicities of 431.56 nm and 441.76 nm, respectively. Figure 4.5(a)

represents the conventional intensity-based OCT B-scan image from the two periodic samples. Figure 4.5(b) shows the corresponding nsOCT B-scan images formed as a colour map from the detected spatial periods. The information from high spatial frequency content is not preserved in conventional OCT processing. Consequently, the structural difference between the two samples cannot be detected in conventional intensity-based OCT B-scan images. However, from the proposed nsOCT method ~10 nm axial structural difference is easily visualized between the two Bragg gratings with ~2 nm detection accuracy. Each Bragg grating has a ~150 nm antireflection coating on the top surface which can be seen with a different colour in figure 4.5(b) nsOCT B-scan image. Figure 4.5(b) nsOCT B-scan image confirms that using the nsOCT method, we can detect nanoscale structural alterations within submicron axial structures.

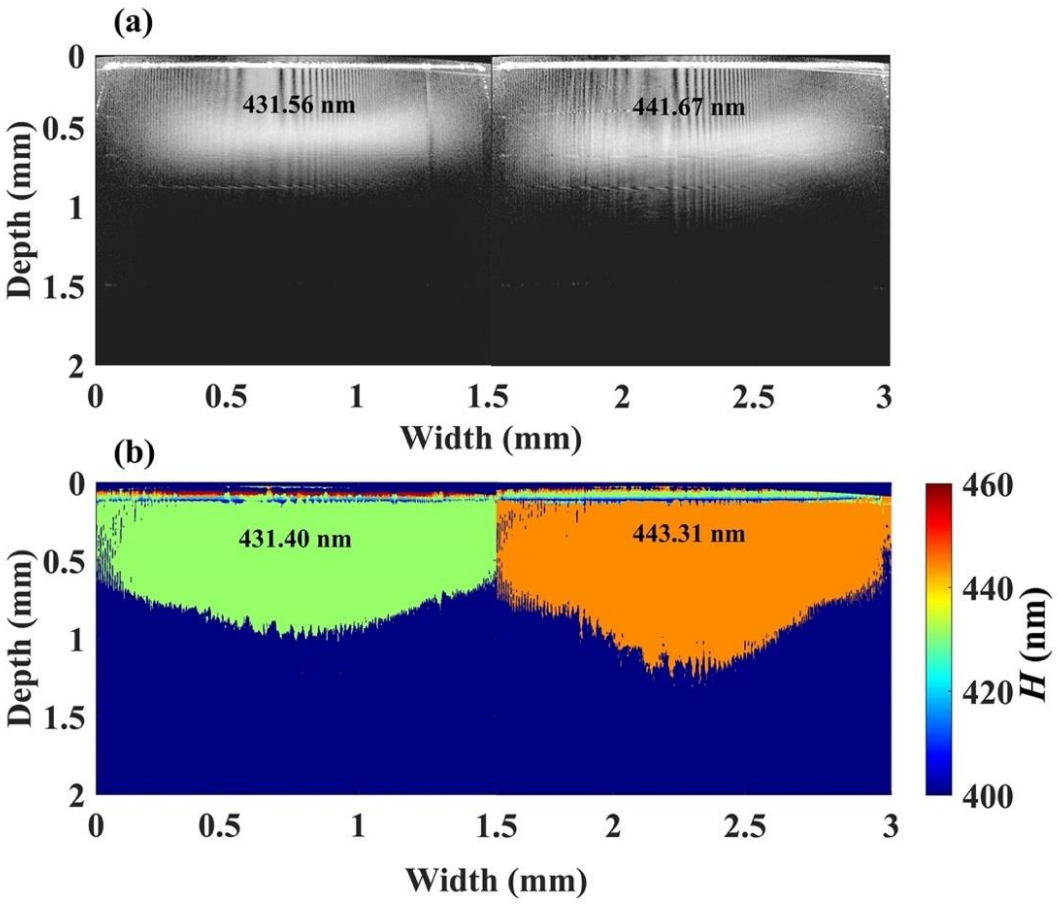

Fig. 4.5 Experimental demonstration of nsOCT technique using Bragg gratings, the detected axial spatial periods are 431.56 nm and 441.67 nm. (a) OCT B-scan image, (b) nsOCT B-scan image of the two Bragg gratings. The colour bar represents structural size in nanometres.

4.5.3 nsOCT approach to detect submicron structural changes within marginal area from human skin cancer tissue

After successful numerical and experimental validation of the nsOCT approach, we applied the nsOCT technique to fresh human skin cancer tissue samples. We collected skin tissue samples with healthy and lesional parts within one sample. After 3D OCT image acquisition from those collected tissue samples, the nsOCT technique was applied to distinguish both regions with an intervening margin area. Here, we show three conventional OCT and corresponding nsOCT en face images from a 3D volume image. Figures 4.6(a), 4.6(d), and 4.6(g) represent conventional intensity-based OCT en face images at depths of 200 μm, 400 μm, and 600 μm (from the top surface of the tissue), respectively from the acquired 3D volume. It is impossible to detect structural changes between healthy and lesion regions from the conventional OCT en face images in Figures. 4.6(a), 4.6(d), and 4.6(g). Figures 4.6(b), 4.6(e), and 4.6(h) represent nsOCT en face images which were constructed from the complex spectral interference OCT signal. In the nsOCT en face images, colour code mapping represents the different dominant nanoscale structural sizes of the tissue. Within the nsOCT en face images, a null value for accurate spatial period measurement is set as a dark blue background colour and does not represent any structure. In contrast to conventional OCT, the nsOCT image is formed using different contrast mechanisms like the dominant size of the sub-micron structure at a given location.

Figures 4.6(c), 4.6(f), and 4.6(i) show the change in mean spatial periods from the healthy region to the lesion region of the nsOCT en face images 4.6(b), 4.6(e), and 4.6(h) respectively. The mean spatial period was calculated from the nsOCT en face images. From figure 4.6(c), it can be clearly observed that from the healthy region to lesional region, the mean spatial period (H_z) value increased from 469 ± 1.3 (mean spatial period ± standard deviation) nm to 478.9 ± 1.4 nm. Similarly, figure 4.6(f) and 4.6(i) shows the mean spatial period changing from 472.1 ± 1.0 nm to 478.8 ± 1.1 nm and from 472.2 ± 1.0 nm to 478.8 ±1.1 nm, respectively. Red dashed lines in Figures 4.6(c), 4.6(f), and 4.6(i) represent the mean spatial period values of each region. So, the mean spatial period of the structure has been increased from left to right side within the nsOCT enface images. According to the mean spatial period distribution in figures. 4.6(c), 4.6(f), and 4.6(i) the region where the slope changes represent the margin between the healthy and lesional regions of the tissue. The width of the margin is represented by the spacing between the two black straight lines in the figures. 4.6(c), 4.6(f), and 4.6(i). In the nsOCT enface images, the spacing between the two red curved lines represents the margin between the healthy and lesional regions. The spacing between the red curves in figures 4.6(b), 4.6(e), and 4.6(h) are determined according to the spacing between the two black straight lines in figures. 4.6(c), 4.6(f) and 4.6(i). From figures. 4.6(a), 4.6(d), and 4.6(g) it can be observed that conventional intensity-based OCT en face images cannot distinguish healthy and lesional regions. It can give only the intensity value at each point, which provides only reflectivity at a given location and does not convey any information about the structures below the resolution limit at that location. In contrast, the processed nsOCT en face images and the mean spatial period profile of these nsOCT en face images clearly show the differences in the spatial period within the healthy and lesional regions.

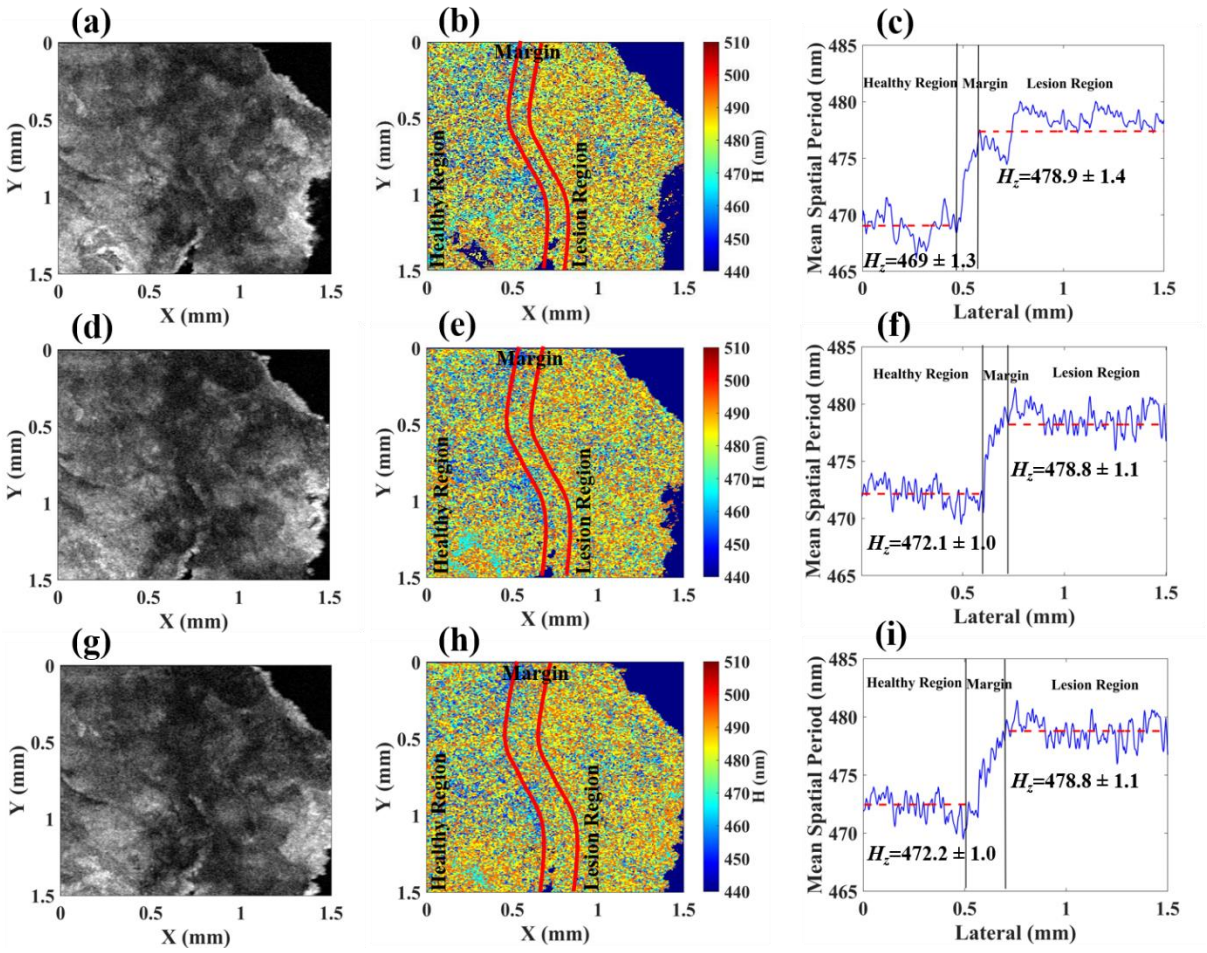

Fig. 4.6 (a), (d), and (g) conventional intensity-based OCT en face images of the tissue at the depths of ~200 µm, 400 µm, and 600 µm respectively. (b), (e), and (h) are corresponding nsOCT en face images with spatial period mapping, presenting the dominant structural size. The healthy, marginal, and lesional regions are separated by the red lines. The colour bar of the nsOCT en face images represents the spatial periods in nanometres. Plot (c), (f), and (i) show changes in the mean dominant spatial period of the structure between the two regions, defining an intervening marginal area in the nsOCT en face images.

Further we have constructed a series of repeating experiments on different fresh skin tissues from the different patients under the same protocol and processing.

Analysing the experimental data of twelve tissue samples we made a summary of dominant spatial period changes between healthy and lesional regions as presented in table 4.1. Summarizing all the experimental data sets using the proposed nsOCT method, we found that from the nsOCT en face images (at a depth of ~200 μm) there is a consistent decrease of the mean spatial period (mean spatial period ± standard deviation) values to the healthy region, and it is providing a reasonably convincing verification of the nanoscale structural changes between the two regions.

Table 4.1 The means spatial period changes of the lesional and healthy regions

Tissue samples	Mean spatial periods (nm)		
	Lesion region	Healthy region	Shift
S1	482.0±1.3	475.7±1.4	6.7
S2	479.7±1.0	473.7±1.0	6.0
S3	478.8±1.2	472.2±1.0	6.6
S4	479.8±1.1	473.2±1.0	6.6
S5	477.8±1.3	468.0±1.3	9.8
S6	481.0±1.3	474.7±1.4	6.4
S7	480.8±1.0	475.8±1.3	5.0
S8	479.8±1.6	471.0±1.3	8.8
S9	483.0±1.3	476.8±1.5	6.2
S10	479.8±1.0	473.8±1.0	6.0
S11	480.0±1.0	475.13±1.7	5.0
S12	482.1±1.8	475.3±1.6	6.9

4.5.4 Structural sizes comparison between nsOCT technique and high-resolution confocal microscopy image from marginal area of human skin cancer tissue

Currently, stained tissue slides of formalin-fixed or paraffin-embedded tissue section images using a bright-field microscope are the gold standard to evaluate nanoscale morphological features. In addition to the nsOCT results to analysis the nanoscale structural changes, laser scanning confocal microscopy images were used for structural comparison. After OCT imaging, the same tissue sample was fixed with paraffin for confocal microscopy imaging. Laser scanning confocal microscopy enables imaging of lesional and healthy skin tissue at cellular resolution in the freshly excised fixed tissue block [5]. We used a 405 nm excitation wavelength and an objective lens with an *NA* (Numerical Aperture) of 0.9 for acquiring the image. The image consisted of 4096 × 4096 pixels covering an area of 225 × 225 μm, which corresponds to 55 nm/pixel with a lateral resolution of 166 nm. The confocal microscopy image of the tissue block is presented in figure 4.7(a). To validate the nsOCT results with the confocal microscopy image, spatial frequency changes of the structures within the two regions were calculated. To analyse the spatial frequency profiles, regions of interest marked by red square boxes were taken from the confocal image 4.7(a). We have analysed two hundred vertical line profiles from the red square boxes. To obtain the spatial period distribution of the structures, we applied Fourier transforms on these line profiles. The median spatial frequency/period (MSP) of the spectrum was calculated after the Fourier analysis of the spectrum profiles [47]. From the two hundred vertical line profiles, average MSP was calculated to distinguish the spatial period changes of the structures within the healthy and lesional regions. Figures 4.7(c) and 4.7(d) show the spatial period profile of the median spatial period values from the lesional and healthy regions, respectively. In figures 4.7(c) and 4.7(d) the red dotted line represents the median spatial period values from the lesional and healthy regions. From the red dotted line, it can be

observed that the median spatial period is higher, or it is shifted towards the right of the spectrum for the lesional region. It indicates an increase in the spatial period of the structures within the lesional region compared to the healthy region. This study supports our results acquired using the nsOCT technique. Figure 4.7(b) box plot shows the distribution of the mean spatial periods of healthy and lesional regions and it is calculated from the confocal image line profile of figure 4.7(a). The box plot indicates that the spatial period of the nanoscale structures within the lesional region increased compared to the healthy region. The mean spatial period distribution of the healthy region is 638 ± 107 nm (mean SP ± standard deviation) and for the lesional region is 765 ± 135 nm. From the confocal microscope image, each red boxes line profile was analyzed for statistical t-test comparison of the median spatial period values of the healthy and lesional regions. Paired t-test results show a significant difference (p <3.48x10^{-24}) in spatial period between the healthy and lesional regions. Thus, the Fourier analysis results of the confocal microscopy images support the results acquired using the nsOCT technique. The higher structural size in the lesional region could be attributed to nuclear enlargement, increased nuclear-to cytoplasmic ratio, nuclear membrane irregularities, hyperchromasia, and abnormal chromatin distribution. In the lesional region, cells are also likely to have an increased volume of genetic material as well as altered nuclear envelope shape. All these factors may also contribute to the differing observation between healthy and lesional regions [57]. Particularly in skin, the basal layer of the epidermis contains multiplying keratinocytes. Terminally differentiating progeny leave this layer and enlarge progressively as they move outward through the spinous layer. The size of the cell is related to the degree of its terminal differentiation. In cell culture studies, human keratinocyte nuclei were found to vary from 3-10 microns to 11-20 microns in diameter [58-60] during progression from benign to malignant. Further investigation is required to compare the nsOCT results with the nuclear components structural sizes of the cancer cell.

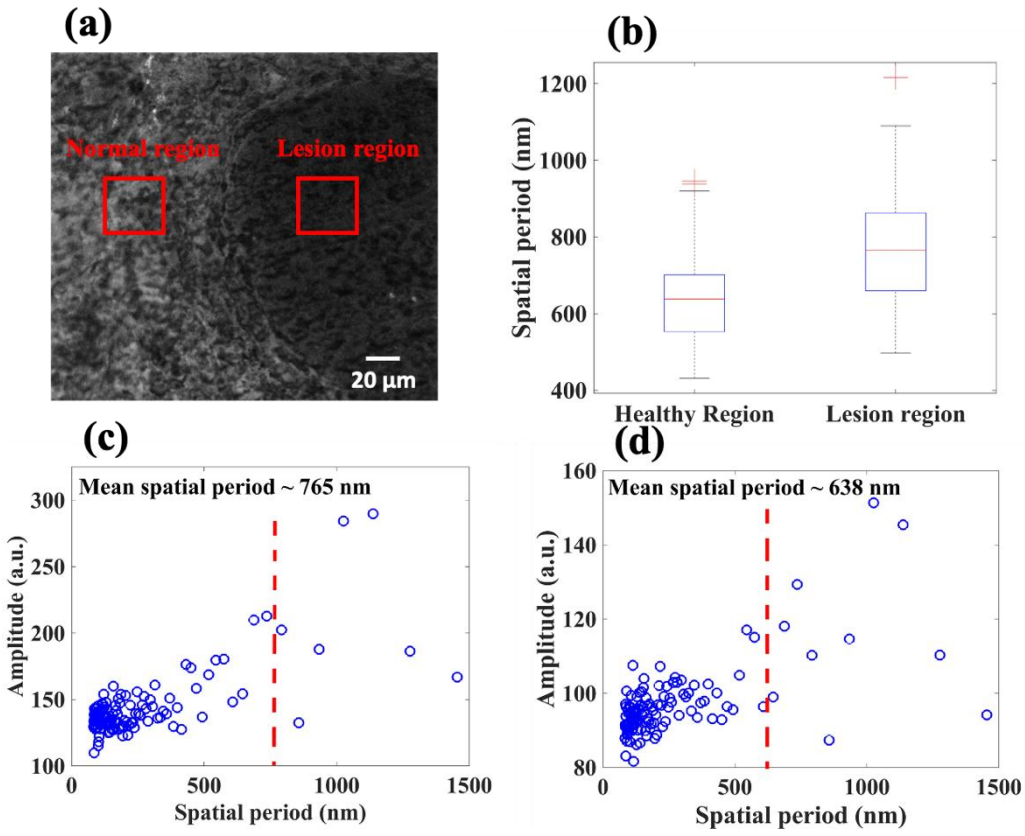

Fig. 4.7 (a) Confocal microscopy image of the tissue sample. Line profiles of the selected red square box regions were taken for spatial period profile measurements using Fourier transform (b) box plot showing the spatial period distribution of the healthy and lesional regions. (c) and (d) spatial period profile obtained from selected lesional and healthy regions of the tissue.

4.5.5 Healthy and lesional regions structure comparison from H&E slide image using high-resolution light microscope

We used an Olympus light microscopy of 580 nm wavelength and an objective lens with an NA (Numerical Aperture) 0.75 for acquiring the H&E slide image. Image consisted of 2056 X 1920 pixels covering an area of 283 X 212 mm, which corresponds to 110 nm/pixel with a lateral resolution of 286 nm. The light

microscopy image of the H&E slide is presented in figure 4.8(a). To validate the nsOCT results with the light microscopy image, spatial frequency changes of the structures within the two regions have been calculated. To analyse the spatial frequency profiles black square boxes regions were taken of the light microscope image 4.8(a). We have analysed two hundred vertical line profiles from the black square boxes. To obtain the spatial period distribution of the structures, Fourier transforms have been applied on these line profiles. Median spatial frequency/period (msf) of the spectrum was calculated after the Fourier analysis of the spectrum profiles. Figure 4.8(b) box plot shows the distribution of the mean spatial periods of healthy and lesion regions, and it is calculated from the line profiles of figure 4.8(a). The box plot indicates that the spatial period of the nanoscale structures within the lesional region increased compared to the healthy region. The mean spatial period distribution of the healthy region is 837 ± 0.5 nm (mean SP ± standard deviation) and for the lesional region is 900 ± 0.3 nm.

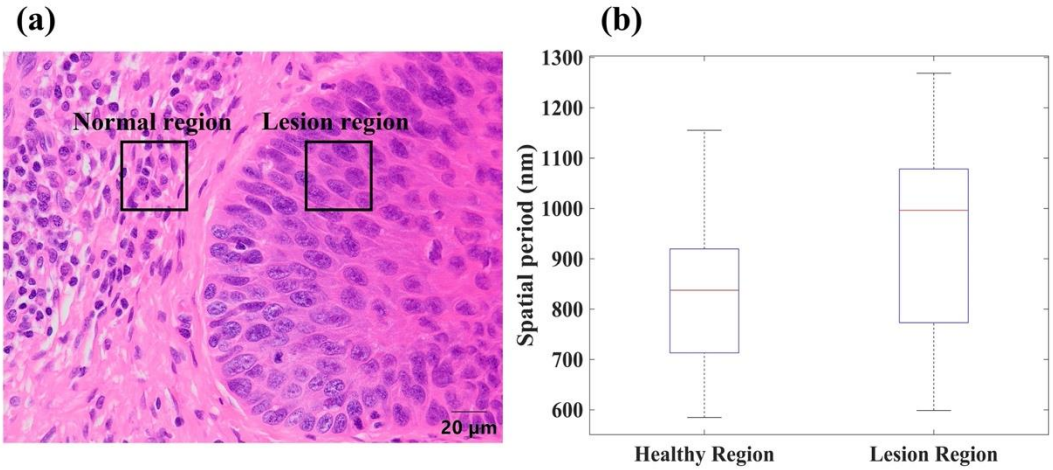

Fig. 4.8 (a) Histological sectioning image of the tissue sample. Line profiles of the selected black square boxes region were taken for spatial period profile measurements using Fourier transform (b) box plot showing the spatial period distribution of the healthy and lesional regions.

4.6 Conclusions

This chapter described differences between the nanoscale structure of healthy and lesional/cancerous regions, undetectable using conventional OCT, can be clearly detected by the nsOCT approach. Using nsOCT we demonstrated the ability to detect the depth-resolved structural changes within a 3D tissue sample and visualize the margin between the healthy and lesional/cancerous regions at different depths. By increasing the sensitivity of OCT to nanoscale structural changes within the sample, the described nsOCT approach bridges the gap between high resolution imaging and enhanced depth of imaging in OCT. The detected dynamic range of the nanometre length scale sensitivity of the tissue structure depends on the illumination source spectral bandwidth. The chapter discussed the advantages of using broadband light source like supercontinuum laser. Within the detected broader spectral range revealed the different structural information. Therefore, all the detected tissue structural sizes are within our illumination bandwidth range. There may be some other axial structural sizes within the tissue beyond our detection range. To detect those axial structures, further investigation with a larger illumination source bandwidth OCT system would be required. Nevertheless, we demonstrated the ability of the nsOCT to detect the depth-resolved structural changes and visualize the margin between the healthy and lesional/cancerous regions using this limited bandwidth of spatial frequencies. This chapter also discussed a comparative study, where confocal microscopy was used to detect nanometre scale structural changes at different bandwidths of structural sizes. This comparative study shows a similar trend to the nsOCT results. A corresponding study with other bandwidths of the lower spatial frequencies was done using histological images. The results demonstrate that for both nsOCT and confocal microscopy, the measured spatial period, or dominant structural sizes in the lesional region is higher compared to the healthy region for both images.

As a future study, we believe that the nsOCT method can be used as a tool to detect and monitor skin cancer at an early stage, possibly in a pre-invasive phase, which may facilitate early clinical intervention. Implementation in real-time would allow more confident surgery about the marginal area of the skin cancer region and avoid hospital stay/revisit. To further develop this technique for *in vivo* imaging applications especially in clinical imaging during the biopsy process and comparison with the nsOCT technique to detect the healthy and lesional/cancerous region along with the marginal area is required. Further, the nsOCT technique can be used to study the morphological changes in any samples, where the conventional OCT is used. For example, nsOCT can be applied for study of some low scattering *ex vivo* biological tissues like cornea of the eye, where OCT is already well established for clinical ophthalmic imaging application. In the next chapter we studied the nanoscale structural changes in cornea using corneal cross-linking treatment as another nsOCT application.

References:

1. R. W. H. Smits, et al. “Resection Margins in Oral Cancer Surgery: Room for Improvement,” *Head & Neck.* **38**(S1), E2197-E2203 (2016).
2. P. Horwich, C. MacKay, M. Bullock, et al. “Specimen oriented intraoperative margin assessment in oral cavity and oropharyngeal squamous cell carcinoma,” *J. Otolaryngology-Head Neck Surg.* **50**(1), 1-12 (2021).
3. R. Noorlag, R. de Bree, M. J. Witjes, “Image-guided surgery in oral cancer: towards improved margin control,” *Curr. Opin. Oncol.* **34**(3), 170-176 (2022).

4. Z. Hamdoona, W. Jerjes, G. McKenziec, A. Jayb, C. Hopper, “Optical coherence tomography in the assessment of oral squamous cell carcinoma resection margins,” *Photodiagn. Photodyn. Ther.* **13**, 211–217 (2016).
5. V. Ahlgrimm-Siess et al., “Confocal microscopy in skin cancer,” *Curr. Dermatol. Rep.* **7**(2), 105–118 (2018).
6. M. Agozzino, S. Gonzalezb, M. Ardigò, “Reflectance Confocal Microscopy for Inflammatory Skin Diseases,” *Actas Dermo-Sifiliogr* **107**(8), 631-639 (2016).
7. P. J. Caspers, G. W. Lucassen, G. J. Puppels, “Combined *In Vivo* Confocal Raman Spectroscopy and Confocal Microscopy of Human Skin,” *Biophys. J.* **85**(1), 572-580 (2003).
8. B. R. Masters, P. T. So, and E. Gratton, “Multiphoton excitation fluorescence microscopy and spectroscopy of *in vivo* human skin,” *Biophys. J.* **72**(6), 2405-2412 (1997).
9. J. G. Fujimoto, C. Pitris, S. A. Boppart, and M. E. Brezinski, “Optical Coherence Tomography: An Emerging Technology for Biomedical Imaging and Optical Biopsy,” *Neoplasia* **2**(1-2), 9-25 (2000).
10. D. Huang, E. A. Swanson, C. P. Lin, J. S. Schuman, W. G. Stinson, W. Chang, M. R. Hee, T. Flotte, K. Gregory, C. A. Puliafito, and J. G. Fujimoto, “Optical coherence tomography,” *Science* **254**(5035), 1178–1181 (1991).
11. W. Drexler, U. Morgner, R. K. Ghanta, F. X. Kärtner, J. S. Schuman, and J. G. Fujimoto, “Ultrahigh-resolution ophthalmic optical coherence tomography,” *Nat. Med.* **7**(4), 502–507 (2001).
12. M. Mujat, R. C. Chan, B. Cense, B. H. Park, C. Joo, T. Akkin, T. C. Chen, and J. F. de Boer, “Retinal nerve fibre layer thickness map determined from optical coherence tomography images,” *Opt. Express* **13**(23), 9480–9491 (2005).

13. X. Yao, Y. Gan, C. C. Marboe, and C. P. Hendon, “Myocardial imaging using ultrahigh-resolution spectral domain optical coherence tomography,” *J. Biomed. Opt.* **21**(6), 061006 (2016).
14. G. J. Tearney, H. Yabushita, S. L. Houser, H. T. Aretz, I.-K. Jang,K. H. Schlendorf, C. R. Kauffman, M. Shishkov, E. F. Halpern, and B. E. Bouma, “Quantification of Macrophage Content in atherosclerotic plaques by Optical Coherence Tomography,” *Circulation* **107**(1),113–119 (2003).
15. S. A. Boppart, W. Luo, D. L. Marks, and K. W. Singletary, “Optical Coherence Tomography: Feasibility for Basic Research and Image-guided Surgery of Breast Cancer,” *Breast Cancer Res. Treat.* **84**(2), 85–97 (2004).
16. F. Zuluaga, M. Follen, I. Boiko, A. Malpica, and R. Richards-Kortum, “Optical coherence tomography: A pilot study of a new imaging technique for noninvasive examination of cervical tissue,” *Am. J. Obstet. Gynecol.* **193**(1), 83–88 (2005).
17. L. L. Otis, B. W. Colston, M. J. Everett, and H. Nathel, “Dental optical coherence tomography: A comparison of two in vitro systems,” *Dentomaxillofac Radiol.* **29**(2), 85–89 (2000).
18. Z. Freitas, D. M. Zezell, N. D. Vieira, A. C. Ribeiro, and A. S. L. Gomes, “Imaging carious human dental tissue with optical coherence tomography,” *J. Appl. Phys.* **99**(2), 024906 (2006).
19. J. Olsen, J. Holmes, and G. B. E. Jemec, “Advances in optical coherence tomography in dermatology—a review,” *J. Biomed. Opt.* **23**(4), 040901 (2018).
20. N. M. Israelsen, M. Maria, M. Mogensen, S. Bojesen, M. Jensen, M. Haedersdal, A. Podoleanu, and O. Bang, “The value of ultrahigh resolution OCT in dermatology-delineating the dermo-epidermal junction, capillaries in the dermal papillae and vellus hairs,” *Biomed. Opt. Express* **9**(5), 2240–2265 (2018).

21. M. Mogensen, L. Thrane, T. M. Jørgensen, P. E. Andersen, and G. B. Jemec, “OCT imaging of skin cancer and other dermatological diseases,” *J. Biophoton* **2**(6–7), 442–451 (2009).
22. A. Levine, K. Wang, O. Markowitz, “Optical Coherence Tomography in the Diagnosis of Skin Cancer,” *Dermatol. Clin.* **35**(4), 465-488 (2017).
23. G. Humbert et. al., “Supercontinuum generation system for optical coherence tomography based on tapered photonic crystal fibre,” *Opt. Express* **14**(4), 1596-1603 (2006).
24. M. Szkulmowski et al., “Quality improvement for high resolution *in vivo* images by spectral domain optical coherence tomography with supercontinuum source” *Opt. Commun.* **246**(4), 569–578 (2005).
25. K. C. Zhou et al., “Optical coherence refraction tomography,” *Nat. Photonics* **13**(11), 794–802 (2019).
26. K. C. Zhou et al., “Spectroscopic optical coherence refraction tomography,” *Opt. Lett.* **45**(7), 2091-2094 (2020).
27. C. K. Chang et al., “Segmentation of nucleus and cytoplasm of a single cell in three-dimensional tomogram using optical coherence tomography,” *J. Biomed. Opt.* **22**(3), 036003 (2017).
28. J. F. de Boer, R. Leitge, & M. Wojtkowski, “Twenty-five years of optical coherence tomography: The paradigm shift in sensitivity and speed provided by Fourier domain OCT [Invited]”. *Biomed. Opt. Express* **8**(7), 3248–3280 (2017).
29. L. Bernstein, A. Ramier, J. Wu, V. D. Aiello, M. J. Béland, C. P. Lin, and S. H. Yun, “Ultrahigh resolution spectral-domain optical coherence tomography using the 1000–1600 nm spectral band,” *Biomed. Opt. Express* **13**(4), 1939-1947 (2022).
30. J. Yi, A. J. Radosevich, J. D. Rogers, S. C. P. Norris, IR Çapoglu, A. Taflove, and V. Backman, “Can OCT be sensitive to nanoscale structural alterations in biological tissue?” *Opt. Express* **21**(7), 9043–9059 (2013).

31. J. Yi, A. J. Radosevich, Y. Stypula-Cyrus, N. N. Mutyal, S. M. Azarin, E. Horcher, M. J. Goldberg, L. K. Bianchi, S. Bajaj, H. K. Roy, and V. Backman, "Spatially resolved optical and ultrastructural properties of colorectal and pancreatic field carcinogenesis observed by inverse spectroscopic optical coherence tomography," *J. Biomed. Opt.* **19**(3), 036013 (2014).
32. R. K. Wang and A. L. Nuttall, "Phase-sensitive optical coherence tomography imaging of the tissue motion within the organ of Corti at a sub nanometre scale: a preliminary study," *J. Biomed. Opt.* **15**(5), 056005 (2010).
33. S. Alexandrov, S. Uttam, R. K. Bista, K. Staton, and Y. Liu, "Spectral encoding of spatial frequency approach for characterization of nanoscale structures," *Appl. Phys. Lett.* **101**(3), 033702 (2012).
34. S. Alexandrov, J. McGrath, H. Subhash, F. Boccafoschi, C. Giannini, and M. Leahy, "Novel approach for label free super-resolution imaging in far field," *Sci. Rep.* **5**(1), 13274 (2015).
35. S. Alexandrov, J. McGrath, C. J. R. Sheppard, F. Boccafoschi, C. Giannini, T. Sibillano, H. Subhash, J. Hogan, and M. Leahy, "Label-free ultra-sensitive visualization of structure below the diffraction resolution limit," *J. Biophotonics* **11**(7), e201700385 (2018).
36. S. Uttam, S. Alexandrov, R. K. Bista, and Y. Liu, "Tomographic imaging via spectral encoding of spatial frequency," *Opt. Express* **21**(6), 7488–7504 (2013).
37. S. Alexandrov, Shikhar Uttam, Rajan K. Bista, Chengquan Zhao, and Yang Liu, "Real-time quantitative visualization of 3D structural information," *Opt. Express* **20**(8), 9203-9214 (2012).
38. S. Alexandrov, Shikhar Uttam, Rajan K. Bista, and Yang Liu, "Spectral contrast imaging microscopy," *Opt. Lett.* **36**(17), 3323-3325, (2011).

39. S. Alexandrov, H. Subhash, and M. Leahy, “Nanosensitive optical coherence tomography for the study of changes in static and dynamic structures,” *Quantum Electron.* **44**(7), 657–663 (2014).
40. S. Alexandrov, H. M. Subhash, A. Zam, and M. Leahy, “Nanosensitive optical coherence tomography,” *Nanoscale* **6**(7), 3545–3549 (2014).
41. S. Alexandrov, H. M. Subhash, A. Zam, and M. Leahy, “Nanosensitive Fourier domain optical coherence tomography inspection system,” Patent US 20160238370 A1, Issued July 3, 2018. European Patent office patent EP3055643 B1 (2019).
42. Y. Zhou, et al., “Noninvasive detection of nanoscale structural changes in cornea associated with cross-linking treatment,” *J. Biophotonics* **13**(6), e201960234 (2020).
43. C. Lal, S. Alexandrov, S. Rani, Y. Zhou, T. Ritter, and M. Leahy, “Nanosensitive optical coherence tomography to assess wound healing within the cornea,” *Biomed. Opt. Express* **11**(7), 3407-3422 (2020).
44. N. Das, S. Alexandrov, Y. Zhou, E. K. Gilligan, R. M. Dwyer, and M. Leahy, “Nanoscale structure detection and monitoring of tumour growth with optical coherence tomography”, *Nanoscale Adv.* **2**(7), 2853–2858 (2020).
45. R. Dsouza, J. Won, G. L. Monroy, M. C. Hill, R. G. Porter, M. A. Novak, and S. A. Boppart, “*In vivo* detection of nanometre-scale structural changes of the human tympanic membrane in otitis media,” *Sci. Rep.* **8**(1), 8777 (2018).
46. S. Alexandrov, A. Arangath, Y. Zhou, M. Murphy, N. Dufy, K. Neuhaus, G. Shaw, R. McAuley, and M. Leahy, “Accessing depth-resolved high spatial frequency content from the optical coherence tomography signal,” *Sci. Rep.* **11**(1), 17123 (2021).

47. F. E. Robles, C. Wilson, G. Grant, and A. Wax, "Molecular imaging true-colour spectroscopic optical coherence tomography," *Nat. Photonics* **5**(12), 744-747 (2011).
48. Y. Zhao, J. R. Maher, J. Kim, M. A. Selim, H. Levinson, and A. Wax, "Evaluation of burn severity *in vivo* in a mouse model using spectroscopic optical coherence tomography," *Biomed. Opt. Express* **6**(9), 3339-3345 (2015).
49. R. Qian, W. Huang, R. P. McNabb, K. C. Zhou, Q. H. Liu, A. N. Kuo, and J. A. Izatt, "Ocular anterior chamber blood cell population differentiation using spectroscopic optical coherence tomography," *Biomed. Opt. Express* **10**(7), 3281-3300 (2019).
50. N. M. Israelsen, M. Maria, M. Mogensen, S. Bojesen, M. Jensen, M. Haedersdal, A. Podoleanu, and O. Bang, "The value of ultrahigh resolution OCT in dermatology - delineating the dermo-epidermal junction, capillaries in the dermal papillae and vellus hairs," *Biomed. Opt. Express* **9**(5), 2240-2265 (2018).
51. M. Nasiriavanakia, J.W. Fakhourya, S. Daveluya, "Commentary on "OCT image atlas of healthy skin on sun-exposed areas"," *J. Skin* **2**(2), 30 (2018).
52. S. Schuh, C. Ruini, M. K. E. Perwein, F. Daxenberger, C. Gust, E. C. Sattler, J. Welzel, "Line-Field Confocal Optical Coherence Tomography: A New Tool for the Differentiation between Nevi and Melanomas?" *Cancers* **14**(5), 1140 (2022).
53. W. Zhou, Z. Chen, S. Yang, and D. Xing, "Optical biopsy approach to basal cell carcinoma and melanoma based on all-optically integrated photoacoustic and optical coherence tomography," *Opt. Lett.* **42**(11), 2145-2148 (2017).
54. R. Dey, Y. Zhou, S. Alexandrov, K. Neuhaus, A. Nolan, M. Leahy, "Simple Characterization Scheme for Optical Coherence Tomography

Systems with Application to a Commercial and a Near-Isometric Resolution Fibre-Based System," *IEEE Photonics J.* **14**(1), 1-11 (2022).

55. Y. Rao, N. P. Sarwade, and R. Makkar, "Modelling and Simulation of Optical Coherence Tomography on Virtual OCT," *Procedia Comput. Sci.* **45**, 644–650 (2015).
56. P. M. d. S. Carvalho, Optical coherence tomography Layout Simulation Using MATLAB®, FCTUC Física - Teses de Mestrado (Master Dissertation), University of Coimbra, APPENDIX B, 133–135 (2016).
57. E. G. Fischer, "Nuclear morphology and the biology of cancer cells," *Acta. Cytol.* **64**(6), 511-519 (2020).
58. Y. Barrandon, and H. Green, "Cell size as a determinant of the clone-forming ability of human keratinocytes," *Proc. of the Natl. Acad. of Sci.* **82**(16), 5390-5394 (1985).
59. P. R. Bergstresser, R. J. Pariser, and J. R. Taylor, "Counting and sizing of epidermal cells in normal human skin," *J. of Invest. Dermatol.* **70**(5), 280-284 (1978).
60. D. Zink, A. H. Fischer, and J. A. Nickerson, "Nuclear structure in cancer cells," *Nat. Rev. cancer*, **4**(9), 677-687 (2004).

Chapter 5

Non-invasive detection of nanoscale structural changes in cornea associated with cross-linking treatment

5.1 Introduction

Corneal ectasia has the potential to cause significant vision impairment, particularly in its progressive form, which is characterized by the inherent structural weakness of the cornea [1, 2]. Keratoconus, the most prevalent type of corneal ectasia that affects approximately 1 in 375 individuals worldwide, is an ocular condition characterized by the degeneration of the cornea due to thinning. This leads to a localized reduction in the corneal curvature radius and the presence of abnormal wavefront aberrations [3-5]. Keratoconus is a progressive, non-inflammatory disease that results in instability of the corneal structure and may eventually necessitate a corneal transplant. In recent years, a non-surgical treatment known as corneal cross-linking (CXL) has been established as an effective method for halting the progression of keratoconus, thereby allowing patients to avoid a corneal transplant [6-9]. CXL involves the use of ultraviolet-A (UVA) light with a central wavelength of 365 nm and a photosensitizer (riboflavin, vitamin B2) to modify the biomechanical properties of the corneal tissue [10-12]. It is considered a minimally invasive procedure that strengthens the connections between collagen fibrils in the corneal stroma. The U.S. Food and Drug Administration (FDA) granted approval for CXL in April 2016 [13].

Despite having been used clinically for several years, there are still ongoing investigations into certain principles and underlying processes of corneal cross-linking (CXL), including the role of oxygen, optimal treatment duration, and methods for monitoring and assessing the treatment [14, 15]. The fundamental theory behind CXL is photo-polymerization, which involves the formation of chemical bonds between collagen, proteoglycans, and other proteins within the

corneal stroma. Several studies have reported that the increase in tissue stiffness is associated with modifications in mechanical properties, which are closely related to ultrastructural changes within the cross-linked cornea, such as alterations in collagen fibril characteristics [16, 17]. Detecting structural changes in the corneal stroma during the CXL procedure would enable a more thorough investigation of the healing processes and the effectiveness of medications. Furthermore, characterizing these structural changes could potentially improve optical monitoring and enhance treatment methods for repairing corneal damage in the future [18-22].

Transmission electron microscopy (TEM) and scanning electron microscopy (SEM) have been utilized to examine the relationship between mechanical behavior and changes in the corneal ultrastructure following CXL in rabbit eyes [23, 24]. While these technologies can provide clear imaging of the nanoscale structure, they are only suitable for in vitro samples. Another approach for detecting corneal ultrastructure is histology, which requires the examination of tissue anatomy and thus is applicable only to *ex vivo* tissue. Other methodologies, such as X-ray microscopy [25] and confocal microscopy [26, 27], also have their limitations, including potential harm from radiation damage, limited imaging area, or shallow imaging depth. These factors present challenges in the context of clinical eye diagnostics.

Optical coherence tomography (OCT) is a technique that was first introduced in 1991 by a team at the Massachusetts Institute of Technology (MIT) for visualizing changes in the human eye. It is based on optical low-coherence interferometry and utilizes the detection of the time delay and intensity of light reflections or back-scatterings from internal tissue structures to generate two-dimensional (2D) or three-dimensional (3D) cross-sectional tomographic images [28-30]. OCT has proven to be highly valuable for visualizing transparent and weakly scattering media, particularly the cornea, and has had a significant impact

in the field of ophthalmology [15, 31-33]. Recent advancements in OCT technology have also made it possible to image highly scattering tissues in other medical fields such as dermatology, gastroenterology, oncology, and interventional cardiology. With its high resolution, noninvasive nature, fast imaging speed, and ability to provide three-dimensional images, OCT bridges the gap between optical microscopy and currently available clinical imaging methods, offering both high-resolution imaging and depth information.

In recent years, there has been a significant increase in interest in the use of optical coherence tomography (OCT) for ophthalmic applications. One area that has greatly benefited from OCT technology is refractive surgery on the cornea, including procedures such as phakic intraocular lens implantation, laser-assisted in situ keratomileusis (LASIK) enhancement, and lamellar keratoplasty. The availability of OCT has opened up promising opportunities for therapeutic and diagnostic purposes in both research and clinical applications within the field of ophthalmology.

However, it's important to note that the spatial and axial resolution of OCT is inherently limited by the wavelength of the light source used and the optical components employed. While OCT has proven to be highly useful in various ophthalmic treatments, certain specific procedures involving the cornea, such as monitoring the cross-linking process, require image resolution in the nanometer range, as demonstrated through the use of transmission electron microscopy (TEM) and scanning electron microscopy (SEM) techniques [23, 34].

In this chapter, we will discuss the application of over-sampling nanosensitive optical coherence tomography (nsOCT) for investigating structural alterations within *ex vivo* bovine cornea during corneal cross-linking (CXL) treatment with nanoscale sensitivity. The nsOCT technique involves increasing the number of points within the detected bandwidth to extract high spatial frequency information from the interference spectra. To validate the nanoscale detection

capability of nsOCT, we conducted experiments using two periodic Bragg grating samples with known dimensional sizes, successfully distinguishing between them. For the investigation of corneal cross-linking, we followed the Dresden protocol, which is considered the gold standard for CXL treatment. Data from the corneas were recorded and analyzed at three time intervals: 1) after epithelium removal, 2) following a 30-minute riboflavin instillation, and 3) after a 30-minute UVA irradiation. We present over-sampling nsOCT B-scans and en face results at different depths within the cornea, consistently demonstrating the findings. The spatial periods of the cornea showed a slight increase after 30 minutes of riboflavin instillation, but a significant decrease after 30 minutes of UVA irradiation. These results indicate that over-sampling nsOCT has the potential to detect nano-sized structural changes that are valuable for improving corneal treatment methods.

5.2 Materials and Methods

5.2.1 Principle and demonstration of the over-sampling nsOCT

The scattering potential of a three-dimensional (3D) object can be reconstructed by analyzing the distribution of the complex amplitude of the light scattered by the object in the far zone. This reconstruction is achieved through a 3D inverse Fourier transform [35]. As discussed in the previous chapter, the spectral encoding of spatial frequency (SESF) approach has been utilized to characterize structures with nanoscale sensitivity. Building upon this theory, over-sampling nanosensitive optical coherence tomography (nsOCT) has been proposed as a label-free, depth-resolved sensing technique for probing structural changes at the nanoscale [40-45]. In this particular study, over-sampling is employed to increase the number of points in the reconstructed axial spatial frequency or period profiles. Conventional OCT techniques typically result in the loss of high-frequency information during the inverse Fourier transform process, limiting the

axial resolution to the micron level, which is determined by the spectral bandwidth of the light source used.

The nsOCT method utilizes spectral encoding to transfer the spectrally encoded axial spatial period from **K**-space to the reconstructed object space, with each axial spatial frequency being encoded with a specific wavelength. The signal processing steps for nsOCT are illustrated in a flowchart shown in figure 5.1. To enable over-sampling in nsOCT, we first process the interference spectra by performing preliminary modifications. These modifications include **K**-space linearization, removal of background noise, apodization, and dispersion compensation. After these initial steps, the processed spectra are decomposed into several sub-bands using Tukey windows, as typically done in nsOCT imaging. In order to reduce the spatial frequency range within each sub-band, we apply over-sampling by shifting the window with the same width. This means that the starting point for each processing shifts along with the spatial frequency, as depicted in figure 5.1(a). The Fast Fourier Transform (FFT) is then applied to each sub-band signal, generating amplitude profiles along all the imaging depths for a specific spatial frequency range, as shown in figure 5.1(b). By combining all the over-sampled spatial profiles, it becomes possible to reconstruct the dominant structural size of each voxel. This is achieved by identifying the medium spatial periods with the highest energy contribution, as indicated in figure 5.1(c). The collected complex amplitudes of the spectrum are converted to complex amplitudes of spatial frequencies based on a specific equation 4.16. The spatial periods of the structure (denoted as) can be determined using another equation 4.18. Finally, the nsOCT image is constructed by mapping the corresponding dominant spatial period to each voxel using an optimized thresholding approach.

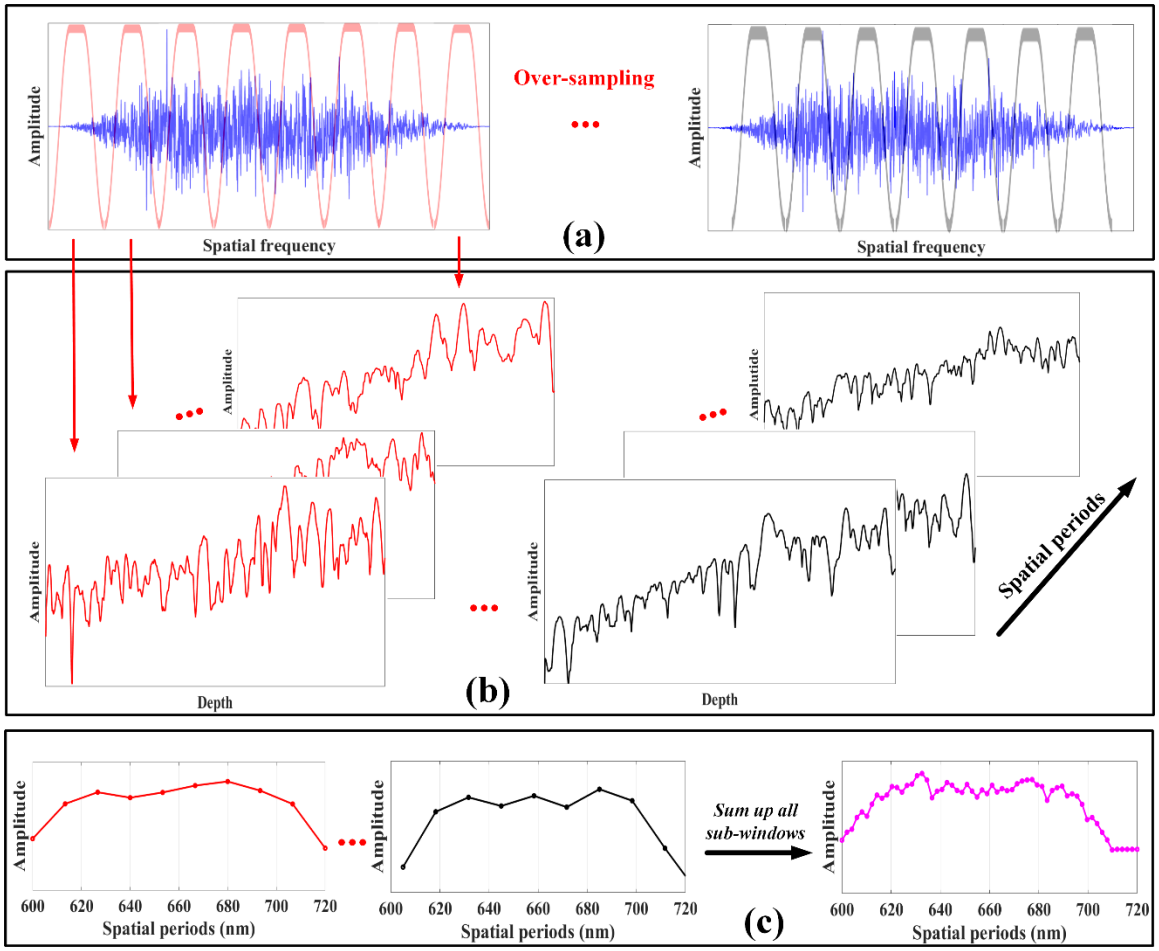

Fig. 5.1 Flowchart illustrates the steps involved in the over-sampling nsOCT signal processing. (a) Decompose axial spatial frequencies into multiple sub-bands and shift the dividing windows for over-sampling the spatial frequencies. (b) Fast Fourier Transform is applied to each sub-band to acquire the amplitude along different depths within each specific spatial frequency range. (c) The spatial period profiles are reconstructed by summing up the energy contributions from all sub-bands, and the dominant structural size for each voxel is obtained based on these reconstructed profiles.

5.2.2 Experimental validation of the proposed nsOCT method using sum-micron structures

To validate the proposed nsOCT method experimentally, we utilized two reflection Bragg gratings with periodicities of 431.6 nm and 441.7 nm from OptiGrate, Florida, United States. These gratings consisted of sinusoidal refractive index variations with a value of 1.483 ± 0.001. To simulate imaging conditions similar to real tissue, a two-layer plastic tape was placed on top of the Bragg gratings, along with a tissue paper layer, as shown in figure 5.2(a). In the image, the highly scattered region on the right side corresponds to the tissue paper.

Figure 5.2(a) and 5.2(b) represent the conventional intensity-based OCT B-scan and en face images, respectively. In these images, the structural differences between the Bragg gratings are not distinguishable since the high-frequency information is not available through standard OCT processing. However, by employing the proposed nsOCT method, both the nsOCT B-scan and en face images were constructed, mapping the spatial periods as shown in figure 5.2(c) and 5.2(d). These images clearly visualize the nanometre-scale structural difference (approximately 10 nm) between the two Bragg gratings. The spatial periods of the tape and tissue paper exhibit a diffuse distribution of various values due to the random nature of their structural sizes. Through these proof-of-concept demonstrations, we successfully confirm that the nsOCT method holds promise for sensing nanoscale structural alterations along the depth axis.

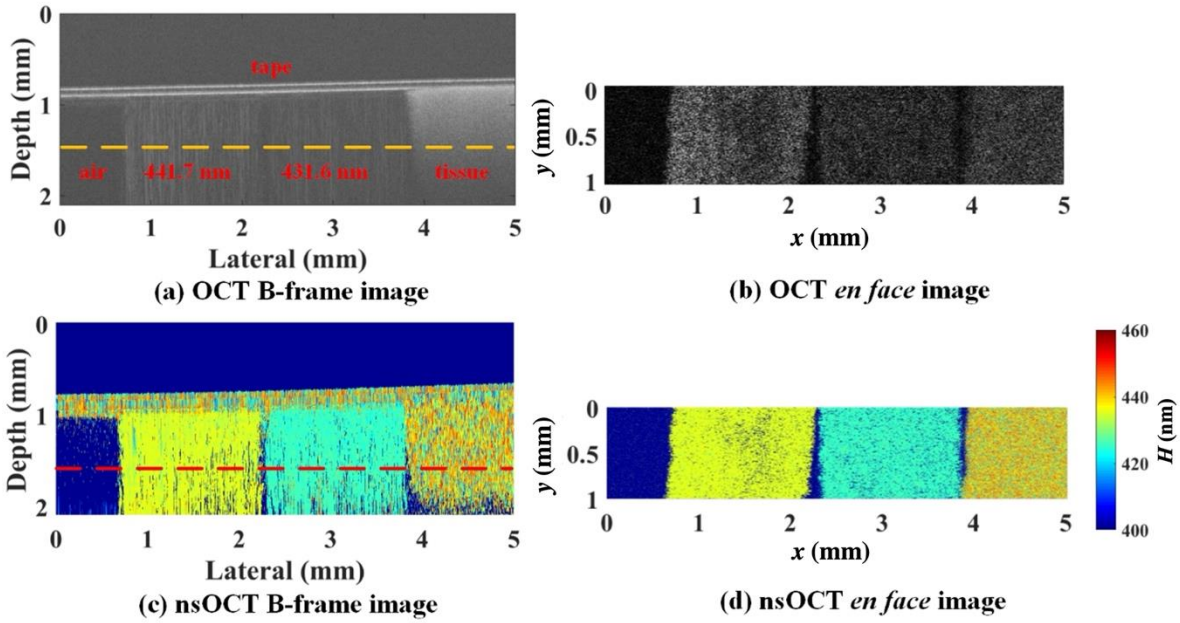

Fig. 5.2 Experimental validation of the over-sampling nsOCT method by both B-scan and en face images. The two periodicity-different Bragg gratings and a tissue paper were covered under a two-layer tape. (a, b) Conventional intensity-based OCT B-scan and en face image at the depth marked by the dashed line. (c, d) The corresponding nsOCT B-scan and en face image with spatial periods mapping, visualizing the nanoscale structural differences between the samples. The colour bar presents the spatial periods with unit nanometre.

5.2.3 Numerical and experimental realization of nsOCT and over-sampling nsOCT methods on phantoms

To provide a clearer understanding of the distinction between over-sampling nsOCT and the previous nsOCT method, we conducted simulations and experiments. In the simulation, we generated seven samples with varying axial periodicities: 425 nm, 428 nm, 431 nm, 434 nm, 437 nm, 440 nm, and 443 nm. The aim was to assess the capability of each method to detect and differentiate small structural differences. Figure 3 presents the results of the simulation. It

demonstrates that the over-sampling nsOCT technique allows for the discrimination of structural differences as small as 3 nm. On the other hand, the previous nsOCT method, without over-sampling, could only detect differences of 6 nm but was unable to distinguish such small differences effectively.

These finding obtained through simulation and provide clarity on the improved performance of over-sampling nsOCT in detecting and resolving finer structural differences compared to the previous nsOCT method. The implementation of over-sampling enables enhanced sensitivity and resolution, facilitating the differentiation of nanoscale variations that may not be discernible using conventional nsOCT approaches.

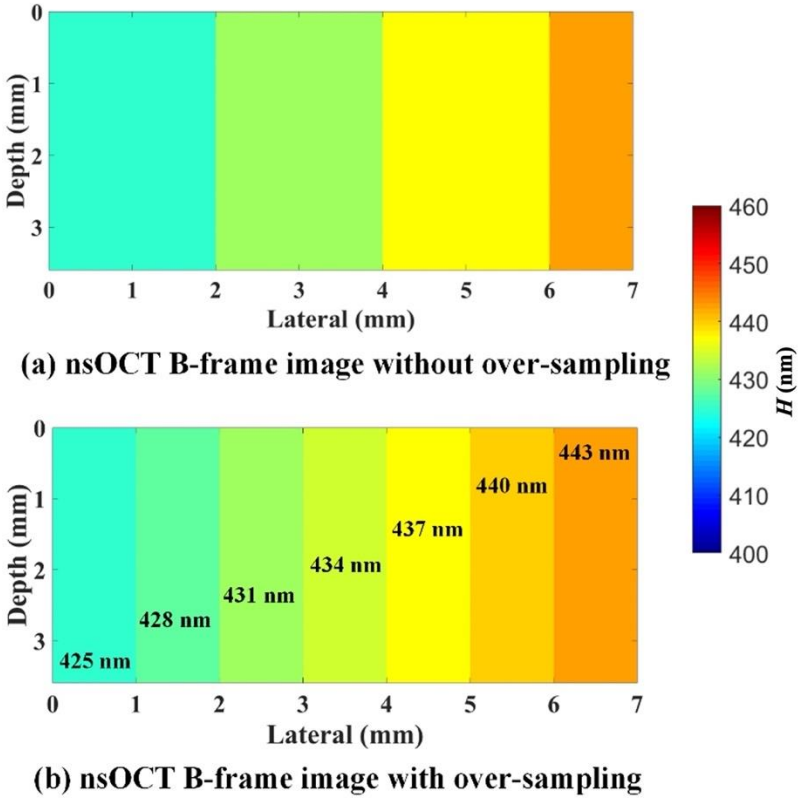

(a) nsOCT B-frame image without over-sampling

(b) nsOCT B-frame image with over-sampling

Fig. 5.3 Results of the nsOCT simulation with and without oversampling. (a) nsOCT without over-sampling can detect the difference of 6 nm but cannot distinguish very small difference, (b) nsOCT with over-sampling is able to distinguish the structural difference of 3 nm.

In the experiment, we continued to utilize Bragg gratings to demonstrate the performance of the over-sampling nsOCT method. For the Bragg grating with a periodicity of 431.6 nm, we measured a value of 430.4 nm (with an discrepancy of 1.2 nm) using the over-sampling nsOCT technique, while the previous nsOCT method yielded a measurement of 428.2 nm (with an discrepancy of 3.4 nm), as depicted in figure 5.4(a, b). This comparison clearly illustrates that over-sampling nsOCT provides higher measurement accuracy, enabling more precise determination of the structural periodicity. Similarly, for the Bragg grating with a periodicity of 441.7 nm, we obtained a measurement of 440.1 nm using the over-sampling nsOCT method, while the previous nsOCT method yielded a measurement of 438.2 nm, as demonstrated in figure 5.4(c, d).

These experimental results reaffirm the advantages of over-sampling nsOCT in terms of improved measurement accuracy. By incorporating over-sampling, the method enables more accurate determination of the structural periodicity, leading to enhanced precision in the measurement of nanoscale structural features.

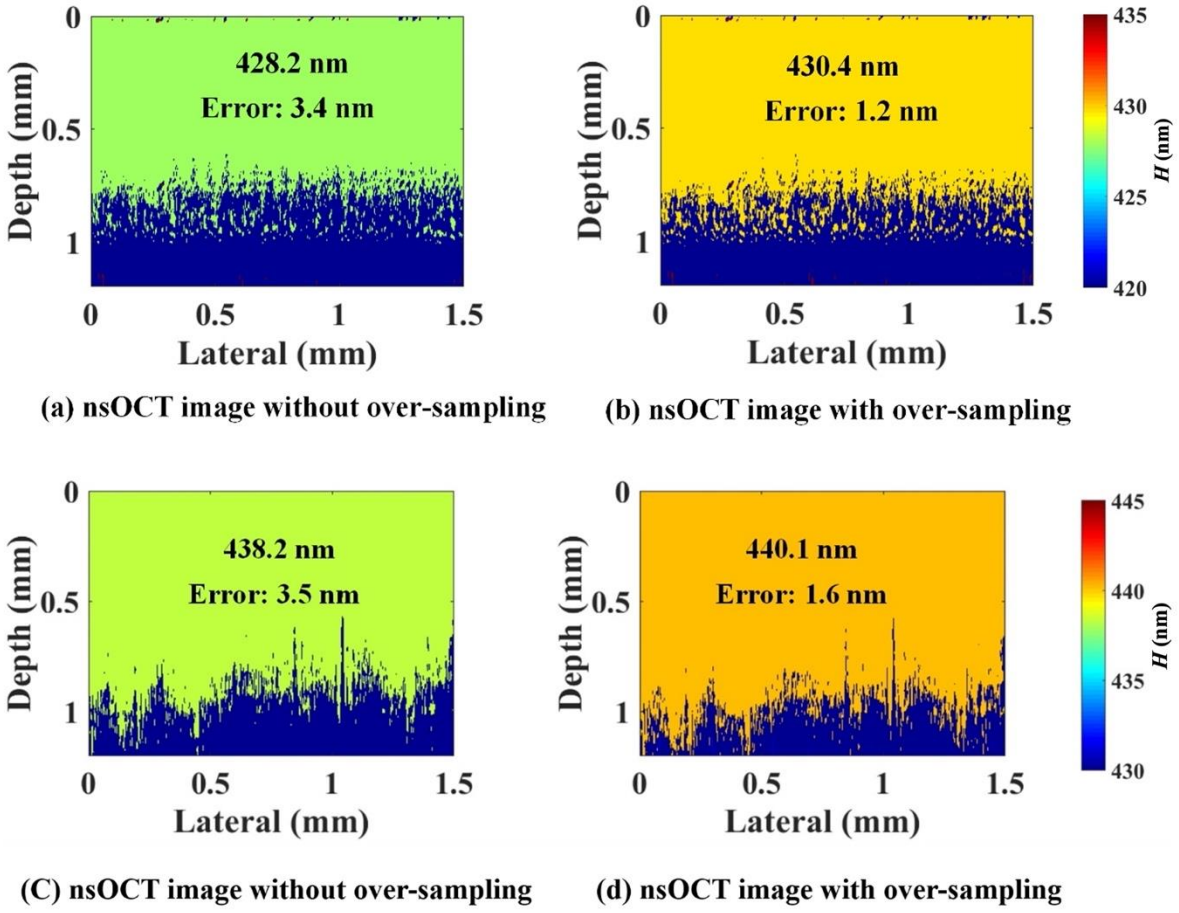

Fig. 5.4 Experimental results of the Bragg gratings with the axial periodicity of 431.6 nm and 441.7 nm. (a) The nsOCT without over-sampling presents a 428.2 nm structural size. Error is 3.4 nm. (b)The nsOCT with over-sampling shows a 430.4 nm structural size. Error is 1.2 nm. (c) The nsOCT without over-sampling presents a 488.2 nm structural size. Error is 3.5 nm. (d) The nsOCT with over-sampling shows a 440.1 nm structural size. Error is 1.6 nm. The colour bar present the spatial periods with unit nanometre.

5.2.4 *Ex vivo* bovine corneal cross-linking experiment

In the CXL experiments, we specifically chose bovine corneas to ensure a consistent sample quality. The bovine eyes were obtained from a local abattoir, Athenry Quality Meats Ltd, located in County Galway, Ireland. The eyes were

harvested in the evening following slaughter, within 2 hours post mortem, and were subsequently stored at a temperature of 4°C. The abattoir granted permission for the use of these eyes in research.

For the *ex vivo* studies, we selected eye globes with intact epithelium and clear corneas. The first step involved the removal of the epithelium using a stainless-steel spatula. The CXL process was then performed in a dark environment using riboflavin (MedioCROSS M, 0.1% Riboflavin, 1.1% HPMC) as the photosensitizer. UV-A light (UV-XTM 2000, IROC Innocross, Zurich, Switzerland) was used for the final irradiation, with an illumination spot size of 9.5 mm, an intensity of 3.0 mW/cm2, and an energy dose of 5.4 J/cm2.

Following the Dresden protocol, which is widely recognized as the current gold standard for CXL treatment, we conducted structural assessments at three distinct stages of the treatment process. These stages included immediately after epithelial removal, after a 30-minute riboflavin instillation, and after a 30-minute UVA irradiation, with additional continuous installation of riboflavin every 2 minutes during the UVA exposure.

5.2.5 Experimental system setup

For the data acquisition, a commercial spectral-domain optical coherence tomography (SDOCT) system (Telesto III, Thorlabs, Inc. New Jersey, United States) with an objective lens LSM03 (NA=0.055, lateral resolution=13 μm) was used in our experiments. This high-resolution OCT system, operating at the central wavelength of 1300 nm with sensitivity 96 dB at 76 kHz rate, can reach an axial resolution of 5.5 μm and imaging depth of 3.6 mm in air.

5.3 Results

5.3.1 Structural visualization of virgin and treated cornea from confocal microscope images

In our study, we utilized a laser scanning confocal microscopy system (FV 3000, Olympus) to examine the differences between untreated and treated corneas. The imaging process was carried out using a 405 nm excitation wavelength and an objective lens with a numerical aperture (NA) of 0.85 (UPLSAPO 20XO). Figure 5.5 illustrate the confocal microscopy images of both the virgin (untreated) and treated corneas. The virgin corneas exhibited highly reflective and clearly delineated cell nuclei with an oval shape, which are indicated by white arrows. No visualizations of keratocyte processes or collagen fibers were observed in these images. On the other hand, the crosslinked corneas displayed the presence of reflective interconnected stellate structures. These structures were characterized by elongated nuclei and the presence of keratocyte apoptotic bodies. The confocal microscopy images provide visual evidence of corneal crosslinking having occurred during the CXL treatment.

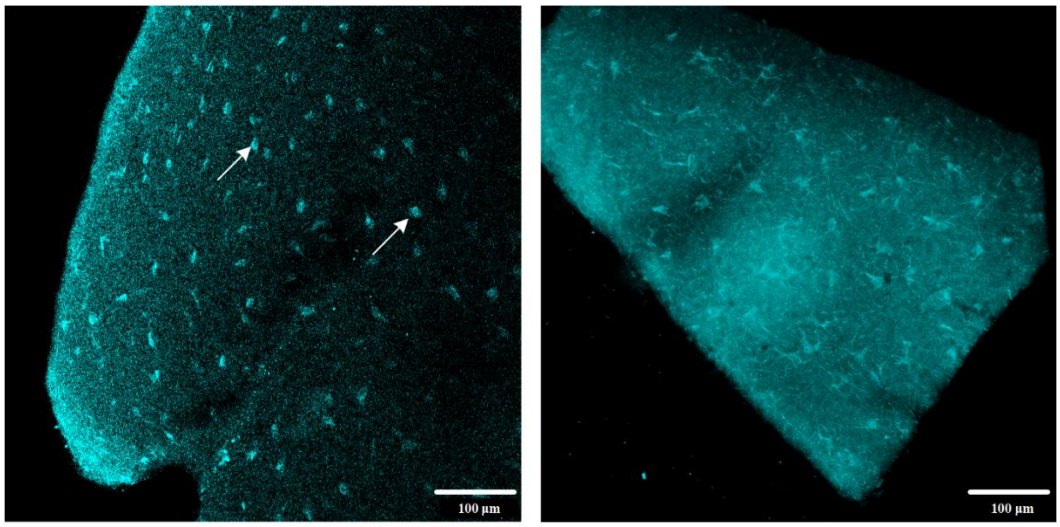

(a) Virgin cornea **(b) Treated cornea**

Fig. 5.5 Confocal microscopy images of the virgin and treated cornea. (a) The virgin corneas consist of highly reflective and well-demarcated cell nuclei with an oval shape, indicated by white arrows. (b) The treated cornea is populated with some reflective interconnected stellate structures, containing elongated nuclei and keratocyte apoptotic bodies. The scale bar is 100 μm.

5.3.2 Structural comparisons of virgin cornea, after riboflavin installation, and after CXL process using oversampling nsOCT technique

Figure 5.6(a, c, e) presents the intensity-based OCT B-scans corresponding to the three processing steps in the CXL treatment. In these conventional OCT images, it is not possible to identify structural changes that are smaller than the resolution limit. As a result, no discernible structural differences within the corneas can be observed. To overcome this limitation, we applied the proposed nsOCT method to analyze the structural responses during the CXL treatment. Figure 5.6(b, d, f) presents the nsOCT B-scans with spatial periods mapping. By employing the nsOCT technique, we can clearly visualize the structural alterations that occur during the treatment process. The nsOCT B-scans reveal that there are no apparent structural changes between the virgin cornea and the cornea after 30 minutes of riboflavin instillation, indicating a minor increase in spatial periods after riboflavin immersion. However, a significant decrease in spatial periods is observed after 30 minutes of UVA irradiation, indicating a notable reduction in structural size following the CXL treatment. In figure 5.6(f), the spatial periods after the CXL process are clearly detected to be smaller by several nanometres compared to figure 5.6(b, d).

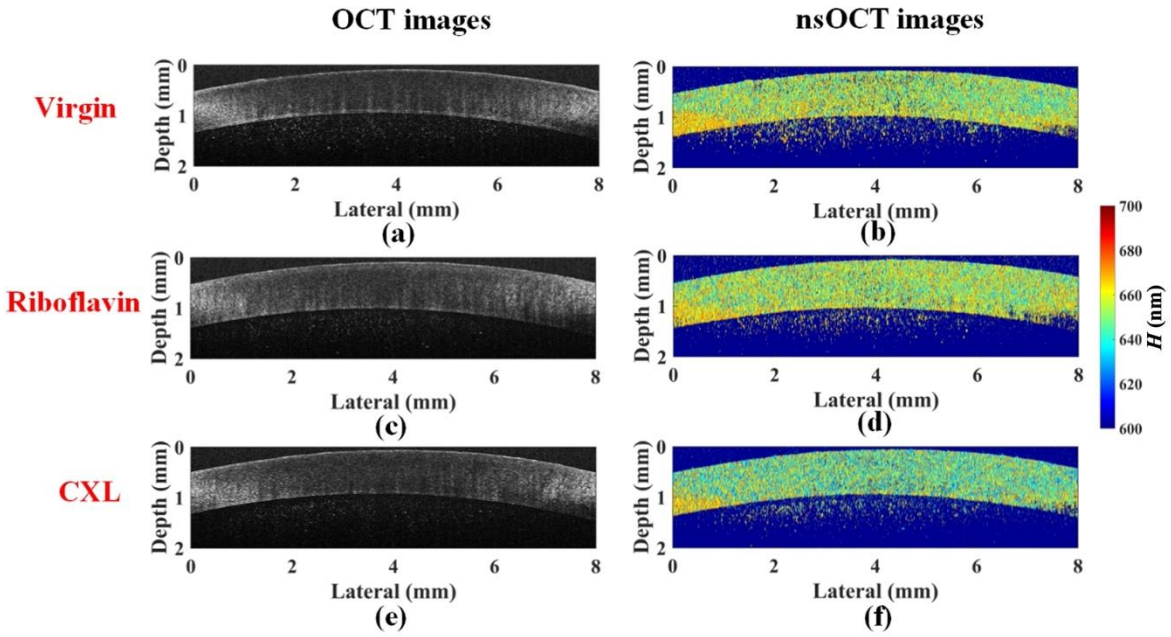

Fig. 5.6 B-scans of *ex vivo* bovine cornea during CXL treatment at three treating steps. (a, b) Both conventional OCT and nsOCT images acquired immediately after epithelial removal. (c, d) Images constructed after 30 min riboflavin instillation and (e, f) after 30 min UVA irradiation while finishing the treatment. The colour bar presents the spatial periods with unit nanometre.

To provide quantitative analysis of the structural variations associated with CXL treatment, we examined the histograms and boxplots of spatial period distributions for B-scans at all three steps. Figure 5.7(a, b, c) illustrates the spatial period results for one of the bovine corneas. The mean spatial periods for the virgin cornea, the cornea after 30 minutes of riboflavin instillation, and the cornea after 30 minutes of UVA irradiation were measured to be 657.1 nm, 658.1 nm, and 649.6 nm, respectively. These values indicate a slightly larger spatial size following riboflavin immersion but a significantly smaller size after the CXL procedure. This demonstrates the effectiveness of the CXL treatment in reducing the structural size of the cornea. Furthermore, the histograms of spatial period distributions also reveal the shift towards smaller structural sizes in the treated cornea. This can be observed from the histograms, which show a displacement

towards lower spatial period values, indicating the reduction in structural size after CXL treatment.

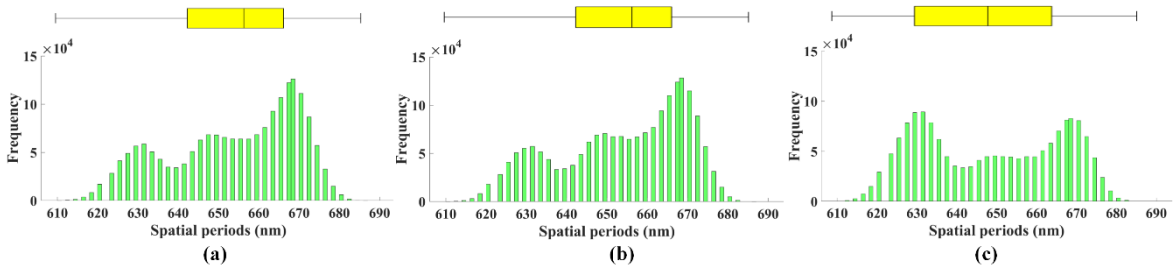

Fig. 5.7 Histogram and boxplot of spatial period distributions inside cornea associated with CXL treatment. (a) Virgin cornea with the mean spatial period of 657.1 nm. (b) The cornea after 30 minutes riboflavin instillation with the mean value of 658.1 nm. (c) The crosslinked cornea with the mean value of 649.6 nm, with the histogram showing a shift towards lower spatial period compared with (a) and (b).

In our study, we performed a series of repeated experiments on different bovine eyes, all subjected to the same CXL protocol and signal processing. By analyzing the experimental data from ten bovine eyes treated with CXL, we compiled a summary of the intensity and spatial period shifts, which are presented in Table 5.1 and Table 5.2, respectively. From the analysis, we observed that the intensity values exhibited fluctuations in both negative and positive directions, without a consistent and continuous change in a single direction. This finding indicates that it is not possible to detect the variations occurring during the CXL process solely based on conventional intensity-based OCT. The intensity values alone do not provide sufficient information to assess the structural alterations taking place. Additionally, we measured the intensity histograms for the virgin cornea, the cornea after 30 minutes of riboflavin instillation, and the treated cornea. However, similar to the intensity values, we did not observe any significant shifts or noticeable differences in the intensity histograms among these stages. This

further supports the limitation of intensity-based OCT in capturing and quantifying structural changes during the CXL treatment.

Table 5.1 The intensity changes between the virgin cornea and cross-linked cornea during the CXL treatment

Bovine corneas	Mean intensity values (dB)			
	Virgin	Treated	Shift	Percentage
S1	35.86	35.57	-0.29	-0.81%
S2	35.99	35.31	-0.68	-1.89%
S3	35.58	34.96	-0.62	-1.74%
S4	36.01	36.55	+0.54	+1.50%
S5	35.90	35.36	-0.54	-1.50%
S6	35.62	36.01	+0.39	+1.09%
S7	35.88	36.13	+0.25	+0.70%
S8	35.79	35.99	+0.20	+0.56%
S9	36.03	35.69	-0.34	-0.94%
S10	35.86	35.32	-0.54	-1.50%
Mean	35.85± 0.15	35.69± 0.48	-0.16± 0.46	(-0.45± 1.23)%

Table 5.2 The spatial period changes of the virgin cornea and cross-linked cornea during the CXL treatment

Bovine corneas	Mean spatial periods (nm)			
	Virgin	Treated	Shift	Percentage
S1	657.1	649.6	-7.5	-1.14%
S2	652.1	638.5	-13.6	-2.09%
S3	656.3	649.2	-7.1	-1.08%
S4	654.3	648.1	-6.2	-0.95%
S5	653.2	649.6	-3.6	-0.55%
S6	651.7	646.9	-4.8	-0.74%
S7	653.6	648.9	-4.7	-0.72%
S8	653.9	647.3	-6.6	-1.01%
S9	654.3	649.6	-4.7	-0.72%
S10	652.6	647.3	-5.3	-0.81%
Mean	653.9± 1.7	647.5± 3.3	-6.4± 2.8	(-0.98± 0.43)%

In summarizing all the experimental sets conducted using the proposed over-sampling nsOCT method, we evaluated that the spatial period of the corneas changed from 653.9 ± 1.7 nm (mean ± standard deviation) in the virgin corneas to 647.5 ± 3.3 nm in the treated corneas. This indicates a decrease in the spatial periods within the corneas by -6.4 ± 2.8 nm, corresponding to a percentage change of -0.98 ± 0.43% after the CXL treatment. Importantly, we observed a consistent decrease in spatial period for all the bovine corneas examined in the experiments. This provides strong evidence supporting the presence of nanoscale structural changes associated with the CXL treatment. The consistent nature of this decrease across multiple experiments enhances the credibility of the findings and underscores the efficacy of the proposed over-sampling nsOCT method in detecting and quantifying these nanoscale structural alterations.

To obtain comprehensive information, 3D volumetric data acquisition was employed to generate en face images at different imaging depths. Each en face image covered an area of 2 mm x 2 mm and consisted of 400 x 400 A-lines. The CXL treatment was carried out following the same protocol as described previously. Figure 5.8(a-c) presents the conventional OCT en face images, which fail to reveal any discernible features indicative of changes resulting from the CXL procedure. However, the nsOCT en face images, as shown in figure 5.8(d, e, f), demonstrate the ability to visualize nanoscale alterations, particularly between the virgin cornea and the cross-linked cornea. These images clearly exhibit a minor spatial period after the treatment, highlighting the structural changes that occur at the nanoscale level. In terms of quantitative analysis, the mean spatial periods of the en face data for the virgin cornea, the cornea after 30 minutes of riboflavin instillation, and the cross-linked cornea were calculated to be 653.2 nm, 654.3 nm, and 648.6 nm, respectively. These measurements further confirm the reduction in spatial period and the corresponding structural modifications occurring as a result of the CXL treatment.

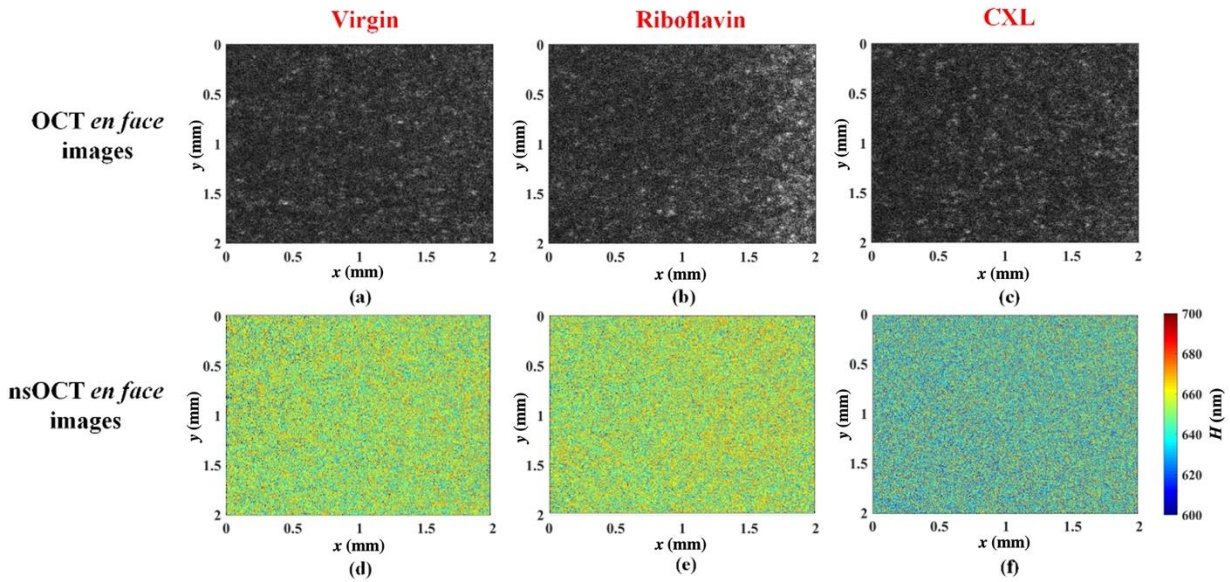

Fig. 5.8 Conventional OCT and nsOCT en face images at the three key treating steps during CXL treatment. (a, b, c) Conventional intensity-based OCT en face

images of the cornea after epithelium removal, after 30 min riboflavin instillation and after 30 min UVA illumination, respectively. (d, e, f) The corresponding nsOCT en face images with spatial period mapping, presenting the nanoscale structural alterations. The en face images were constructed at the depth of ~500 µm. The colour bar presents the spatial periods with unit nanometre.

Figure 5.9 presents the spatial period values (Y-Axis) plotted against depth (X-Axis) in the range of 200 to 770 µm, with depth intervals of 38 µm step width. In figure 5.6 (b, d, f), the depth range from 0 to 200 µm does not have sufficient image data points due to the cornea's positioning within the imaging depth and its curvature shape. As a result, the image data in this specific depth range may be limited, affecting the visualization and analysis of structural changes in that region. The change in spatial period for each treatment step is clearly evident in the graph. The measured spatial period range depends on the detected wavelength range. It is possible that there are other spatial period sizes within the cornea that are beyond the range of our current detection capabilities. To identify and extract those spatial periods, further investigation using an OCT system with a larger illumination source bandwidth would be necessary. In the plot, the spatial period values for a virgin bovine cornea are represented by red circles, while the spatial periods for a cornea treated with riboflavin are denoted by yellow squares. It is notable that the spatial periods for the virgin cornea consistently exhibit smaller values compared to those for the riboflavin-treated cornea. A significant change in spatial period occurs after the 30 minutes of UVA irradiation. The values of the spatial periods reduce by approximately 3 nm, decreasing from 652 nm to 649 nm. This demonstrates a measurable decrease in the structural size of the cornea following the CXL treatment.

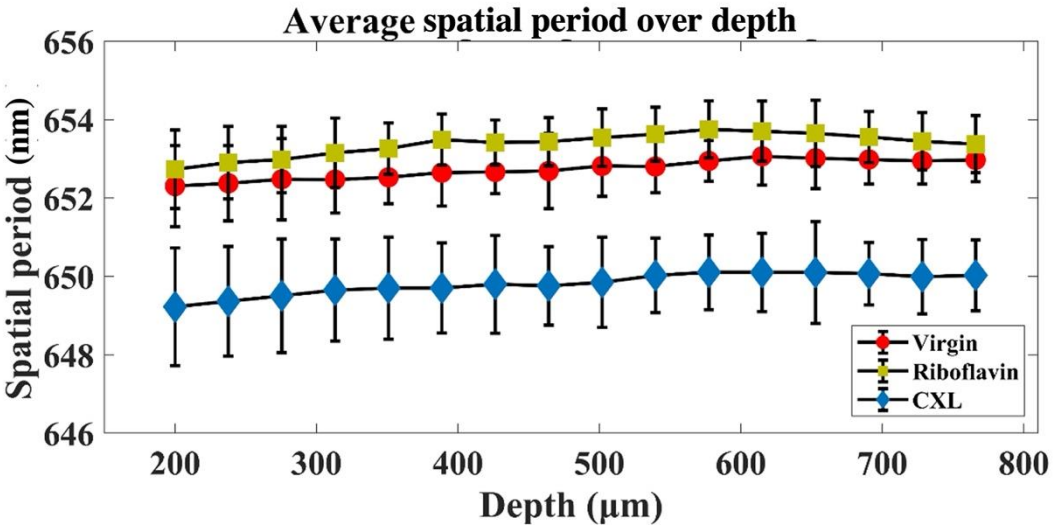

Fig. 5.9 Mean spatial periods at various corneal depths for the virgin cornea, the cornea after 30 min riboflavin instillation and the cross-linked cornea, indicated by red, yellow and blue colour, respectively.

In figure 5.10, a zoomed-in plot of the spatial periods of the treated cornea reveals a slight increase in spatial period values over the corneal depth. This observation is interesting and may indicate that the crosslinking process is influenced by adjacent biochemical reactions initiated by the superficial UVA irradiation. It is possible that the structural changes occurring in the superficial layers of the cornea generate a dominant spatial periodicity that propagates throughout the entire signal range. As a result, the deeper regions of the cornea appear to exhibit changes in structural sizes in conjunction with the top layers. However, at this stage, it is important to note that the exact reasons behind this phenomenon cannot be confirmed. Further research will be necessary to explore and understand the underlying mechanisms responsible for the observed changes in spatial periods throughout the corneal depth during the crosslinking process.

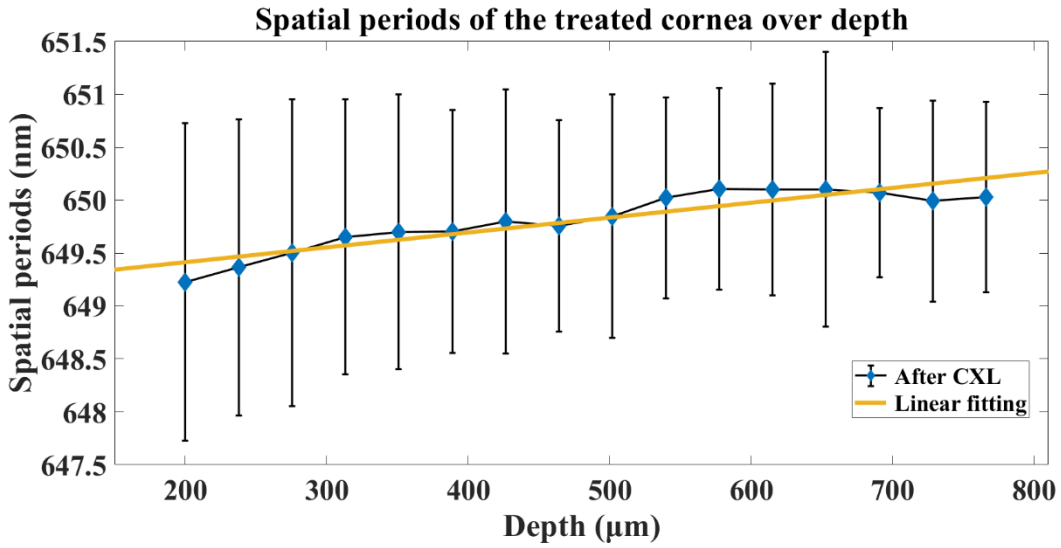

Fig. 5.10 The spatial periods plot of the treated cornea over different depths.

Based on the values plotted in figure 5.9, a paired t-test was performed (samples size ten per group) which confirmed the high significance (p <10^{-4}) between the virgin corneas and the group after 30 min riboflavin instillation. The p-value test for spatial changes between the virgin and CXL treated corneas provided an even larger significance p <10^{-13}.

5.4 Discussion

The experimental results obtained from Bragg gratings with known structural sizes have effectively demonstrated the feasibility of the over-sampling nsOCT method in distinguishing nanoscale structural alterations in both B-scan and en face images. In the study involving *ex vivo* bovine corneas subjected to CXL treatment, both conventional intensity-based OCT images and corresponding nsOCT images were generated for different stages of the treatment, including the virgin cornea after epithelial removal, the cornea after 30 minutes of riboflavin instillation, and the cornea after 30 minutes of UVA irradiation. The conventional OCT images proved to be inadequate in recognizing the internal structural changes within the cornea due to the limited axial resolution of only a few micrometers. However, through the use of the nsOCT modality, we were able to

detect and visualize the ultrastructural variations occurring inside the cornea during the CXL treatment. Specifically, our investigation revealed that the spatial periods of the cornea experienced a slight increase after 30 minutes of riboflavin instillation, indicating a minor change in structural size. However, after 30 minutes of UVA irradiation, a significant decrease in spatial periods was observed, indicating a substantial reduction in the structural size of the cornea.

According to existing reports, it is expected that the structural size inside the cornea would decrease after riboflavin absorption due to the dehydration caused by the hypertonic photosensitizer solution. However, in our study, we observed an increased spatial period after 30 minutes of riboflavin instillation in a dark environment. This finding appears to contradict the results obtained from TEM or SEM methods. We propose that the reason for this discrepancy lies in the increased refractive index inside the cornea following riboflavin immersion. In OCT systems, we measure the optical path difference, which is influenced by both the physical structural size and the refractive index of the sample. The minor increment in the spatial period after 30 minutes of riboflavin instillation may be attributed to the higher refractive index of riboflavin compared to that of the cornea itself. As riboflavin penetrates inside the cornea, the refractive index of the stroma increases, leading to a larger spatial period. This change in refractive index could potentially offset or mask the expected decrease in structural size resulting from dehydration. But in our measurement we used refractive index value one to measure the optical spatial period. Thus, the combined effect of changes in both the physical structural size and the refractive index of the cornea may explain the observed increase in spatial period after riboflavin instillation, contrary to the anticipated decrease based on dehydration alone.

Previous literature has discussed various methods for investigating the changes in interfibrillar distance and fibril diameter within the corneal stroma after CXL treatment. Among these methods are TEM, SEM, and X-ray imaging. A study by

T. Sibillano et al. [25] utilized small-angle X-ray scattering (SAXS) microscopy to examine *ex vivo* bovine corneas. Their findings revealed a decrease in the interfibrillar distance from approximately 62 nm in the virgin cornea to approximately 56 nm in the treated cornea. Additionally, the study observed a decrease in fibril shell thickness from around 11 nm to approximately 9 nm as a result of cross-linking within proteoglycan core proteins. These changes contribute to the decreased spatial periods observed and are consistent with the proposed nsOCT method. Similar results regarding the structural changes associated with the CXL process have been reported by other studies as well. Ho, Leona TY et al. [46], Freund et al. [47], and Cheng et al. [48] have all provided evidence supporting these findings, further validating the agreement between their results and the proposed nsOCT method. Other studies have also reported similar results in rabbit, porcine, and sheep corneas. For instance, Sally Hayes [20, 24] found that the fiber diameter of in vitro porcine corneas increased, while the interfibrillar spacing decreased. *Ex vivo* CXL treatment on sheep corneal tissue samples was associated with slight decreases in collagen intermolecular spacing.

To investigate the specific contribution of corneal cross-linking treatment to the observed structural alterations, a control experiment was conducted to assess the impact of factors like dehydration. In this control experiment, a bovine eye was subjected to the same CXL procedure described previously, with the exception that half of the cornea was shielded from UVA illumination. By blocking UVA exposure to a portion of the cornea, any structural changes observed in that specific region can be attributed to factors other than corneal cross-linking, such as dehydration. This control experiment allows for a comparison between the treated and untreated regions of the cornea, providing insights into the specific effects of the cross-linking treatment. In the control experiment, the virgin cornea was imaged immediately after epithelial removal. Figure 5.11(a) displays the

intensity-based OCT image of the virgin cornea, while figure 5.11(b) presents the corresponding nsOCT image. Subsequently, riboflavin was applied to the entire cornea and allowed to sit for 30 minutes in a dark environment. In the final step, a long-pass filter was utilized to block UVA illumination in the right half of the cornea, as illustrated in figure 5.11(c). Consequently, the corneal cross-linking treatment only took place in the left half of the cornea, as the UVA light was unable to reach the right half. Upon analysis, it was observed that the spatial period of the left half of the cornea measured 647.9 nm, while the right half measured 653.6 nm. These measurements indicate a decreased spatial period in the left half of the cornea following CXL treatment. The nsOCT image corresponding to this experiment is shown in figure 5.11(d), revealing the nanoscale structural differences between the left and right halves of the same cornea.

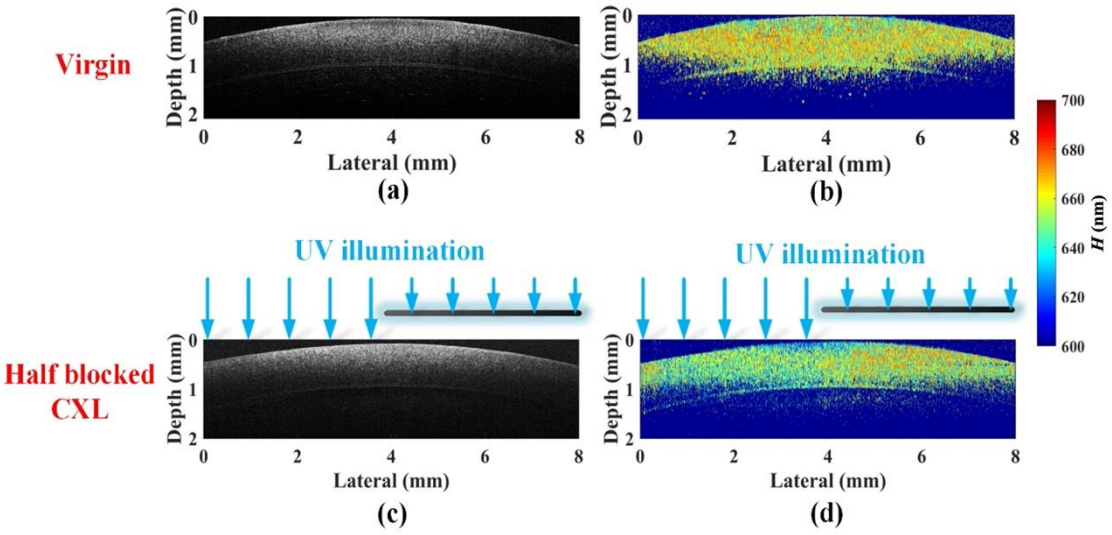

Fig. 5.11 A control experiment with the cornea half blocked from UVA irradiation. (a, b) Conventional intensity-based OCT and nsOCT images of the virgin cornea. (c) The conventional OCT image of the half cross-linked cornea using a UVA irradiation block on the right half. (d) The corresponding nsOCT image of the half cross-linked cornea, illustrating the nanoscale structural

difference between the left half and right half in the same B-scan. The colour bar presents the spatial periods with unit nanometre.

By comparing the treated and untreated halves of the cornea in this control experiment, the specific impact of corneal cross-linking treatment can be evaluated. The observed differences in spatial periods and the corresponding nsOCT images provide evidence that the structural alterations observed in the cornea are indeed a result of the CXL treatment, independent of factors like dehydration. These findings reinforce the role of corneal cross-linking in inducing nanoscale structural changes within the cornea.

5.5 Conclusion

This chapter explained that the nano-structural changes inside *ex vivo* bovine cornea associated with CXL treatment can be clearly detected by the proposed over-sampling nsOCT method. The results have shown that the spatial periods inside corneal stroma increased slightly after 30 minutes riboflavin instillation but decreased significantly after 30 min UVA irradiation. En face nsOCT images at different corneal depths have also confirmed the consistent consequences, demonstrating the nanoscale structural size decreases after the CXL treatment.

The proposed over-sampling nsOCT method can be easily implemented using existing OCT systems, without the need for additional components. This makes it a relatively straightforward technique to apply in *in vivo* tissues and facilitates its translation to clinical use as a novel imaging system. The fast and non-invasive nature of this method, combined with its nanoscale sensitivity, makes it a promising tool for diagnostic assessment associated with corneal cross-linking (CXL) treatment. It has the potential to serve as an indicator of treatment efficacy and provide valuable real-time feedback from patient's tissue during the procedure. Future research will focus on implementing this method for *in vivo*

corneal imaging during CXL treatment. This includes monitoring the nanoscale structural variations at different stages of the treatment process and assessing the postoperative outcomes. By utilizing the over-sampling nsOCT method in clinical settings, it may be possible to enhance the monitoring and evaluation of CXL treatment, leading to improved patient care and treatment optimization. Furthermore, to accurately measure the physical spatial period or precise nanoscale structural size differences, it is essential to incorporate the exact refractive value. This aspect could be taken into consideration in future studies. Overall, the application of the over-sampling nsOCT method in *in vivo* corneal imaging holds great promise and opens up new possibilities for real-time, high-resolution assessment of structural changes in the cornea during CXL treatment and beyond.

References

1. J. A. Gomes, D. Tan, C. J. Rapuano, M. W. Belin, Jr. R. Ambrósio, J. L. Guell, F. Malecaze, K. Nishida, and V. S. Sangwan, "Global consensus on keratoconus and ectatic diseases," *Cornea* **34**(4), 359-369 (2015).
2. S. M. Kymes, J. J. Walline, K. Zadnik, J. Sterling, M. O. Gordon, "Changes in the quality-of-life of people with keratoconus", *Am. J. Ophthalmol.* **145**(4), 611-617 (2008).
3. T. V. Mas, C. MacGregor, R. Jayaswal, D. O'Brart, N. Maycock, "A review of keratoconus: Diagnosis, pathophysiology, and genetics," *Surv. Ophthalmol.* **62**(6), 770-783 (2017).
4. D. A. Godefrooij, G. A. de Wit, C. S. Uiterwaal, S. M. Imhof, R. P. Wisse, "Age-specific Incidence and Prevalence of Keratoconus: A Nationwide Registration Study," *Am. J. Ophthalmol.* **175**, 169-172 (2017).
5. M. Romero-Jiménez, J. Santodomingo-Rubido, and J. S. Wolffsohn, "Keratoconus: a review," *Cont. Lens and Anterior Eye* **33**(4), 157-166 (2010).

6. J. L. Alio, A. Abbouda, D. D. Valle, J. M. B. Del Castillo, and J. A. G. Fernandez, "Corneal cross linking and infectious keratitis: a systematic review with a meta-analysis of reported cases," *J. of Ophthalmic Inflamm. Infect.* **3**(1), 1-7 (2013).
7. K. M. Meek, S. Hayes "Corneal cross-linking - a review," *Ophthalmic Physiol. Opt.* **33**(2), 78-93 (2013).
8. S. A. Balasubramanian, D.C. Pye, M.D. Willcox, "Effects of eye rubbing on the levels of protease, protease activity and cytokines in tears: relevance in keratoconus," *Clin. Exp. Optom.* **96**(2), 214-218 (2013).
9. G. R. Snibson. "Collagen cross-linking: a new treatment paradigm in corneal disease – a review," *Clin Exp Ophthalmol.* **38**(2), 141-153 (2010).
10. F. Raiskup, and E. Spoerl, "Corneal crosslinking with riboflavin and ultraviolet AI Principles," *Ocul. Surf.* **11**(2), 65-74 (2013).
11. J. B. Randleman, S. S. Khandelwal, and F. Hafezi, "Corneal cross-linking," *Surv. Ophthalmol.* **60**(6), 509-523 (2015).
12. E. Spörl, F. Raiskup-Wolf, and L. E. Pillunat, "Biophysical principles of collagen cross-linking," *Klin. Monatsbl. Augenh.* **225**(2), 131-137 (2008).
13. B. H. Jeng, M. Farid, S. V. Patel, and I. R. Schwab, "Corneal cross-linking for keratoconus: a look at the data, the food and drug administration, and the future," *Ophthalmology* **123**(11), 2270-2272 (2016).
14. B. J. Blackburn, S. Gu, M. R. Ford, V. de Stefano, M. W. Jenkins, W. J. Dupps, and A. M. Rollins, "Noninvasive assessment of corneal crosslinking with phase-decorrelation optical coherence tomography," *Investig. Ophthalmol. & Vis. Sci.* **60**(1), 41-51 (2019).
15. Y. Zhou, Y. Wang, M. Shen, Z. Jin, Y. Chen, Y. Zhou, J. Qu, and D. Zhu, "*In vivo* evaluation of corneal biomechanical properties by optical coherence elastography at different cross-linking irradiances," *J. Biomed. Opt.* **24**(10), 105001 (2019).

16. E. Spoerl, M. Huhle, and T. Seiler, “Induction of cross-links in corneal tissue,” *Exp. Eye Res.* **66**(1), 97-103 (1998).
17. G. Wollensak, and E. Iomdina, “Long-term biomechanical properties of rabbit cornea after photodynamic collagen crosslinking,” *Acta Ophthalmol.* **87**(1), 48-51 (2009).
18. S. H. Chang, A. Mohammadvali, K. J. Chen, Y. R. Ji, T. H. Young, T. J. Wang, C. E. Willoughby, K. J. Hamill, and A. Elsheikh, “The relationship between mechanical properties, ultrastructural changes, and intrafibrillar bond formation in corneal UVA/riboflavin cross-linking treatment for keratoconus,” *J. Refract. Surg.* **34**(4), 264-272 (2018).
19. S. Choi, S. C. Lee, H. J. Lee, Y. Cheong, G. B. Jung, K. H. Jin, and H. K. Park, “Structural response of human corneal and scleral tissues to collagen cross-linking treatment with riboflavin and ultraviolet A light,” *Lasers Med. Sci.* **28**(5), 1289-1296 (2013).
20. S. Hayes, C. Boote, C. S. Kamma-Lorger, M. S. Rajan, J. Harris, E. Dooley, N. Hawksworth, J. Hiller, N. J. Terill, F. Hafezi, and S. K. Brahma, “Riboflavin/UVA collagen cross-linking-induced changes in normal and keratoconus corneal stroma,” *PLoS One* **6**(8), 22405 (2011).
21. E. Spoerl, N. Terai, F. Scholz, F. Raiskup, and L. E. Pillunat, “Detection of biomechanical changes after corneal cross-linking using Ocular Response Analyzer software,” *J. Refract. Surg.* **27**(6), 452-457 (2011).
22. H. R. Vellara, and D. V. Patel, “Biomechanical properties of the keratoconic cornea: a review,” *Clin. Exp. Optom.* **98**(1), 31-38 (2015).
23. G. Wollensak, M. Wilsch, E. Spoerl, and T. Seiler, “Collagen fibre diameter in the rabbit cornea after collagen crosslinking by riboflavin/UVA,” *Cornea* **23**(5), 503-507 (2004).
24. S. Hayes, C. S. Kamma-Lorger, C. Boote, R. D. Young, A. J. Quantock, A. Rost, Y. Khatib, J. Harris, N. Yagi, N. Terrill, and K. M. Meek, “The effect of riboflavin/UVA collagen cross-linking therapy on the structure

and hydrodynamic behavior of the ungulate and rabbit corneal stroma," *PLoS One* **8**(1), 52860 (2013).

25. T. Sibillano, L. De Caro, F. Scattarella, G. Scarcelli, D. Siliqi, D. Altamura, M. Liebi, M. Ladisa, O. Bunk, and C. Giannini, "Interfibrillar packing of bovine cornea by table-top and synchrotron scanning SAXS microscopy," *J. Appl. Cryst.* **49**(4), 1231-1239 (2016).
26. K. M. Bottós, J. L. Dreyfuss, C. V. Regatieri, A. A. Lima-Filho, P. Schor, H. B. Nader, and W. Chamon, "Immunofluorescence confocal microscopy of porcine corneas following collagen cross-linking treatment with riboflavin and ultraviolet," *J. of Refract. Surg.* **24**(7), 715 (2008).
27. I. B. Damgaard, Y. C. Liu, A. K. Riau, E. P. W. Teo, M. L. Tey, C. L. Nyein, and J. S. Mehta, "Corneal remodeling and topography following biological inlay implantation with combined crosslinking in a rabbit model," *Sci. Rep.* **9**(1), 1-11 (2019).
28. D. Huang, E. A. Swanson, C. P. Lin, J. S. Schuman, W. G. Stinson, W. Chang, M. R. Hee, T. Flotte, K. Gregory, C. A. Puliafito, and J. G. Fujimoto, "Optical coherence tomography," *Science* **254**(5035), 1178-1181 (1991).
29. J. M. Schmitt, "Optical coherence tomography (OCT): a review," *IEEE J. Sel. Top. Quantum Electron.* **5**(4), 1205-1215 (1999).
30. W. Drexler, U. Morgner, R. K. Ghanta, F. X. Kärtner, J. S. Schuman, and J. G. Fujimoto, "Ultrahigh-resolution ophthalmic optical coherence tomography," *Nat. Med.* **7**(4), 502-507 (2001).
31. E. Götzinger, M. Pircher, B. Baumann, C. Hirn, C. Vass, and C. K. Hitzenberger, "Retinal nerve fibre layer birefringence evaluated with polarization sensitive spectral domain OCT and scanning laser polarimetry: a comparison," *J. Biophotonics* **1**(2), 129-139 (2008).
32. Y. Li, O. Tan, R. Brass, J. L. Weiss, and D. Huang, "Corneal epithelial thickness mapping by Fourier-domain optical coherence tomography in

normal and keratoconic eyes," *Ophthalmology* **119**(12), 2425-2433 (2012).

33. J. G. Fujimoto, "Optical coherence tomography for ultrahigh resolution *in vivo* imaging," *Nat. Biotechnol.* **21**(11), 1361-1367 (2003).
34. S. P. Veres, J. M. Harrison, and J. M. Lee, "Cross-link stabilization does not affect the response of collagen molecules, fibrils, or tendons to tensile overload," *J. Orthop. Res.* **31**(12), 1907-1913 (2013).
35. M. Born, M. and E. Wolf, "*Principles of optics: electromagnetic theory of propagation, interference and diffraction of light*," Elsevier, (2013).
36. S. Alexandrov, S. Uttam, R. K. Bista, K. Staton, and Y. Liu, "Spectral encoding of spatial frequency approach for characterization of nanoscale structures," *Appl. Phys. Lett.* **101**(3), 033702 (2012).
37. S. Alexandrov, S. Uttam, R. K. Bista, C. Zhao, and Y. Liu, "Real-time quantitative visualization of 3D structural information," *Opt. Express* **20**(8), 9203-9214 (2012).
38. S. Alexandrov, J. McGrath, H. Subhash, F. Boccafoschi, C. Giannini, and M. Leahy, "Novel approach for label free super-resolution imaging in far field," *Sci. Rep.* **5**(1), 1-8 (2015).
39. S. Alexandrov, J. McGrath, C. J. Sheppard, F. Boccafoschi, C Giannini, T. Sibillano, H. Subhash, J. Hogan, and M. Leahy, "Label-free ultra-sensitive visualization of structure below the diffraction resolution limit," *J. Biophotonics* **11**(7), 201700385 (2018).
40. S. Alexandrov, H. M. Subhash, A. Zam, and M. Leahy, "Nano-sensitive optical coherence tomography," *Nanoscale* **6**(7), 3545-3549 (2014).
41. S. Alexandrov, H. M. Subhash, M. Leahy, Z. Azhar (National University of Ireland Galway), European Patent EP3055643 B1, (2014) and U.S. Patent 10,012,492, (2018).

42. S. Alexandrov, H. M. Subhash, and M. Leahy, "Nanosensitive optical coherence tomography for the study of changes in static and dynamic structures," *Quantum Electron.* **44**(7), 657 (2014).
43. R. Dsouza, J. Won, G. L. Monroy, M. C. Hill, R. G. Porter, M. A. Novak, and S. A. Boppart, "*In vivo* detection of nanometre-scale structural changes of the human tympanic membrane in otitis media," *Sci. Rep.* **8**(1), 1-13 (2018).
44. S. Alexandrov, P. M. McNamara, N. Das, Y. Zhou, G. Lynch, J. Hogan, and M. Leahy, "Spatial frequency domain correlation mapping optical coherence tomography for nanoscale structural characterization," *Appl. Phys. Lett.* **115**(12), 121105 (2019).
45. S. Alexandrov, A. Anand, Y. Zhou, M. Mary, D. Niamh, N. Kai, S. Georgina, R. McAuley, and M. Leahy, "Accessing depth-resolved high spatial frequency content from the optical coherence tomography signal," *Sci. Rep.* **11**(1), 17123 (2021).
46. L. T. Ho, A. M. Harris, H. Tanioka, N. Yagi, S. Kinoshita, B. Caterson, A. J. Quantock, R. D. Young, and K. M. Meek, "A comparison of glycosaminoglycan distributions, keratan sulphate sulphation patterns and collagen fibril architecture from central to peripheral regions of the bovine cornea," *Matrix Biol.* **38**, 59-68 (2014).
47. D. Freund, R. McCally, R. Farrell, S. Cristol, N. L'Hernault, and H. Edelhauser, "Ultrastructure in anterior and posterior stroma of perfused human and rabbit corneas. Relation to transparency," *Invest. Ophthalmol. Vis. Sci.* **36**(8), 1508-1523 (1995).
48. X, Cheng, and P. M. Pinsky, "Mechanisms of self-organization for the collagen fibril lattice in the human cornea," *J. Royal Soc. Interface* **10**(87), 20130512 (2013).

Chapter 6

Conclusion and future work

The thesis is dedicated towards development of a broadband fibre-based high-resolution spectral-domain OCT system for the extraction and quantification of morphological changes at the sub-micron length scales of biological tissue. Specifically, nsOCT models in combination with conventional OCT measurements are explored for the quantification of ultra-structural information on tissue, which are otherwise invisible in conventional OCT measurements. The ability of such nsOCT techniques has been investigated and implemented to *ex vivo* tissues in the context of tissue structural characterisation and diagnosis, with early indications revealing that the developed methods hold substantial potential and need further investigation. This thesis work is divided into two categories: technical developments of the SDOCT system using supercontinuum light source and imaging applications using SDOCT in conjunction with nsOCT approach.

In chapter 1, we described the earlier medical imaging techniques and their advantages and disadvantages. Then we described the advantages of light-based imaging systems to investigate the biological fundamentals of life. Further, we discussed the details history of OCT since the invention and its various imaging applications in clinical and industrial research.

In chapter 2, we discussed basic working principles, theoretical framework, and key performance metrics of the optical coherence tomography. Three types of OCT were introduced including time-domain, spectral-domain, and swept-source OCTs. Also, this chapter described the advantages of Fourier domain OCT compared to earlier development of the TDOCT. Various key performance metrics such as central wavelength and spectral range of the light source, axial resolution, lateral resolution, depth of focus, total imaging depth, roll-off and sensitivity were discussed in this chapter. Further, a brief description of OCT

applications in all different aspects were discussed, mainly based on biomedical research and clinical or industrial applications.

In chapter 3, we presented design of a fibre-based HR-SDOCT system and evaluation of a simple air-wedge method to compare axial resolution directly. At first, we described low-cost construction of the air-wedges, which should be easily accessible for many laboratories, but also has the potential to work with commercially fabricated wedges. The characterization of the axial resolution with air-wedges provides the opportunity to work with different AR coatings compared to using conventional mirrors. Future developments could also include the use of custom optical mounts that allow direct adjustment of the wedge spacing and slope. Further studies will be carried out to characterize the noise of the develop system and its impact on images. Nevertheless, the air-wedge also provides some information of the uncertainty of reproducing a PSF, which may be of interest for high NA image quality quantification.

In this chapter, we described the feasibility of using a broad bandwidth fibre-based OCT system in conjunction with a high-NA sample lens to improve the isometric shape of the image voxels. Specifically using broad bandwidth light source, we show improved structural visibility in B-frame and en face images. After quantitative contrast to noise ratio (CNR) comparison, it is confirmed that high-resolution system improved the structural visibility.

To characterised the HR-SDOCT system several OCT key parameters have been optimized such as axial resolution, lateral resolution and sensitivity. The axial resolution of the HR-SDOCT was calculated to be 3.7 microns based on the spectral bandwidth at FWHM and was measured with a Gaussian fit on the data recorded from the sample mirror to be 3.8 microns. The measured sensitivity roll-off from 109 dB to about 94 dB over a depth range of about 1 mm. The lateral resolution at the focal plane of the objective lens was simulated using Zemax for a scan range of 2 mm and it was 6 microns. The image of the USAF target showed

experimental lateral resolution 5.5 microns, which is the width of a single element. We compared axial resolution with a Telesto III system that is specified with 5.5 microns in air. The HR-SDOCT has about 1.4 times better axial resolution. The air-wedge analysis provided a mean axial resolution of 13 microns for the Telesto and 11 microns for the HR-SDOCT, which is about 1.2 times better axial resolution of the HR-SDOCT.

The improved image quality in conjunction to isometric image voxel geometry is of major interest for conventional OCT imaging. With the newly developed nanosensitive OCT (nsOCT) gives advantage from the extended spectral bandwidth which allows access to a wider distribution of spatial frequencies, and it improves the dynamic range of the length scale sensitivity. Using advanced signal and image processing techniques (nsOCT), we have characterized the *ex vivo* biological tissues to detect sub-micron morphological changes.

In chapter 4, we described differences between the structural changes with nanoscale sensitivity of healthy and lesional/cancerous regions from human skin tissues. The structural information with nanoscale sensitivity cannot be detected using conventional OCT, but nsOCT approach can clearly detect the healthy and lesional/cancerous regions with intervening margin area. The nsOCT demonstrated the ability to detect the depth-resolved structural changes with nanoscale sensitivity within a 3D tissue at different depths. By increasing the sensitivity of OCT to nanoscale structural changes within the sample, the described approach bridges the gap between high resolution imaging and enhanced depth of imaging in OCT. The detected dynamic range of the nanometre length scale sensitivity of the tissue structure depends on the illumination source's spectral bandwidth. The chapter described the advantages of using of broadband light source like supercontinuum laser. The detected broader spectral range revealed the additional structural information. This chapter also presented a

comparative study between nsOCT and confocal microscopy for detecting the nanometre scale structural changes at different bandwidths of structural sizes. This comparative study shows a similar trend to the nsOCT results. A corresponding study with other bandwidths of the lower spatial frequencies was done using histological images. The histology image analysis results follow similar trend as both nsOCT and confocal microscopy results, the measured spatial period, or dominant structural sizes in the lesional region is higher compared to the healthy region.

The techniques presented in this chapter can be used as a tool to detect and monitor skin cancer at an early stage, possibly in a pre-invasive phase, which may facilitate early clinical intervention. Implementation in real-time would allow more confident surgery about the marginal area of the skin cancer region and possible reduce the hospital stay/revisit. For this studies all the tissue samples used were collected post-operatively, following pathological confirmation of the histological diagnosis. To further develop this technique for *in vivo* imaging applications is required. Especially in clinical imaging during the biopsy process and comparison with the nsOCT technique to detect the healthy and lesional/cancerous region along with the marginal area is needed. The nsOCT technique can be used to study the morphological changes of cancerous cells compared to normal cells where the conventional OCT is used. The nanoscale structural changes at the beginning stage of disease progression can be captured more efficiently using nsOCT.

In chapter 5, we demonstrated that the structural changes with nanoscale sensitivity inside *ex vivo* bovine cornea associated with CXL treatment and clearly detected by the proposed over-sampling nsOCT method. Several groups of samples have consistently shown that the spatial periods inside corneal stroma increased slightly after 30 minutes riboflavin instillation but decreased significantly after 30 min UVA irradiation. En face nsOCT images at different

corneal depths have also confirmed the consistent consequences demonstrating the nanoscale structural size decreases after the CXL treatment.

The proposed method can be implemented using the existing OCT system without any additional components, therefore it can be relatively straightforward to be applied in *in vivo* tissues and translated to clinical use as a novel imaging system. Due to its fast, non-invasive detection method and nanoscale sensitivity, this unique technology has the potential to be an indicator in diagnostic assessment associated with CXL treatment, and possibly to be a real-time monitoring tool in clinics as a fast way to receive feedback from patient's tissue samples. Further studies will be carried out to implement this method for *in vivo* corneal detections associated with CXL treatment, including monitoring the nanoscale structural variations at the different treatment stages and for postoperative assessment.